

POLITECNICO DI TORINO

Collegio di Ingegneria Chimica e dei Materiali

**Corso di Laurea Magistrale
in Ingegneria dei Materiali**

Tesi di Laurea Magistrale

**Zinc Oxide-Modified Copper catalyst
materials for the electrochemical reduction
of Carbon Dioxide to Carbon Monoxide**



Relatori

Prof. Giancarlo Cicero
Dott. Juqin Zeng

Candidato

Telemaco Rino

Dicembre 2019

Contents

Contents	I
Riassunto in italiano	III
Abstract	XVII
1 Introduction	1
1.1 Greenhouse effect and greenhouse gases	1
1.2 Strategies of mitigating CO ₂ effect	3
1.3 Aim of the work	4
2 Electrochemical CO₂ reduction reaction	5
2.1 Generalities	5
2.2 Electrocatalysts	6
2.3 Hydrogen evolution reaction and syngas	6
2.4 Efficiency of the electrodes and CO ₂ RR parameters	7
2.5 CO ₂ RR on Cu-based catalysts and state-of-the-art	8
2.5.1 Nano-porous structures and NP size effect	8
2.5.2 NP shape effect	9
2.5.3 NP alloying elements effect	9
2.5.4 Support material effect	10
3 Materials and methods	11
3.1 Synthesis	11
3.1.1 Microwave-assisted solvothermal synthesis	11
3.1.2 Materials used	12
3.1.3 Preparation of the catalyst materials	12
3.2 Electrode fabrication	14
3.2.1 Materials used	14
3.2.2 Electrode preparation	14
3.3 Material characterization	15
3.3.1 Field-Emission Scanning Electron Microscopy	15
3.3.2 X-Ray Diffractometry	16
3.3.3 Inductively Coupled Plasma/Optical Emission Spectrometry	18
3.3.4 Cyclic Voltammetry	19
3.3.5 Chronoamperometry	20
3.3.6 Gas chromatography	21
4 Results and discussion	25
4.1 Material's characterization	25
4.1.1 FESEM	25

4.1.2	XRD	31
4.1.3	ICP/OES	32
4.2	Electrochemical characterization	32
4.2.1	Cyclic Voltammetry	32
4.2.2	Chronoamperometry and micro-GC	35
4.3	Comparison of results	44
5	Conclusions and future developments	49
5.1	Industrial demands and future trends	49
5.2	Further analyses	50
	List of abbreviation and symbols	51
	References	53
	Acknowledgements	57

Riassunto in italiano

Introduzione

Il fenomeno del riscaldamento globale, accentuato dalle emissioni antropogeniche di gas serra nell'atmosfera, è un tema di grande attualità e interesse. La superficie terrestre assorbe l'energia che dal sole riesce ad attraversare l'atmosfera e successivamente la rilascia sotto forma di radiazione termica. Le molecole di gas serra, opache alla radiazione infrarossa, assorbono gran parte di questa energia e la rilasciano alle molecole vicine, mantenendo la temperatura terrestre su valori compatibili con la vita. Tuttavia le emissioni antropogeniche di gas serra accrescono la portata del fenomeno, aumentando la temperatura media terrestre. I principali gas serra sono il vapore acqueo, l'anidride carbonica (CO_2), il metano (CH_4), l'ossido di diazoto (N_2O) e i gas fluorinati.

La CO_2 non è il gas serra più pericoloso per il riscaldamento globale, ma il suo contributo al fenomeno è superiore agli altri gas serra per la sua abbondanza nell'atmosfera (Fig.0.1). Inoltre, secondo Muntean et al. [1], le emissioni di gas serra sono aumentate dall'inizio del 21° secolo rispetto ai precedenti trent'anni, soprattutto a causa delle crescenti emissioni di CO_2 da parte dei paesi in espansione economica, come Cina e India (Fig.0.2).

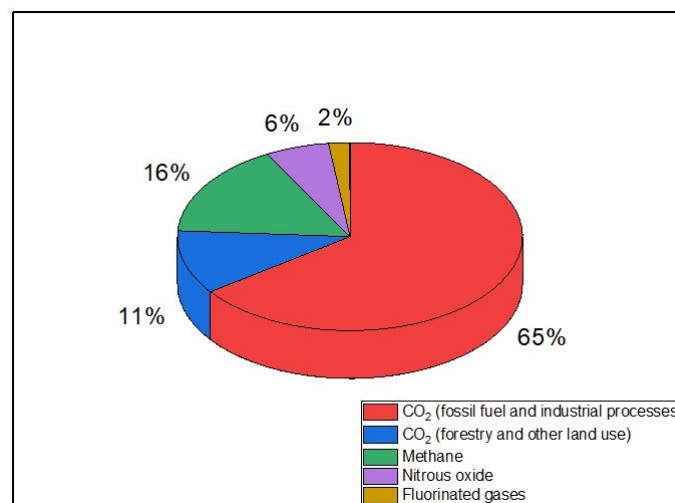


Figura 0.1: Emissioni globali di gas serra. Dati tratti da Pachauri et al. [2].

A questo proposito sono numerosi gli sforzi della comunità scientifica per riuscire a limitare le emissioni di CO_2 (utilizzando fonti energetiche alternative) e diminuirne la concentrazione atmosferica (catturando e convertendo quella già presente). La trasformazione della CO_2 è una strategia invitante perché, oltre a ridurre potenzialmente la concentrazione atmosferica di CO_2 , può diminuire l'impatto dei processi industriali che la emettono e generare un profitto da un gas di scarto. Infatti, la reazione di riduzione della CO_2 (CO_2RR , CO_2 reduction reaction) permette di sintetizzare da essa specie chimiche con un valore commerciale.

Questo studio verte sulla riduzione elettrochimica della CO_2 per i suoi numerosi vantaggi rispetto ad altri tipi di trasformazione, come la possibilità di costruire celle elettrochimiche

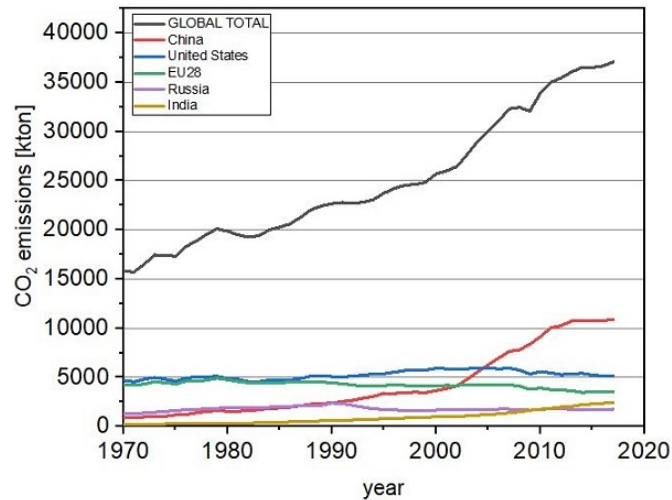


Figura 0.2: Emissioni di CO₂ dal 1970 divise per Paese.

adeguate alle produzioni industriali, l'utilizzo di elettroliti ecologici e la possibilità di utilizzare energia da fonti rinnovabili [3], trasformando la CO₂ senza contribuire a nuove emissioni. Con la riduzione elettrochimica la velocità di conversione della CO₂ è direttamente correlata al potenziale dell'elettrodo e può essere quindi modulata variando il potenziale applicato [4, 5]. L'elettroreduzione è una reazione non spontanea che avviene applicando un potenziale elettrico alla cella elettrolitica, un sistema a tre componenti schematizzato in figura 0.3. L'applicazione di un potenziale elettrico con la giusta polarità e sufficiente ampiezza causa la reazione di riduzione al catodo e l'ossidazione all'anodo, permettendo la decomposizione di specie chimiche normalmente inerti. L'energia necessaria a ridurre o ossidare una specie chimica è misurata attraverso il potenziale standard dell'elettrodo E^0 , il potenziale di metà cella riferito ad un elettrodo standard ad idrogeno (SHE, standard hydrogen electrode). L'SHE è definito come un elettrodo a potenziale 0,00V in condizioni standard (in elettrolita acido pH 0, 10⁵Pa e 25°C). Per testare e comparare gli elettrodi in condizioni diverse da quelle standard è possibile riferirsi ad un elettrodo reversibile ad idrogeno (RHE, reversible hydrogen electrode), calcolando il valore del potenziale con l'equazione di Nernst:

$$E (V \text{ vs. RHE}) = E_{(vs.ref.)} + E_{ref.}^0 (V) + 0.059 * pH \quad (0.1)$$

dove E è il potenziale applicato all'elettrodo e E^0 è il potenziale standard dell'elettrodo di riferimento vs. SHE.

Ridurre la CO₂ richiede un'elevata energia a causa dell'energia del doppio legame C=O che la caratterizza (energia di legame $E_B = 750\text{kJ/mol}$). La rottura del doppio legame è il primo passo di qualsiasi processo di riduzione [6, 7]. La tabella 0.1 mostra diversi prodotti ottenibili dalla CO₂RR in soluzione acquosa, tutti attraverso reazioni di trasferimento multiplo di elettroni-protoni [5, 6]. I prodotti ottenibili sono divisibili in due grandi categorie: i prodotti C₁ con un atomo di carbonio nella molecola finale (CO, HCOOH, CH₃OH e CH₄) e i prodotti C₂ con due molecole di carbonio (HOCCOOH, CH₂CH₂, CH₃CH₃ e CH₃CH₂OH). Oltre questi, possono essere ottenuti anche idrocarburi con più di due atomi di C.

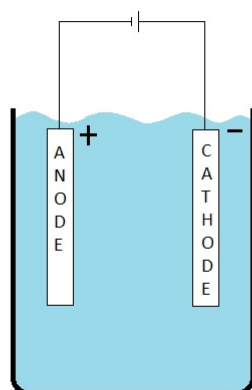


Figura 0.3: Una cella elettrolitica, il polo positivo è l'anodo e il polo negativo il catodo.

Tabella 0.1: Diversi prodotti di CO₂RR e loro potenziale standard di riduzione (E^0) [5, 7].

Prodotti	Meccanismo di reazione	E^0 [V vs. RHE]
CO	$\text{CO}_2 + 2 e^- + 2 \text{H}^+ \longrightarrow \text{CO} + \text{H}_2\text{O}$	-0,11
HCOOH	$\text{CO}_2 + 2 e^- + 2 \text{H}^+ \longrightarrow \text{HCOOH}$	-0,22
CH ₃ OH	$\text{CO}_2 + 4 e^- + 4 \text{H}^+ \longrightarrow \text{CH}_3\text{OH} + 2 \text{H}_2\text{O}$	+0,02
CH ₄	$\text{CO}_2 + 8 e^- + 8 \text{H}^+ \longrightarrow \text{CH}_4 + 2 \text{H}_2\text{O}$	+0,17
C ₂ H ₄	$\text{CO}_2 + 12 e^- + 12 \text{H}^+ \longrightarrow \text{C}_2\text{H}_4 + 4 \text{H}_2\text{O}$	+0,08
CO ₂ * ⁻	$\text{CO}_2 + e^- \longrightarrow \text{CO}_2^{*-}$	-1,5
H ₂	$2 \text{H}^+ + 2 e^- \longrightarrow \text{H}_2$	0,0

Secondo Xie et al. [6], il meccanismo di CO₂RR è divisibile in tre stadi:

1. adsorbimento e interazione della CO₂ con gli atomi superficiali del catalizzatore
2. attivazione della CO₂ favorita dal catalizzatore e successiva riduzione
3. desorbimento del prodotto di riduzione dalla superficie del catalizzatore e recupero del sito superficiale attivo

La generazione del radicale CO₂*⁻ è la fase che determina la velocità della CO₂RR con catalizzatori a base metallica, per l'elevata energia di barriera (Tab.0.1) necessaria ad iniziare il processo [6]. Infatti la CO₂ non viene ridotta ai potenziali riportati in tabella 0.1, ma a potenziali maggiori. La differenza tra il potenziale reale di riduzione e quello teorico termodinamico è detta sovratensione (overpotential), causata non solo dalla suddetta barriera energetica, ma anche da perdite ohmiche della cella e dal limite al trasporto di massa di reagenti sulla superficie dell'elettrodo. Il primo ruolo di un materiale catalizzatore è quindi quello di ridurre al minimo la sovratensione, per ottenere la reazione di riduzione desiderata con la minima quantità di energia fornita al sistema [4, 8]. Un'altra funzione del catalizzatore è quella di orientare la selettività dei prodotti della CO₂RR verso uno specifico prodotto; infatti ottenere diverse specie chimiche necessita di una successiva separazione di quest'ultime. Come è possibile vedere dalla

tabella 0.1, la reazione di evoluzione di idrogeno (HER, hydrogen evolution reaction) avviene a potenziali standard paragonabili con la CO₂RR, sottraendo parte dell'energia fornita al sistema e parte dei siti superficiali attivi alla CO₂RR, diminuendo l'efficienza del processo. Dopo la formazione del radicale CO₂*⁻, la reattività di questa specie controlla la distribuzione dei prodotti di reazione. Numerosi studi [4, 8, 9, 10] su diversi catalizzatori a base metallica hanno provato che l'interazione CO₂*⁻/catalizzatore dipende dalle proprietà elettroniche superficiali intrinseche del materiale, proprietà che influenzano anche l'energia di barriera. Sulla superficie di catalizzatori a base Au o Ag, il radicale CO₂*⁻ è legato alla superficie metallica attraverso l'atomo di C; ciò comporta la protonazione/riduzione in posizione O e la successiva formazione di *COOH. Questa specie può essere ridotta ulteriormente a *CO, e desorbirà come CO per la sua scarsa affinità con la superficie metallica. Questo comportamento è stato rilevato anche per catalizzatori a base Zn e Ga. Con catalizzatori a base Sn o In, il radicale CO₂*⁻ è legato alla superficie tramite l'atomo di ossigeno, con conseguente protonazione/riduzione in posizione C, formazione della specie HCOO⁻ e desorbimento di acido formico. Questo comportamento è stato riscontrato anche per catalizzatori a base Pb, Hg e Cd. Diversamente da questi materiali, i catalizzatori a base Cu hanno mostrato un comportamento differente, catalizzando la formazione di CO, HCOOH e anche prodotti C₂. Questa differenza può essere attribuita alla diversa affinità del radicale *CO con la superficie del rame. Materiali come Ni, Fe, Pt e Ti non sono compatibili con la CO₂RR in ambiente acquoso poiché troppo attivi nella riduzione dell'acqua in H₂ [8].

Nonostante i valori riportati in tabella 0.1, la riduzione della CO₂ in CO è cineticamente favorita poiché solo due elettroni sono coinvolti nella reazione [8]. Inoltre, l'inevitabile formazione di idrogeno dalla HER, se opportunamente limitata, può portare alla formazione di una miscela di gas H₂/CO, conosciuta come syngas, ad alto valore commerciale. Il syngas, a seconda del rapporto H₂/CO, può essere utilizzato per la produzione di ammoniaca (NH₃), alcoli e altri idrocarburi tramite processo Fischer-Tropsch. Ad oggi il syngas è prodotto dal metano tramite reazione di reforming con vapore, un processo che richiede elevate temperature e pressioni. Per questo motivo, l'utilizzo di un processo alimentato da un gas di scarto (CO₂) per produrre una miscela di CO e H₂ in condizioni meno critiche è molto suggestivo [8]. La miscela può essere arricchita successivamente con H₂ (prodotto con metodi più efficienti) per ottenere syngas con uno specifico rapporto H₂/CO.

Diversi sono i parametri utilizzati per descrivere le prestazioni di un catalizzatore. Tra questi, la densità di corrente (j) è il più usato per esprimere la velocità di reazione all'elettrodo. La densità di corrente è definita come la corrente elettrica per unità di superficie dell'elettrodo [11]. Per un dato catalizzatore e per un definito potenziale applicato, maggiore è la densità di corrente, maggiore sarà la velocità di reazione. Altro parametro descrittivo delle prestazioni di un catalizzatore è l'efficienza faradica (FE, faradaic efficiency). FE è definita come il rapporto tra gli elettroni necessari a formare un certo quantitativo di prodotto e il numero totale di elettroni coinvolti nel tempo di reazione,

$$FE(\%) = \frac{nNF}{j * A * t} * 100 \quad (0.2)$$

dove n è il numero di elettroni trasferiti nel processo, N è il quantitativo di prodotto generato, F è la costante di Faraday (96485, 33C/mol), j è la densità di corrente [A/m²], A è l'area dell'elettrodo [m²] e t è il tempo di reazione [s]. Idealmente, alla fine del processo di elettro-riduzione, la somma dei valori di FE per tutti i prodotti ottenuti dovrebbe essere 100% [8]. Le prestazioni e la distribuzione finale dei prodotti sono influenzate da diversi parametri chimico/fisici del materiale catalizzatore. Come già accennato, le proprietà elettroniche superficiali

intrinseche del materiale hanno un ruolo centrale nel determinare l'efficienza e la selettività della CO₂RR. Nei catalizzatori metallici formati da nanoparticelle (NP), anche la dimensione delle particelle del catalizzatore ne influenza il comportamento, determinando sia il tipo sia la densità dei siti superficiali attivi. Infatti, la reattività degli atomi superficiali dipende dal loro numero di coordinazione [6]. La forma delle NP è un altro parametro che influenza la selettività dei catalizzatori: a seconda della faccia cristallografica esposta, specie uguali generano diversi prodotti di reazione [6, 9]. La forma delle NP può influenzare anche l'efficienza di un catalizzatore (j); infatti, strutture di tipo dendritico possono favorire il trasporto di massa di reagente ai siti superficiali attivi [5]. L'unione di diversi materiali per formare un catalizzatore unico può modificare le proprietà di riduzione della CO₂. Questo perché, cambiando l'ambiente di reazione superficiale, varia l'affinità dei vari prodotti intermedi di reazione della CO₂RR (*CO, *COOH, *CHO ecc.) con il catalizzatore [12]. Queste variazioni dipendono fortemente dalla natura dei diversi materiali e, per estensione, dalla formazione di diversi siti superficiali attivi sulla superficie del catalizzatore. Diversi altri parametri influenzano le proprietà generali di un catalizzatore, tra questi ci sono il materiale di supporto al catalizzatore [6], la configurazione della cella elettrolitica, il tipo di elettrolita e il suo pH, la pressione e la temperatura di processo [8]. Da queste considerazioni è possibile stabilire che un materiale adatto alla CO₂RR deve presentare le seguenti caratteristiche:

- Elevata densità di corrente j (velocità di reazione)
- Bassa sovratensione (efficienza energetica)
- Elevati valori di FE per il prodotto desiderato (selettività)
- Elevata stabilità nel tempo
- Economicità dei precursori del materiale e del processo produttivo

Lo scopo di questo lavoro è quello della valutazione delle prestazioni di diversi materiali catalizzatori a base Cu modificati con ZnO (ZnO/Cu) per la CO₂RR. I diversi materiali sono stati sintetizzati in un unico passaggio tramite reazione Solvothermal assistita da microonde; una tecnica rapida, facilmente riproducibile, energeticamente conveniente e estensibile a processi industriali. Tutti i materiali sintetizzati sono stati caratterizzati morfologicamente e nella loro composizione con le tecniche Field-Emission Scanning Electron Microscopy (FESEM), X-Ray Diffractometry (XRD) e Inductively Coupled Plasma/Optical Emission Spectrometry (ICP/OES), mentre le proprietà elettrochimiche sono state testate con le tecniche Cyclic Voltammetry (CV) and Chronoamperometry (CA) unita con Gas Chromatography (GC) per la valutazione dei prodotti di reazione.

Materiali e metodi

Come precedentemente accennato, i materiali catalizzatori sono stati sintetizzati usando la tecnica solvothermal assistita da microonde. Con le microonde ($f = 300\text{MHz} - 300\text{GHz}$) è possibile riscaldare le molecole polari sfruttando il fenomeno fisico del riscaldamento dielettrico; il riscaldamento mirato del solvente polare permette la sintesi efficiente di composti ad elevata temperatura e moderate pressioni senza riscaldare l'intero forno e reattore, risparmiando tempo ed energia. Abbinare questa tecnica all'utilizzo di precursori atossici e rinnovabili, permette la sintesi ecosostenibile di materiali con un'elevata efficienza di reazione, basso consumo energetico e minimi scarti di processo rispetto a metodi di riscaldamento tradizionali [13].

I materiali utilizzati per la sintesi dei catalizzatori ZnO/Cu sono: rame(II) acetato idrato ($\text{Cu}(\text{Ace})$, $\text{Cu}(\text{CO}_2\text{CH}_3)_2 \cdot x\text{H}_2\text{O}$, 98), zinco(II) acetato diidrato ($\text{Zn}(\text{Ace})$, $\text{Zn}(\text{CO}_2\text{CH}_3)_2 \cdot 2\text{H}_2\text{O}$, $\geq 98\%$), idrossido di sodio (NaOH , 98%), glicole etilenico (EG, $(\text{CH}_2\text{OH})_2$, 99.8 %), acqua ed etanolo (EtOH). L'intero processo di sintesi è schematizzato in figura 0.4; i materiali Cu_xZn_y sono stati sintetizzati con un diverso rapporto stechiometrico $x : y$ variando la concentrazione dei precursori in soluzione, come illustrato in tabella 0.2. Per evidenziare le differenze tra i vari campioni sono stati sintetizzati anche due campioni di riferimento monometallici Cu e ZnO.

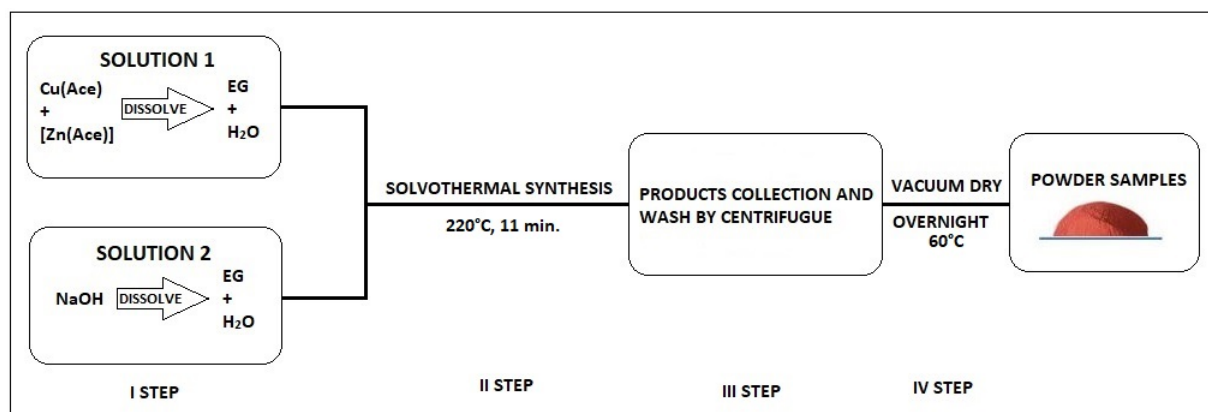


Figura 0.4: Schema del processo di sintesi dei materiali catalizzatori.

Tabella 0.2: Concentrazione dei precursori di Zn e Cu per la sintesi dei campioni.

Campioni	Cu(Ace) [mg]	Zn(Ace) [mg]
Cu	900	0
Cu_9Zn_1	900	120,6
Cu_9Zn_3	900	361,8
Cu_9Zn_6	900	723,7
Cu_9Zn_9	900	1085,5
ZnO	0	1085,5

La prima fase è la dissoluzione dei precursori di Cu e Zn in 5ml di acqua e 35ml di EG (solution 1 in Fig.0.4) e del NaOH in una soluzione contenente 24ml di EG e 4ml di H_2O ($\approx 1,14\text{M}$, solution 2 in Fig.0.4). Successivamente, 20ml della soluzione 2 sono aggiunti goccia a goccia alla soluzione 1. La soluzione ottenuta è trasferita nel reattore di Teflon del forno a microonde, connesso ai sensori di pressione e temperatura. Le sintesi sono effettuate a $T = 220^\circ\text{C}$ per 11 minuti (1 minuto per raggiungere la temperatura impostata e 10 minuti di sintesi). Dopo il raffreddamento a temperatura ambiente, il campione è trasferito in una fiala di plastica per separare la soluzione liquida dal precipitato attraverso una macchina centrifuga. Con la stessa macchina il precipitato è lavato due volte con acqua e una con EtOH per rimuovere i prodotti di decomposizione e il EG residuo. In ultimo, la polvere è lasciata ad asciugare in un forno sotto vuoto a 60°C per tutta la notte.

Per la preparazione degli elettrodi sono stati utilizzati: le diverse polveri a base Cu sintetizzate, acetylene carbon black (CB, Shawinigan Black AB50), soluzione Nafion[®] 117 (5 wt.%),

alcool isopropilico e carbon paper con gas diffusion layer (GDL) (SIGRACET 28BC, SGL Technologies). L'elettrolita scelto per le misure è una soluzione acquosa 0,1M di bicarbonato di potassio (KHCO_3 , 99,7%). Il carbon paper è utilizzato come substrato per le sue proprietà conduttive. Lo strato di catalizzatore viene depositato goccia a goccia sul carbon paper da una dispersione composta da materiale sintetizzato (5mg) e CB (0,5mg, per le proprietà conduttive) dispersi in Nafion[®] 117 (45 μl , per le sue proprietà di scambio protonico e di legante) e alcool isopropilico (160 μl). L'elettrodo è realizzato con una superficie attiva di $1.5 \times 1\text{cm}^2$ circondata da nastro di rame, per garantire il contatto conduttivo con il collettore di corrente della cella elettrolitica. Questo tipo di elettrodo è utilizzato per le misure CA in una cella a due compartimenti e tre elettrodi (Figure 0.5 e 0.6). Da questo elettrodo ($1.5 \times 1\text{cm}^2$) è ritagliato un secondo elettrodo più piccolo di $0.4 \times 0.5\text{cm}^2$ (superficie attiva) per le misure CV in un altro tipo di cella elettrolitica (Figure 0.5 e 0.7). Tutti gli elettrodi hanno lo stessa quantità di materiale catalizzatore (3,33mg/cm²).

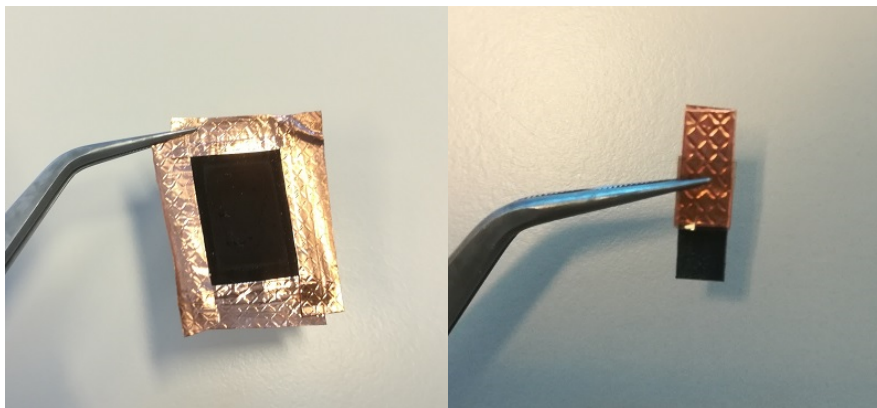


Figura 0.5: A sinistra, l'elettrodo grande ($1.5 \times 1\text{cm}^2$) per le misure CA . A destra, l'elettrodo piccolo ($0.4 \times 0.5\text{cm}^2$) per le misure CV.

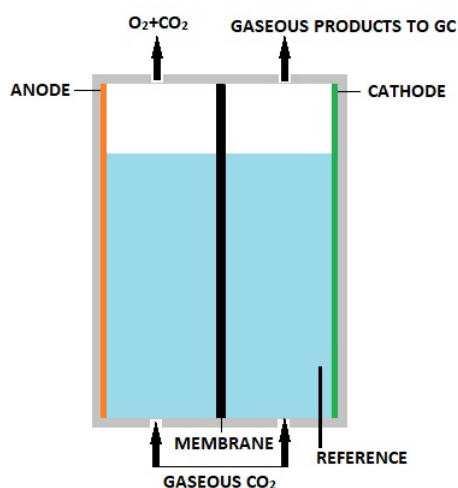


Figura 0.6: Rappresentazione della cella elettrolitica utilizzata per le misure CA.

L'analisi morfologica dei campioni è effettuata con microscopia FESEM a diversi ingrandimenti, ottenendo immagini con un aspetto tridimensionale in scala nanometrica. Le tecniche

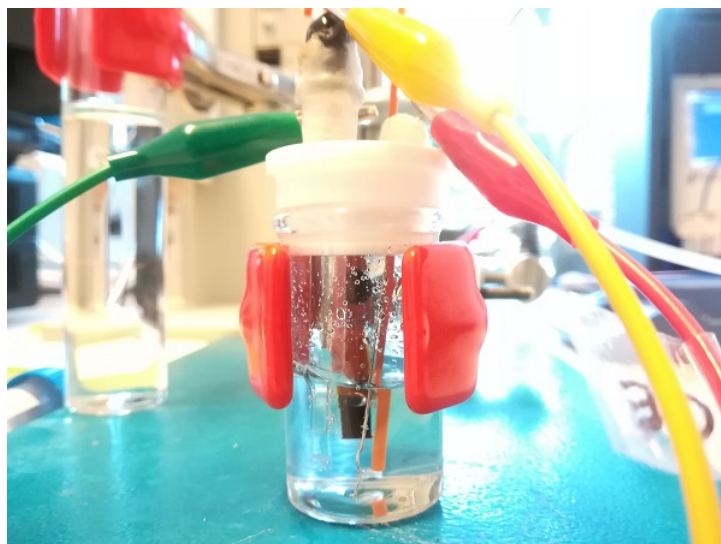


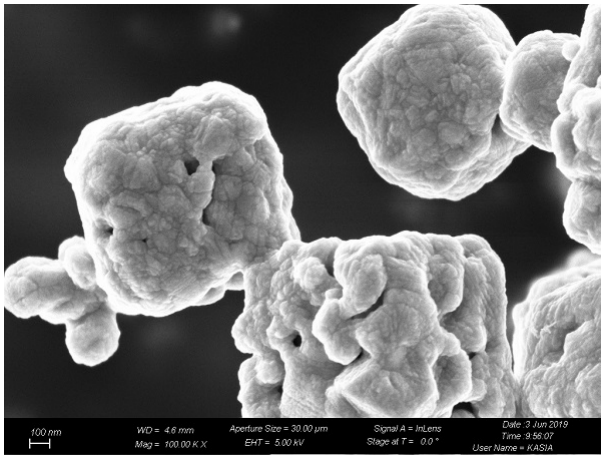
Figura 0.7: La cella elettrolitica utilizzata per le misure CV.

XRD e ICP/OES hanno permesso l'identificazione e la quantificazione delle diverse specie chimiche presenti nei campioni. Con l'analisi CV è stato possibile verificare l'attività dei diversi catalizzatori e l'intervallo di potenziale da investigare successivamente per l'analisi dei prodotti tramite CA collegata al micro gas cromatografo. La misura CA ha rivelato anche le proprietà conduttive dei vari elettrodi nell'intervallo di potenziale applicato.

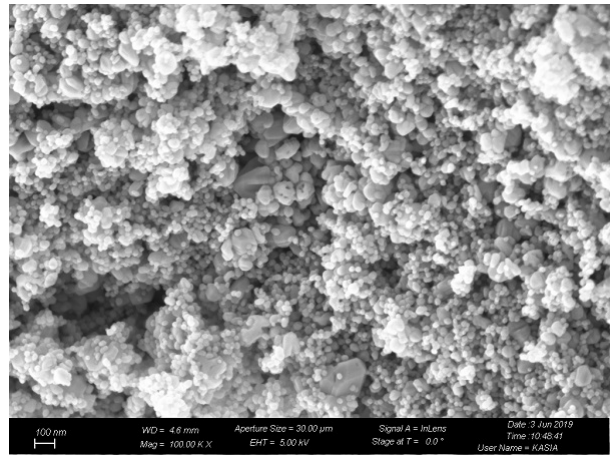
Discussione dei risultati

Dall'analisi delle immagini FESEM (Fig.0.8) è chiaramente visibile l'influenza della presenza di ZnO sulla morfologia dei diversi campioni. Le particelle del campione Cu hanno forma cubica, con un'ampia distribuzione delle dimensioni, nell'ordine dei μm (Fig.0.8a). Questa morfologia è riscontrabile anche per il campione Cu_9Zn_1 ; dalla figura 0.8c sono visibili particelle cubiche submicrometriche di Cu e particelle più piccole di ZnO. I campioni con rapporto atomico $\text{Cu}:\text{Zn} \geq 9 : 3$ hanno invece morfologia diversa (Fig.0.8d-0.8f): queste polveri sono caratterizzate da particelle di Cu, di dimensioni inferiori e di forma irregolare, decorate da particelle nanometriche di ZnO, simili a quelle del campione ZnO (Fig.0.8b).

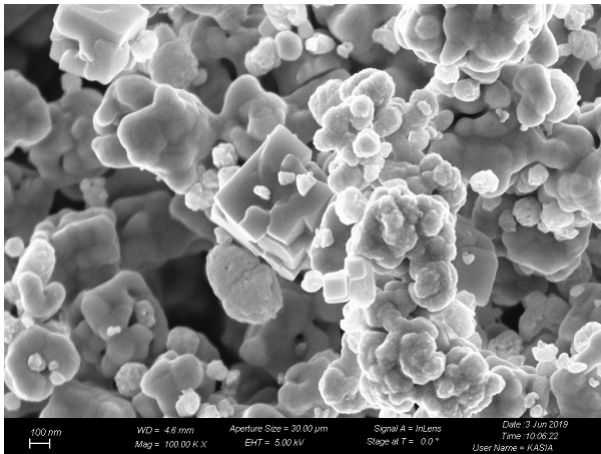
L'analisi dei dati XRD (Fig.0.9) evidenzia come l'aggiunta di maggiori quantità di Zn(Ace) non mitiga l'effetto riducente del EG e del NaOH sul Cu^{2+} dell'acetato di rame; risultano infatti solo piccole quantità di Cu_2O nei campioni ZnO/Cu, probabilmente dovute alla facile ossidazione delle nanoparticelle di Cu in aria. I campioni ZnO/Cu differiscono tra loro solo per l'intensità dei picchi relativi alla fase metallica Cu e alla fase cristallina ZnO. Il campione Cu presenta solo i picchi relativi al Cu metallico, mentre il campione ZnO solo quelli relativi all'ossido di zinco.



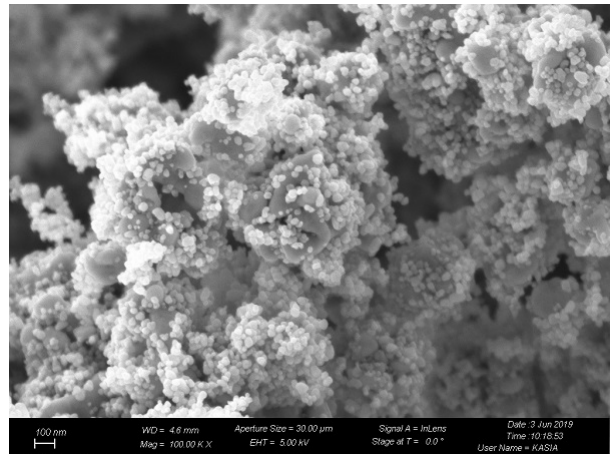
(a) Campione Cu.



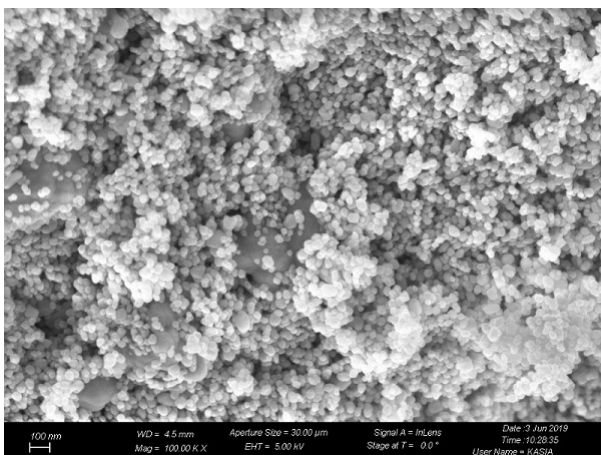
(b) Campione Zn.



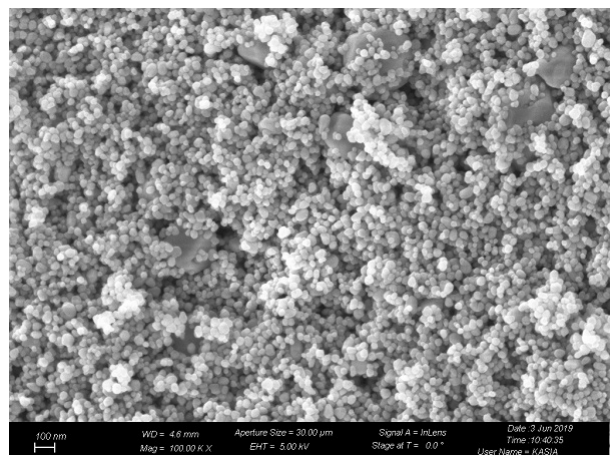
(c) Campione Cu_9Zn_1 .



(d) Campione Cu_9Zn_3 .



(e) Campione Cu_9Zn_6 .



(f) Campione Cu_9Zn_9 .

Figura 0.8: Immagini FESEM dei campioni a 10000000 X.

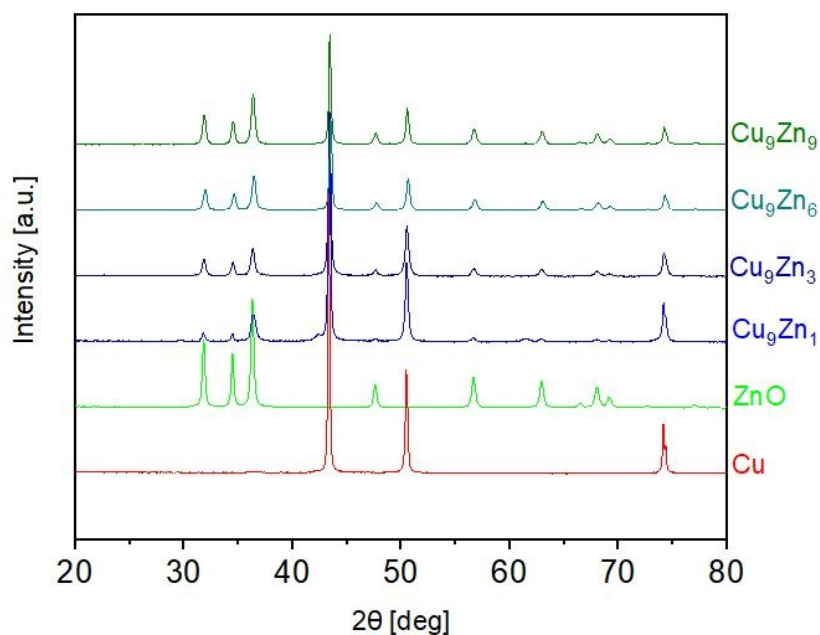


Figura 0.9: Spettri XRD di tutti i campioni.

L'abbondanza relativa delle specie chimiche presenti nei campioni è quantificata tramite ICP/OES (tab.0.3). Ciò verifica il rapporto atomico Cu/Zn ottenuto tramite il processo di sintesi assistito da microonde.

Table 0.3: Risultati analisi ICP/OES

Campione	Cu [wt. %]	Zn [wt. %]	Cu/Zn (rapporto atomico)	ZnO [wt. %]
Cu_9Zn_1	92,81	11,70	8,1	14,60
Cu_9Zn_3	75,84	22,70	3,4	28,30
Cu_9Zn_6	52,17	37,26	1,4	46,40
Cu_9Zn_9	44,65	41,06	1,1	51,20

I cambiamenti morfologici e composizionali dei materiali ZnO/Cu ne modificano le proprietà elettrochimiche rispetto agli elettrodi monometallici Cu e ZnO. La selettività del Cu è fortemente influenzata dalla presenza del ZnO (Fig.0.10); la presenza di diversi tipi di siti superficiali attivi per la CO_2RR limita la HER e sposta la produzione di CO da valori $< 10\%$ all'elettrodo Cu (a tutti i potenziali testati) verso un valore massimo $< 71\%$ per gli elettrodi Cu_9Zn_3 , Cu_9Zn_6 e Cu_9Zn_9 a $-1,1$ e $-1,0\text{V}$ (Tab.0.4). L'elettrodo ZnO produce circa 75% di CO a $-1,1$ e $-1,0\text{V}$.

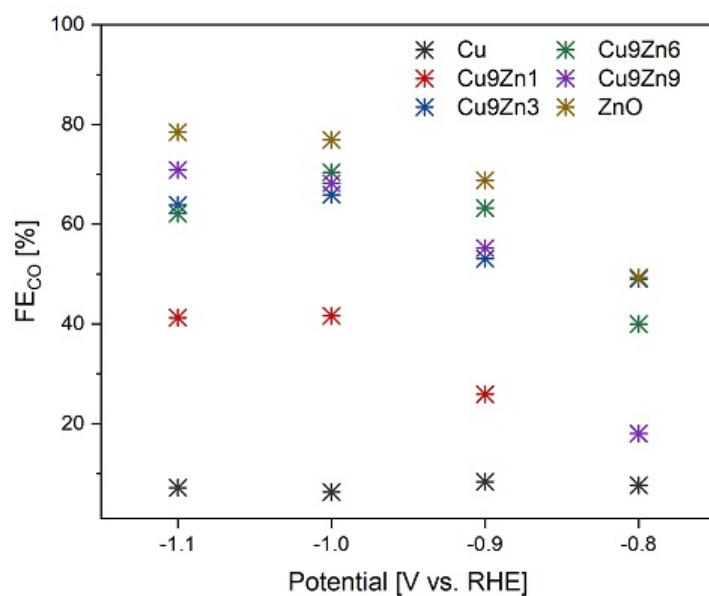


Figura 0.10: Confronto dei risultati della FE_{CO} tra tutti gli elettrodi.

Tabella 0.4: valori FE_{CO} [%].

Potenziale (V vs RHE)	Cu	Cu ₉ Zn ₁	Cu ₉ Zn ₃	Cu ₉ Zn ₆	Cu ₉ Zn ₉	ZnO
-0,8	7,63	18,01	49,03	39,99	18,04	49,30
-0,9	8,36	25,92	53,08	63,22	55,19	68,82
-1,0	6,30	41,64	65,89	70,39	68,22	76,91
-1,1	7,14	41,27	63,88	62,13	70,88	78,46

L'analisi della tabella 0.5 e della figura 0.11 evidenzia che i valori di densità di corrente j dell'elettrodo ZnO variano tra 5,08 e 5,99 mA/cm² a -1,0 e -1,1 V rispettivamente ($j^{Cu} = 12,83$ mA/cm² a -1,1 V). La velocità di reazione di una specie può essere calcolata con l'equazione

$$j_{CO}^{El} = FE_{CO} * j \quad (0.3)$$

dove j_{CO}^{El} è la velocità di reazione di CO per uno specifico elettrodo [mA/cm²] e j è la densità di corrente dell'elettrodo. Nel caso dei materiali ZnO/Cu, la conduttività delle particelle di Cu gioca un ruolo combinato con la selettività delle particelle di ZnO (Fig.0.12), formando un nuovo ambiente di reazione per la CO₂RR favorevole alla riduzione in CO con un valore maggiore di j_{CO} maggiore rispetto al catalizzatore a metallo singolo ($j_{CO}^{ZnO} = 4,70$ mA/cm² vs. $j_{CO}^{Cu_9Zn_9} = 5,88$ mA/cm² a -1,1 V (Tab.0.6).

Tabella 0.5: Valori della densità di corrente j [mA/cm²].

Potenziale (V vs RHE)	Cu	Cu ₉ Zn ₁	Cu ₉ Zn ₃	Cu ₉ Zn ₆	Cu ₉ Zn ₉	ZnO
-0,8	5,44	3,32	1,95	2,27	2,48	1,73
-0,9	7,90	5,25	2,92	3,85	4,27	2,95
-1,0	11,99	7,11	4,70	4,31	5,43	5,08
-1,1	12,83	9,33	5,71	6,19	8,29	5,99

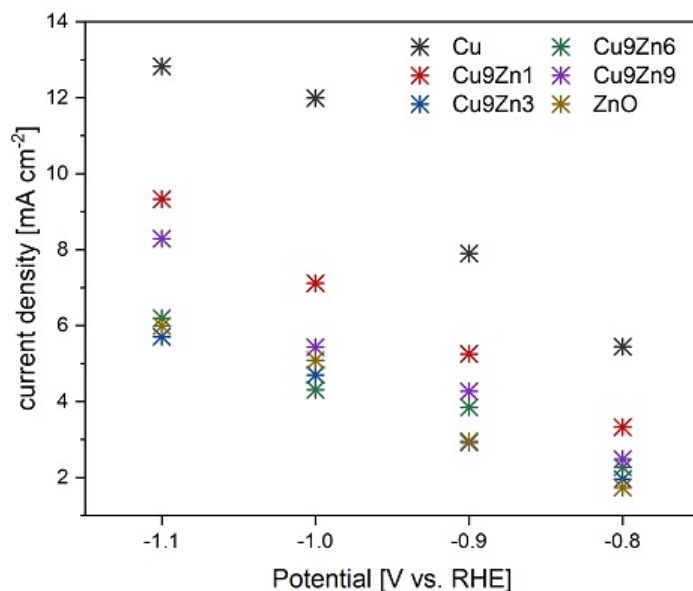


Figura 0.11: Confronto delle densità di corrente j tra tutti gli elettrodi.

Tabella 0.6: Valori di j_{CO}^X [mA/cm²].

Potenziale (V vs RHE)	Cu	Cu ₉ Zn ₁	Cu ₉ Zn ₃	Cu ₉ Zn ₆	Cu ₉ Zn ₉	ZnO
-0,8	0,41	0,60	0,96	0,91	0,45	0,85
-0,9	0,66	1,36	1,55	2,43	2,35	2,03
-1,0	0,75	2,96	3,10	3,03	3,70	3,91
-1,1	0,92	3,85	3,64	3,85	5,88	4,70

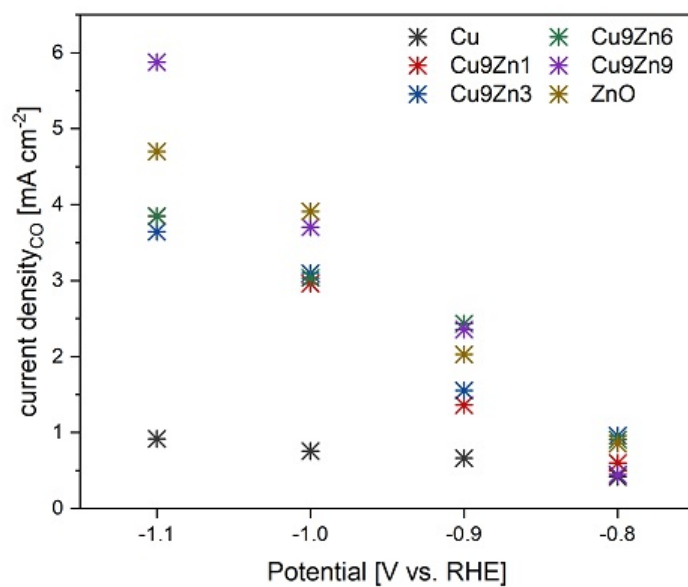


Figura 0.12: Confronto di j_{CO}^{EL} tra tutti gli elettrodi.

Conclusioni e futuri sviluppi

Lo scopo di questo lavoro è quello di sintetizzare e caratterizzare materiali per la CO₂RR. I catalizzatori sono stati sintetizzati attraverso la tecnica solvothermal assistita da microonde a partire da Cu(Ace) e Zn(Ace) con diversi rapporti stechiometrici Cu:Zn. Questa tecnica di sintesi è promettente per l'uso pratico poiché è rapida ed estensibile a reattori industriali, con un basso consumo energetico (rispetto a tecniche tradizionali) e buon controllo dei parametri di processo. Nonostante i numerosi progressi raggiunti negli ultimi anni nel campo della CO₂RR, l'utilizzo pratico di questa tecnologia è ancora lontano. Un'analisi tecno-economica dei dati effettuata da Verma et al. [14], evidenzia che, per essere fattibile, la CO₂RR necessita di elettrodi ad elevata durezza e valori di densità di corrente j superiori a 200mA/cm². A prescindere dai materiali utilizzati come elettrodi, valori così elevati di j sono difficili da raggiungere in un reattore in fase liquida (come la cella elettrolitica di questo studio), a causa della bassa solubilità della CO₂ nell'elettrolita (33mM) che limita il trasporto di massa di reagente all'elettrodo, arginandone la produttività. Al contrario, le celle in fase gas hanno recentemente mostrato prestazioni migliori, soprattutto riguardo la densità di corrente ($j > 100\text{mA}/\text{cm}^2$), rispetto alle celle in fase liquida (valori molto inferiori a 100mA/cm²) [15]. I principali tipi di celle in fase gas studiati recentemente sono due: la cella Membrane Electrode Assembly (MEA) e la cella microfluidica (figure 0.13a e 0.13b).



Figura 0.13: Rappresentazione schematica delle celle in fase gas.

Ulteriori analisi possono essere effettuate per approfondire il comportamento dei materiali sintetizzati e comprendere i meccanismi retrostanti la migliorata selettività e produttività verso la CO rispetto ai catalizzatori a metallo singolo. Tra le possibili analisi ci sono: Electrochemical Impedance Spectroscopy (EIS), scanning transmission electron microscopy (STEM) equipaggiata con Energy Dispersive X-ray Spectroscopy (EDS) e operando X-ray Absorption Spectroscopy (XAS). Queste analisi permettono di ottenere informazioni sulla cinetica della CO₂RR (EIS), sul ruolo delle specifiche specie chimiche nel processo di riduzione (STEM e EDS prima e dopo la reazione di riduzione) e sullo stato elettrochimico dei siti superficiali attivi durante la CO₂RR (operando XAS). L'unione di queste ulteriori informazioni con un modello della cinetica della CO₂RR può portare alla progettazione di catalizzatori più performanti, con densità di corrente adeguate e con il giusto rapporto di H₂/CO prodotti. Sostituendo i metodi tradizionali di sintesi di materiali catalizzatori con la tecnologia microonde, si unisce l'uso di un metodo di sintesi eco-sostenibile e estensibile a processi industriali con l'obiettivo di trovare nuovi materiali catalizzatori adatti allo sfruttamento della riduzione elettrochimica della CO₂.

Abstract

Nowadays, global warming and CO₂ emissions and its concentration in the atmosphere are central topics in politics and scientific debate. While finding alternative source of energy can be a good strategy to mitigate new CO₂ emissions, transformation of CO₂ in valuable chemicals with the electrochemical CO₂ reduction reaction (CO₂RR) can reduce the already enormous amount of atmospheric CO₂ and can also minimize the emissions with respect of other industrial processes.

Electrochemical CO₂RR presents several advantages over other approaches. Firstly, relative to the eco-compatibility of the process, this method can use green chemicals as electrolytes [3] and electricity from renewable sources, not contributing to CO₂ emissions while transforming it. Secondly, the conversion rate is directly related to the electrode potential and can be tuned by applying different potentials [4, 5]. Ultimately, the reactor of the process can be extensible to industrial demands. The economic feasibility of the electrochemical CO₂RR requires catalyst materials able to reduce the overpotential of the reaction and to promote efficiently the formation of specific reaction products (Tab.0.7), with good stability over the reaction time. The precursors and the production process of these materials need also have reasonable costs for the purpose of the mass-scale implementation. Among all the possible reaction products of the CO₂RR, the reduction CO₂ → CO is kinetically favorable because only two electrons are required to complete it [8]. In aqueous solution, the CO₂RR competes with the cathodic half-reaction of hydrogen evolution reaction (HER). The H₂/CO mixture with minor amount of H₂ can be further tuned by adding H₂ in order to get a syngas with a desired H₂/CO ratio. In this field, Au- or Ag-based catalysts show the best performance for the CO₂RR to CO [4, 8, 9, 10], but the precursors are expensive, limiting the mass-scale implementation. Cu-based materials are less expensive, but the selectivity of these catalysts need to be tuned with different approach, like particles size and shape control or alloying elements, properties that all contribute to the performance of nanostructured Cu-based catalysts [5, 6, 12, 16, 17].

Table 0.7: Several electrochemical CO₂RR products and the standard reduction potentials (E^0) [5, 7].

Product	Reaction	E^0 [V vs. RHE]
CO	$\text{CO}_2 + 2\text{e}^- + 2\text{H}^+ \longrightarrow \text{CO} + \text{H}_2\text{O}$	-0.11
HCOOH	$\text{CO}_2 + 2\text{e}^- + 2\text{H}^+ \longrightarrow \text{HCOOH}$	-0.22
CH ₄	$\text{CO}_2 + 8\text{e}^- + 8\text{H}^+ \longrightarrow \text{CH}_4 + 2\text{H}_2\text{O}$	+0.17
C ₂ H ₄	$\text{CO}_2 + 12\text{e}^- + 12\text{H}^+ \longrightarrow \text{C}_2\text{H}_4 + 4\text{H}_2\text{O}$	+0.08
CO ₂ ^{*-}	$\text{CO}_2 + \text{e}^- \longrightarrow \text{CO}_2^{*-}$	-1.5
H ₂	$2\text{H}^+ + 2\text{e}^- \longrightarrow \text{H}_2$	0.0

All things considered, a material suitable for the CO₂RR should present the following characteristics:

- High faradaic efficiency (FE) for the desired product (selectivity): FE is defined as the ratio of the total electrons (coulombs, n) required to form a certain amount of product (N) to the total electrons (coulombs) over the reaction time, $FE(\%) = \frac{nNF}{Q} * 100$
- High current density j : this value describes the reaction rate of the target product, $j_{CO} = FE_{CO} * j$
- Low overpotential (energy efficiency)
- Good stability and durability
- Affordability of both the precursor materials and the production process of the electrode

The aim of this work is the evaluation of ZnO-modified Cu (ZnO/Cu) catalysts with different stoichiometric quantities (Tab.0.8) for the CO₂RR. The Cu-based materials are synthesised in a one-step microwave-assisted solvothermal route, which is fast, reproducible, scalable and energetically convenient. All the synthesised materials are characterised via Field-Emission Scanning Electron Microscopy, X-Ray Diffractometry, and Inductively Coupled Plasma/Optical Emission Spectrometry, while the prepared electrodes are characterised via Cyclic Voltammetry and Chronoamperometry coupled with Gas Chromatography for products evaluation. The comparison between the ZnO/Cu materials and both the reference single-metal materials highlights the influence of the addition of ZnO on the performance of Cu electrodes.

Table 0.8: Sample prepared with different amount of Cu and Zn precursors.

Samples	Cu(Ace) [mg]	Zn(Ace) [mg]
Cu	900	0
Cu ₉ Zn ₁	900	120.6
Cu ₉ Zn ₃	900	361.8
Cu ₉ Zn ₆	900	723.7
Cu ₉ Zn ₉	900	1085.5
ZnO	0	1085.5

The selectivity of the Cu electrode is heavily influenced by the ZnO presence (Fig.0.14); different types of active sites for CO₂RR inhabit the HER and shift the production of CO from < 10% (at all the tested potentials) at the Cu electrode to a maximum value of about 70% for Cu₉Zn₃, Cu₉Zn₆ and Cu₉Zn₉ at certain potentials. The ZnO electrode produces around 75% of CO at different potentials, but the presence of Cu species in ZnO/Cu electrodes increases the current density values of these modified electrodes (Figs.0.15a and 0.15b), achieving better results compared to single-metal electrode.

The information gathered with this work, together with further analyses in the working state of the electrodes and a model of the kinetic of the CO₂RR, could lead to better designed catalysts with favourable current density values and the higher CO production ratio. The microwave-assisted technology implemented for the synthesis of catalyst materials, instead of classic solvothermal methods, combines a upscalable and environmental-friendly synthesis method to the main goal of finding new catalyst materials suitable for the electrochemical CO₂RR exploitation.

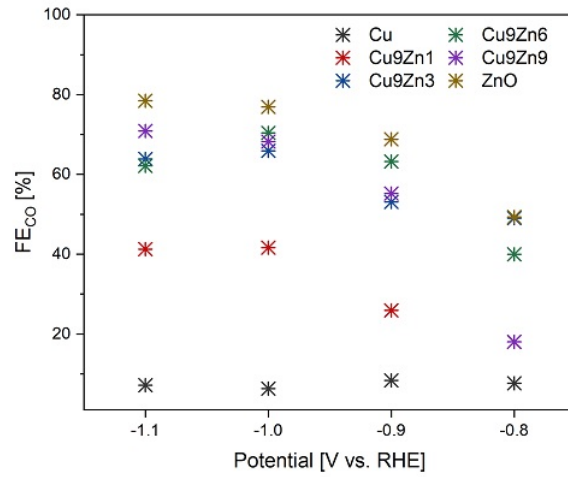
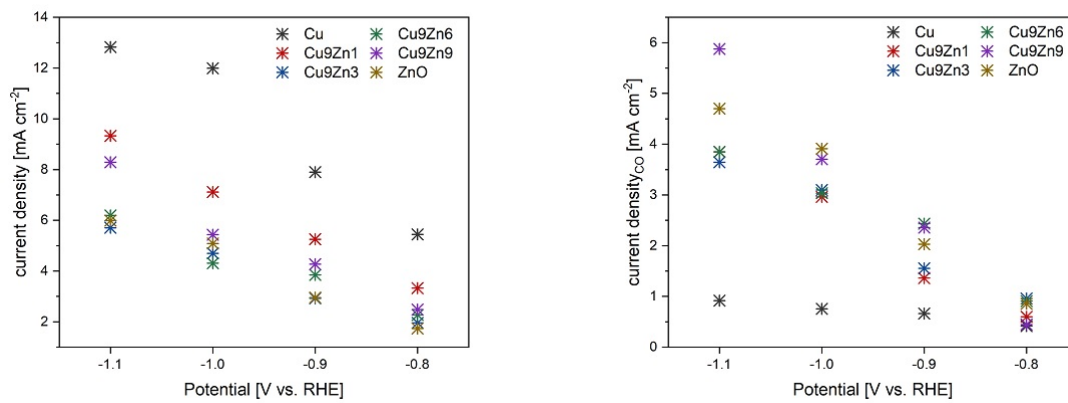


Figure 0.14: Faradaic Efficiency towards CO production of all the electrodes.



(a) Current density j values of all the electrodes.

(b) Reaction rate of CO (j_{CO}^{EL}) of all the electrodes.

Figure 0.15: Results comparison.

1 Introduction

1.1 Greenhouse effect and greenhouse gases

Energy travels from the Sun to the Earth. Some of this solar energy is reflected back into the space by obstacles such as atmosphere and clouds, while some of it is absorbed by these obstacles. Most of this solar energy reaches the earth and is absorbed by the earth surface. The earth surface then releases this energy as heat radiation into the atmosphere. Greenhouse gases in the atmosphere absorb most of this energy and release it, maintaining a high equilibrium temperature of the earth surface. This natural process, called greenhouse effect, allows the earth's temperature to be suitable for life and not below freezing. However, anthropogenic greenhouse gases emissions into the atmosphere strengthen this effect, overwarming the climate of our planet. Greenhouse gases absorb the energy because of their molecular morphology, more complex than other gas molecules in the atmosphere. In fact, most of the gas in the atmosphere is nitrogen and oxygen. The two atoms of these molecules are tightly bounded, giving rise to high frequency molecular vibration which barely absorb heat; hence, they do not contribute to the greenhouse effect.

There are different types of greenhouse gases, such as water vapour, carbon dioxide, methane, nitrous oxide and fluorinated gases. All of these gas molecules are made of three or more atoms and are opaque to infrared radiation. They can absorb heat and sequentially release the radiation to a nearby greenhouse gas molecule, keeping the heat near the earth's surface.

- **Carbon dioxide (CO₂):** released primarily by fossil fuel use, it is also emitted from deforestation, cement production, land clearing and degradation of soils due to agriculture. It is the least dangerous among these gases although it is the most abundant (Fig 1.1).
- **Methane (CH₄):** agricultural activities, farm animals, waste management, energy use, and biomass burning all contribute to CH₄ emissions in the atmosphere.
- **Nitrous oxide (N₂O):** the primary source of N₂O emissions are fertilizer use in agricultural activities. Fossil fuel combustion also generates N₂O.
- **Fluorinated gases (F-gases):** this category includes hydrofluorocarbons (HFCs), perfluorocarbons (PFCs), and sulphur hexafluoride (SF₆), released by industrial processes, refrigeration and consumer products.

According to Muntean et al. [1], greenhouse gases emissions trend has been increasing since the beginning of 21st century in contrast with the previously thirty years, due to the increase in CO₂ emissions from emerging economies and mostly caused by fossil fuel combustion. As clearly shown in figures 1.2 and 1.3a, the industrial and economic growth of countries like China and India contributes to this rate increase, but the amount of CO₂ pro capita per year of other countries like USA and Russia is still higher (figure 1.3b) and their contribution to the total amount of CO₂ in the atmosphere through the years is even more considerable.

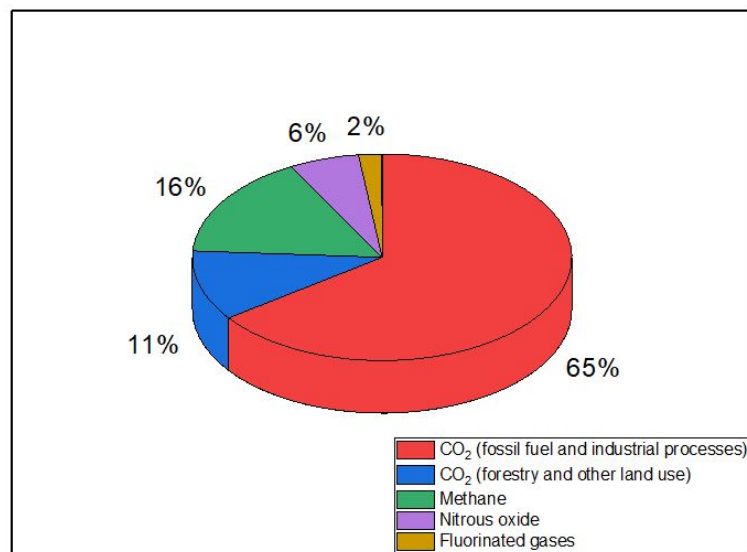


Figure 1.1: Global greenhouse gases emissions. Data from Pachauri et al. [2].

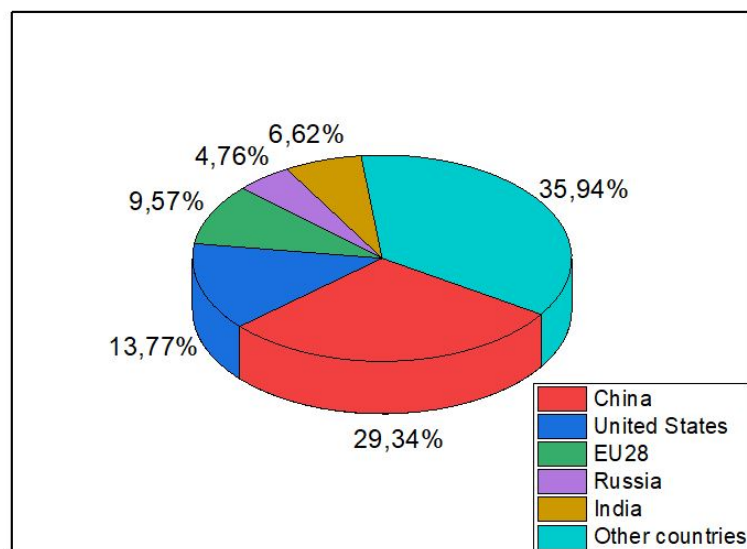


Figure 1.2: CO₂ emissions by country divided by the total CO₂ emissions. Data from Muntean et al. [1].

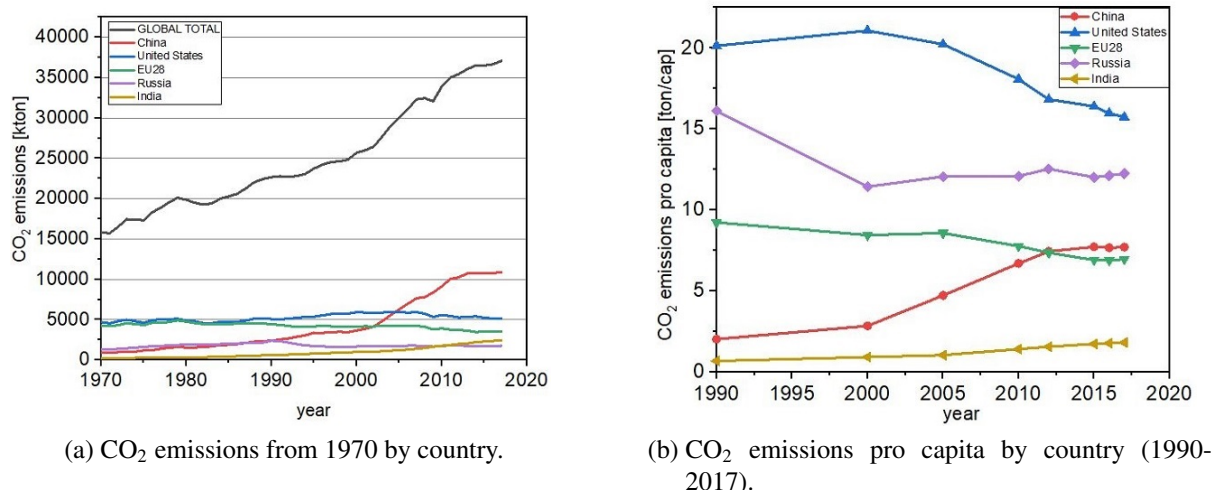


Figure 1.3: Data from Muntean et al. [1].

1.2 Strategies of mitigating CO₂ effect

As mentioned previously, CO₂ is not the most dangerous gas to the global warming effect, but it gives the biggest contribution because of its abundance. Consequently, since the end of the Seventies, many politics and studies are dedicated to limit the global CO₂ emissions and to reduce the CO₂ concentration in order to mitigate the global warming. The fossil-fuel combustion is our primarily source of energy until now and this process contributes to most of the CO₂ emissions. Hence, searching for alternative sources of energy is a possible solution to limit the CO₂ emissions. To decrease atmospheric CO₂ concentration to a desired and not dangerous value, trapping and transformation of the atmospheric CO₂ are necessary. This is a highly inviting approach because it can reduce the carbon footprint correlated to fossil-fuel-powered processes, allowing sustainable exploitation of current fossil-fuel resources, and can generate revenue from a waste gas. The CO₂ reduction reaction (CO₂RR) permits to synthesize valuable chemicals from CO₂ and it can be accomplished by different methods, including chemical, photochemical, electrochemical, biological and inorganic transformations.

This study dwells on the reduction of CO₂ via electrochemical methods since it presents several advantages over other approaches. Firstly, relative to the eco-compatibility of the process, this method can use green chemicals as electrolytes [3] and electricity from renewable sources, not contributing to CO₂ emissions while transforming it. Secondly, the conversion rate is directly related to the electrode potential and can be tuned by applying different potentials [4, 5]. Ultimately, the reactor of the process can be extensible to industrial demands.

The electroreduction is a non-spontaneous reaction achieved in an electrolytic cell (figure 1.4) by applying electrical energy to the system. An electrolytic cell is a three-component parts system: two electrodes (anode and cathode) and an electrolyte in which the electrodes are immersed. When an external electrical voltage with correct polarity and sufficient magnitude is applied to the electrolytic cell, the reduction reaction occurs at the cathode, while the oxidation arises at the anode, allowing the decomposition of normally stable or inert chemical compounds that would not occurs spontaneously.

To measure the energy needed to reduce or oxidize a chemical compound, standard electrode potentials (E^0) are commonly used. These half-cell potentials usually refer to the standard hydrogen electrode (SHE). It is defined that the SHE has a potential of 0.00V at standard condi-

tions (an acid electrolyte with a pH value of 0, gaseous hydrogen atmosphere with a pressure of 10^5 Pa and a temperature of 25°C). A reversible hydrogen electrode (RHE) can be used instead of a SHE in order to overcome the difficulties of keeping a system in standard conditions and the SHE dependence to the electrolyte's pH. The applied potentials, referred to the RHE instead of the SHE, are comparable in the electrolytes with various pH values. When a different reference electrode is used during the test, the applied potential can be calibrated to that refers to the RHE according to the Nernst equation:

$$E (V \text{ vs. RHE}) = E_{(vs.ref.)} + E_{ref.}^0 (V) + 0.059 * pH \quad (1.1)$$

where E is the potential applied at the electrode and E^0 is the standard potential of the reference electrode versus the SHE.

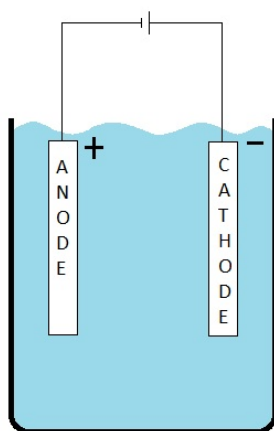


Figure 1.4: Scheme of an electrolytic cell.

1.3 Aim of the work

The purpose of this work is the evaluation of ZnO-modified Cu (ZnO/Cu) catalysts with different stoichiometric quantities for the CO_2RR . In chapter 2 are introduced the generalities of both the electrocatalysts and the CO_2RR , with a focus on the state-of-the-art of Cu-based catalysts. Chapter 3 describes the synthesis of the materials through each individual step and the different characterization's techniques carried out on the samples. The Cu-based materials are synthesised in a one-step microwave-assisted solvothermal route, which is fast, reproducible, scalable and energetically convenient. The conventional synthesis used in most of the materials presented in chapter 2 usually need several thermal or electrochemical synthetic steps. All the synthesised materials are characterised via Field-Emission Scanning Electron Microscopy, X-Ray Diffractometry and Inductively Coupled Plasma/Optical Emission Spectrometry, while the prepared electrodes are characterised via Cyclic Voltammetry and Chronoamperometry coupled with Gas Chromatography for products evaluation. In chapter 4, all the results of the characterization's techniques are presented and compared to better understand the ZnO and Cu effect on the CO_2RR in order to guide further developments. Ultimately, in chapter 5, the future developments on the CO_2RR topic are introduced, along with some advanced characterization's techniques that might help the material's design and increase our understanding on the CO_2RR .

2 Electrochemical CO₂ reduction reaction

2.1 Generalities

The high stability of CO₂ (binding energy $EB = 750\text{kJ/mol}$, compared to C–H bond $EB = 411\text{kJ/mol}$, C–C bond $EB = 336\text{kJ/mol}$, C–O bond $EB = 327\text{kJ/mol}$) implicates that an high amount of energy is required to break the double bond C=O, the first step of every reduction process [6, 7]. Materials and catalysts engineering allows to reduce this energy by designing appropriate catalysts.

As shown in Tab.2.1, electrochemical CO₂RR in an aqueous solution involves multiple electron/proton transfer reactions [5, 6] and promotes the formation of various products. The products can be divided into two main groups: C₁ compounds with one carbon atom and C₂ compounds with two carbon atoms. C₁ products include carbon monoxide (CO), formic acid (HCOOH), formaldehyde (HCHO), methanol (CH₃OH) and methane (CH₄). C₂ products include oxalic acid (HOOC-COOH), ethylene (CH₂CH₂), ethane (CH₃CH₃) and ethanol (CH₃CH₂OH). Other hydrocarbons with more carbon atoms can be also formed.

Table 2.1: Several electrochemical CO₂RR products and the standard reduction potentials (E^0) [5, 7].

Product	Reaction	E^0 [V vs. RHE]
CO	$\text{CO}_2 + 2\text{e}^- + 2\text{H}^+ \longrightarrow \text{CO} + \text{H}_2\text{O}$	-0.11
HCOOH	$\text{CO}_2 + 2\text{e}^- + 2\text{H}^+ \longrightarrow \text{HCOOH}$	-0.22
CH ₃ OH	$\text{CO}_2 + 4\text{e}^- + 4\text{H}^+ \longrightarrow \text{CH}_3\text{OH} + 2\text{H}_2\text{O}$	+0.02
CH ₄	$\text{CO}_2 + 8\text{e}^- + 8\text{H}^+ \longrightarrow \text{CH}_4 + 2\text{H}_2\text{O}$	+0.17
C ₂ H ₄	$\text{CO}_2 + 12\text{e}^- + 12\text{H}^+ \longrightarrow \text{C}_2\text{H}_4 + 4\text{H}_2\text{O}$	+0.08
CO ₂ * ⁻	$\text{CO}_2 + \text{e}^- \longrightarrow \text{CO}_2^{*-}$	-1.5
H ₂	$2\text{H}^+ + 2\text{e}^- \longrightarrow \text{H}_2$	0.0

According to Xie et al. [6], during the CO₂RR process three main steps occur on the catalyst's surface:

1. adsorption and interaction of CO₂ with surface atoms of the catalyst
2. catalyst-initiated activation of CO₂ and subsequent reduction
3. product desorption from the catalyst's surface and recovery of the active sites

2.2 Electrocatalysts

As introduced above, transferring one electron to the adsorbed CO₂ molecule to activate it (generating the radical CO₂^{*-}) is believed to be the rate-determining step of the CO₂RR on transition metal-based catalysts because of the high activation barrier (Tab.2.1) needed for this reduction [6]. Because of this first limiting step, CO₂ can not be reduced to other products at the potentials reported in table 2.1. The difference between the real potential required to reduce CO₂ molecules to a specific product and the ideal thermodynamic one is called overpotential [8]. Other than this surplus energy required to activate the adsorbed CO₂ molecule, the overpotential is also caused by ohmic losses from both the electrolyte and the electrodes as well as the mass transport limitations of the reactants and products at the electrode/electrolyte interface. The first role of the catalyst is to reduce the overpotential in order to achieve the desired reaction with less amount of electrical energy supplied to the electrolytic cell [4, 8]. Another principle role of the catalyst is to enhance the selectivity of the reduction reactions under the applied potentials. As shown in table 2.1, the various pathways of the CO₂RR and the hydrogen evolution reaction (HER) occur at similar standard potentials. Hence, a catalyst is essential to selectively reduce the CO₂ and to hinder the HER. Furthermore, it must drive the CO₂RR under a specific pathway in order to obtain a high selectivity for a desired product. In general, once CO₂^{*-} forms on the catalyst's surface, its reactivity in this state controls the distribution of final products. Both early and later studies of electrochemical CO₂RR [4, 8, 9, 10] on various metal-based electrodes found that the radical CO₂^{*-} interacts with the surface of the catalyst in different ways, depending on the intrinsic electronic surface's properties of the material (that affects also the activation barrier of the process). On the surface of Au or Ag catalyst, the radical CO₂^{*-} is bound to the metal surface by the carbon atom, resulting in a protonation/reduction at the O-position and leading to the formation of the intermediate *COOH. This species can be further reduced to *CO and it desorbs as CO product, due to the weak bind to the metal catalyst. This behaviour has been found also for catalysts based on Zn and Ga. On the surface of a Sn or In catalyst the radical CO₂^{*-} is bound to the metal surface by the oxygen atom, resulting in a protonation/reduction at the C-position and leading to the formation of formate HCOO⁻ and then the desorption of formic acid. This behaviour has been found also for catalysts based on Pb, Hg and Cd. Electrodes based on Cu show a different behaviour from any of these two groups of metals. In fact, Cu can catalyse the formation of carbon monoxide, formic acid and also hydrocarbons, because of the moderate binding energy of *CO to Cu surface. Other metals, such as Ni, Fe, Pt, and Ti are not fitted for the CO₂RR in aqueous media, because they are more active in reducing water to produce H₂ [8]. Despite the values in the table 2.1, among these reactions, the reduction of CO₂ to CO is kinetically favourable because only two electrons are required to complete the transformation [8]. As a result, many studies have been published on this subject, trying to find cheaper materials than Au or Ag for the production of the electrode, as well as more economically convenient and scalable production methods for real industrial applications.

2.3 Hydrogen evolution reaction and syngas

Generally, since CO₂RR is conducted in aqueous solution, the reduction of CO₂ competes with the HER that can even completely replaces the CO₂RR. HER is a cathodic half-reaction, and it has comparable thermodynamic potential with the CO₂RR (0V vs. RHE). It progresses at lower overpotential [18]. Thus, it is almost inevitable to contemporarily generate H₂ during the CO₂RR [8]. The HER side reaction is typically undesired because it occupies electrons and

active sites, decreasing the efficiency of the CO₂RR process. However, considering syngas as the target product, the HER becomes as desirable as the CO₂RR. Syngas is synthetic gas, a mixture of H₂ and CO, which can be used to generate ammonia, alcohols and other hydrocarbons via heterogeneous Fischer-Tropsch catalysis [8]. In fact, depending on the H₂/CO ratio, syngas can be used to generate different products such as chemical intermediates for fertilizer (NH₃), pharmaceutical, plastics and solvents production and also for liquid fuels production (CH₃OH, CH₄, biodiesel and other fuels). Nowadays, Syngas is primarily produced from natural gas by steam reforming, a process catalyzed by nickel-based catalysts that requires high temperature, pressure and of course a source of methane [19]. Hence, developing an electrochemical process that is feasible at mild conditions and fed by green electrical energy from renewable sources and possibly produces syngas with controllable H₂/CO ratio can be very attractive [8].

2.4 Efficiency of the electrodes and CO₂RR parameters

Concerning the performance of an electrocatalyst, the current density (j) is the most used parameter to describe the reaction rate at the electrode. The definition of current density is "the electric current per unit of surface or geometric area of the electrode; the current density vector is defined as a vector whose magnitude is the electric current per cross-sectional area at a given point in space and applied potential, its direction being that of the motion of the charges at this point" [11]. For a given electrocatalyst at a specific potential, the reaction rate of the electroreduction is higher at high current density values. Consequently, a given electrode could be suitable for CO₂RR if it produces a high current density (related to the final product of the reaction). As introduced in section 2.2, the high current density should be achieved at relatively low overpotential values.

Except the reaction rate and overpotentials, selectivity is also an important parameter. In section 2.1, several CO₂ reduction products and side-product (H₂) are described. The selectivity of a catalyst is expressed by the faradaic efficiency (FE). FE is defined as the ratio of the total electrons (coulombs) required to form a certain amount of product to the total electrons (coulombs) over the reaction time,

$$FE(\%) = \frac{nNF}{Q} * 100 \quad (2.1)$$

where n is the number of electrons transferred in the faradaic process, N is the amount of the generated products in the process, F is the faradaic constant (96485.33C/mol) and Q is the charge. For example, for CO production efficiency (2 electrons involved in the process, like HER)

$$FE_{(CO)} = \frac{2 * F * mol\ CO\ produced}{j * A * t} \quad (2.2)$$

where j is the current density [A/m²], A is the electrode area [m²] and t is the reaction time [s]. Ideally, at the end of the electroreduction, the sum of the FE values for all the products should be 100% [8].

The overall performance and product distribution of CO₂RR are influenced by several parameters. As mentioned in Sec.2.2, the material (or materials) used as catalyst and in particular their intrinsic electronic surface's properties play a key role in affecting the efficiency and selectivity of CO₂RR. The particles size of the catalyst material affects also the selectivity and the reactivity of the catalyst, determining both the type of active sites and their density (more details in Sec.2.5.1). This size-dependent behaviour of the CO₂RR has been both theoretically and experimentally inspected for materials like Cu, Ag, Au. For the same reason, the

morphology of the particles can modify catalyst's selectivity and reactivity (Sec.2.5.2). Some particular structures (i.e. dendrite-like structures) can facilitate the mass transfer of reactant to the catalyst, increasing the efficiency of the reaction [5]. The electrolytic cell (EC) configuration affects the charge transfer phenomena, modifying the efficiency of the CO₂RR. Because there is not a standardized method for this process, it's difficult to compare different experiments and EC configurations [8]. The goal remains to accomplish the CO₂RR efficiently at the lowest overpotential. In this work experiments are carried out in a two-compartment three-electrode cell. An ion exchange membrane was used to separate the two compartments (anodic and cathodic compartments) and the catalyst particles dispersed on a Gas Diffusion Layer (GDL) as the cathode (more details in Sec. 3.2.2). The chosen conductive aqueous electrolyte, generally composed of cations like Na⁺, K⁺ and anions like bicarbonate (HCO₃⁻) or hydroxide (OH⁻), can have a deep effect on the current density and selectivity of the CO₂RR. The conductivity of the electrolyte affects the current density while the pH value at the electrode influences both the cell overpotential and the selectivity of products [8]. Pressure and temperature also affect the CO₂RR, modifying the solubility of CO₂ in the electrolytic solution; a temperature increase leads to lower overpotential because the conductivity increases and the electrode/electrolyte contact also increases, due to lower size of gas bubbles in the electrolyte. Despite these behaviours, increasing the temperature decreases the solubility of CO₂ in the electrolytic solution, reducing the overall amount of reactant at the catalyst's surface [8]. At high pressure the CO₂ solubility increases, but it's difficult to build an electrolytic cell capable of handling high pressure in working condition [8]. All things considered, a material suitable for the CO₂RR should present the following characteristics:

- High current density j (reaction rate)
- Low overpotential (energy efficiency)
- High FE for the desired product (selectivity)
- Good stability and durability
- Affordability of both the precursor materials and the production process of the electrode

2.5 CO₂RR on Cu-based catalysts and state-of-the-art

After the discovery that Cu foils treated by plasma oxidation are suitable for CO₂RR with a certain control on product distribution, many studies were made to find more active Cu-based catalysts [6]. The improvement of nanoparticles (NP) synthesis with control on NP morphology, dimension, structure and composition has led to an investigation of such topics, demonstrating higher selectivity and activity for CO₂RR with nanostructured Cu-based electrodes. All these studies have found out that NP size (or nano-porous structures), shape, alloying elements and NP support materials all contribute to the performance of nanostructured Cu-based catalysts.

2.5.1 Nano-porous structures and NP size effect

The behaviour of the plasma-oxidized Cu foil has been related to the presence of metastable grain boundaries on the surface. Because of that, studies were made on porous structures to better control the reaction pathways of CO₂RR. A first example is a hierarchical porous Cu nano-foam with pore size of 20 – 50μm, produced by electrochemical deposition of Cu with

H₂ bubbles as soft template [20]. When used as catalyst, the Cu nano-foam produces HCOOH and CO ($FE_{HCOOH} = 37\%$, $FE_{CO} = 10\%$ at $-1.5V$ vs. Ag/AgCl reference), increasing the performance compared to a smooth Cu electrode ($FE_{HCOOH} = 24\%$ at $-1.5V$ vs. Ag/AgCl). To better understand the pore size-dependent performance of CO₂RR, ordered nano-porous Cu structures with uniform pore sizes were synthesised via magnetron sputtering of Cu on porous Al₂O₃ templates with different pore size (300nm wide and 40nm long pore structure, $30 \times 40nm$ and $30 \times 70nm$) [21]. The porous Cu $300 \times 40nm$ gave CO and CH₄ with a total $FE \approx 24\%$, the $30 \times 40nm$ sample produced mainly C₂H₄ with $FE = 38\%$, while the $30 \times 70nm$ structure produced C₂H₆ ($FE = 46\%$), showing that increasing pore depth and decreasing pore width led to the formation of C₂ products. These differences can be associated to the reaction condition caused by pore dimension. In normal condition with KHCO₃ as electrolyte, HCO₃⁻ neutralizes the OH⁻ generated during the CO₂RR and HER, while the narrow porous structure restricts the HCO₃⁻ diffusion, leading to a local increase of the pH value thus facilitating the formation of C₂ products [6]. Moreover, narrow porous structures limit the mass transport of reactants to the active sites of the catalyst.

To overcome this limitation NPs have been investigated as catalysts. On the surface of a NP, the coordination number and the chemical interaction energy of every atom depend on its position in the crystal lattice: atoms on different crystal planes, along the edges and on the corners of the crystal lattice have distinct properties [6]. As a result, with the control of the surface structure and size of the NPs is theoretically possible to tune their catalysis reactions. Many studies were made to correlate NPs dimension and CO₂RR selectivity. In particular models of spherical Cu NPs with face-centered cubic structure and dimension from 1 to 18nm were constructed to attain the ratios of surface atoms with different coordination numbers [16]. NPs with dimension 6 – 18nm showed high activity and selectivity towards hydrocarbons (mainly CH₄), while NPs smaller than 6nm exhibited activity and selectivity towards H₂ and CO. This difference can be attributed to the ratio of surface atoms with different coordination numbers. In the first case (6 – 18nm), atoms with coordination number greater than 8 account for $\approx 70\%$ of surface atoms, while in the second case the ratio of low-coordinated atoms (coordination number smaller than 8) increases considerably. CO₂, CO and atomic H are strongly bound to low-coordinated surface atoms, not promoting the hydrogenation of CO thus producing H₂ and CO [6].

2.5.2 NP shape effect

The importance of Cu crystal facets exposure on the selectivity of CO₂RR is demonstrated by several studies on single crystal Cu electrodes [6, 17]. The effect of the facets exposure can be attributed to the different properties of atoms in distinct space positions. These studies show that Cu(111) facet promotes the formation of CH₄ and, in some cases, CO, while Cu(100),(110),(911),(711),(511) catalyse CO₂RR to C₂ products (C₂H₄ and C₂H₅OH). Considering that, the shape-controlled synthesis of Cu NPs can increase the efficiency of CO₂RR for a specific final product.

As was mentioned in section 2.4, the shape of the particles can also affect the CO₂RR reaction rate, facilitating the mass transfer of reactant to active sites [5].

2.5.3 NP alloying elements effect

Several studies have proved that pairing two or more metals with Cu can modify the selectivity of the CO₂RR, varying the chemical environment around the Cu atoms thus tuning binding en-

ergies and affinity of CO₂RR intermediates (*CO, *COOH, *CHO etc.) [12]. These variations depend strongly on the nature of the other metal and, by extension, the formation of different active sites on the catalyst's surface.

Coupling Cu with Au, Ag, Zn and Cd leads mainly to the production of CO with FE values generally higher than the single-metal catalyst [12]. These modifications can be associated with the high oxygen affinity of Cu (*COOH stabilization), the low binding energy of *CO with these metals and their weak hydrogen affinity that limits the HER. Pairing Cu with Sn or In promote the production of CO and HCOOH, depending on which metal contributes the most to the CO₂RR active sites formation [12]. When Sn or In dominate, HCOOH is the major reduction product, possibly due to the stabilization of *OCHO and the formation of formic acid through this intermediate. When Sn or In have a limited contribution, CO is produced at high FE values, perhaps because *COOH is better stabilized than *CO, lowering the energy barrier to CO formation (like Au, Ag, etc.). When Cu is coupled with Pd, the product selectivity depends strongly on the structure of the system [12]. With regular arrangement (i.e. Pd₇Cu₃ and CuPd₃) the major product is CO with max $FE \approx 90\%$ (*COOH stabilization). On the phase-separated Cu–Pd nanoparticles, C₂ products are generated due to C–C coupling facilitated by Cu active sites. Coupling Cu with Pt or Ni leads to the production of CH₄ and C₂H₄ with FE values of $\approx 20\%$ and $\approx 7\%$ respectively, although few examples exist in the literature [12].

Overall, the connection between the chemical composition of the alloy and its CO₂RR activity and selectivity depends on the binding energies of the intermediates on the catalyst [12].

2.5.4 Support material effect

The Cu NPs need to be supported on a material in order to stabilize them against aggregation and to assure desired conductive properties of the electrode. Typical support materials are carbon black, carbon nanotubes and graphene, but other types of supports are studied, including MoS₂ and polyaniline [6]. For example, the same 7nm Cu NPs were tested in identical reaction condition on a conventional carbon support and on a pyridinic nitrogen-doped graphene support [6]. With carbon support, these NPs produced mainly C₂H₄ ($FE = 6.3\%$ at $-1.1V$), while on the nitrogen-doped graphene the product selectivity depends on the applied potential: at $-0.8V$ the CO₂RR produces HCOOH ($FE = 62\%$), but at $-0.9V$ this catalyst produces hydrocarbons (CH₄, C₂H₄ and C₂H₆) with increased activity and selectivity towards C₂H₄ ($FE = 19\%$) compared to carbon-supported Cu NPs. The pyridinic nitrogen-doped graphene support is a source of Lewis basic sites that promote the concentration of more proton/hydrogen around Cu atoms, promoting C–C coupling and helping the conversion of *COOH to CO* and further to CH_xO* [6].

3 Materials and methods

3.1 Synthesis

3.1.1 Microwave-assisted solvothermal synthesis

In recent years, the interest in environmental-friendly chemistry has risen greatly. This means the use of non-toxic and renewable precursors, low energy consumption processes and minimization of generated waste. In this field microwave-assisted synthesis can be a recommended process due to its high product yields efficiency, the reduction of generated waste and its time and energy-saving properties, compared to traditional heating methods [13]. Furthermore, this process is scalable for mass-scale production simply by enlarging the reactor and the precursor quantities.

Solvothermal microwave-assisted synthesis uses electromagnetic radiation in the microwave frequency range (300MHz to 300GHz) to heat polar molecules by dielectric heating. It is performed in a closed vessel with organic medium at high pressures and, commonly, at higher temperatures than the boiling temperature of the solvent [22]. The oscillating electromagnetic field generated from microwave radiation makes all the polar molecules move and rotate to align to it, thus increasing the kinetic energy of the system. Rotating molecules collide with other molecules distributing the energy to adjacent molecules and atoms in the system and therefore transforming this energy into heat by friction [23]. The physics of the process allow to heat the target compounds without heating the entire furnace and reactor and thus to save time and energy.



Figure 3.1: The microwave oven used for the synthesis of the materials: a Milestone START-Synth with temperature and pressure control.

3.1.2 Materials used

The precursors used for the synthesis of the materials are: Copper(II) acetate hydrate (Cu(Ace), $\text{Cu}(\text{CO}_2\text{CH}_3)_2 \cdot x\text{H}_2\text{O}$, 98%), Zinc(II) acetate dihydrate (Zn(Ace), $\text{Zn}(\text{CO}_2\text{CH}_3)_2 \cdot 2\text{H}_2\text{O}$, $\geq 98\%$), sodium hydroxide (NaOH, 98 %), ethylene glycol (EG, $(\text{CH}_2\text{OH})_2$, 99.8 %), water and ethanol (EtOH). These materials were purchased from Sigma-Aldrich Inc. and were used as received.

3.1.3 Preparation of the catalyst materials

The Cu-based materials were fabricated via microwave-assisted solvothermal synthesis. Samples were prepared with different concentrations of Zn precursor and were named as “Cu_xZn_y”, where ‘x-y’ is equivalent to the nominal atomic ratio of copper and zinc precursors. Copper and zinc single-metal samples were also fabricated to highlight the changes in the ZnO/Cu materials. All the different samples are recapped in table 3.1.

The synthesis process is divided in four different steps, summarized in Fig.3.2. In the first step, the chosen quantity of copper and zinc precursors (Tab 3.1) were dissolved in a solution of 5ml of water and 35ml of ethylene glycol (solution 1 in Fig 3.2), facilitated by a hot plate stirrer. The produced solution have a clear light blue colour. Right after that, on another hot plate stirrer, 1280mg of sodium hydroxide were dissolved in a solution containing 24ml of EG and 4ml of H₂O to get about 1.14M of NaOH (solution 2 in Fig 3.2). After the dissolution, 20ml of solution 2 were added dropwise in the first solution, getting a dark blue solution.

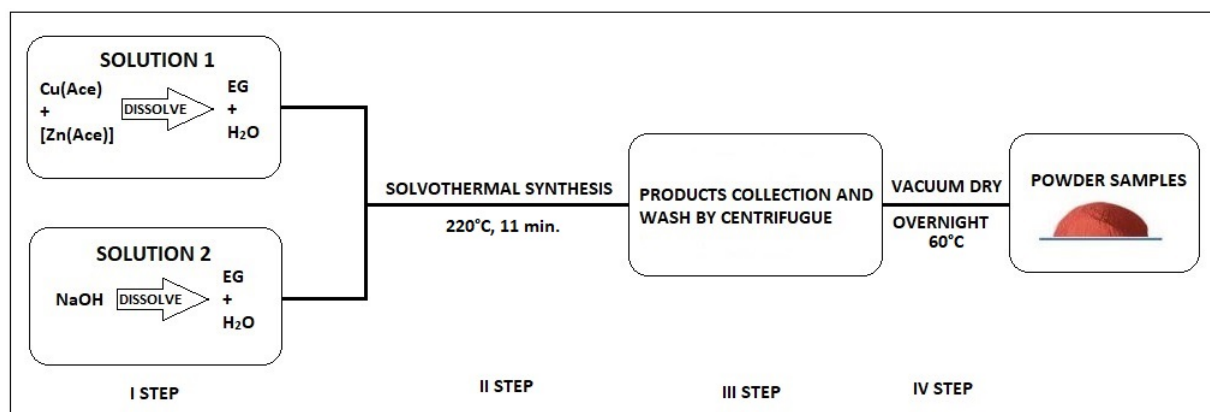


Figure 3.2: Microwave-assisted solvothermal route.

The second step is the solvothermal microwave-assisted synthesis. The Teflon vessel was sealed and connected to the temperature and pressure sensors of the oven. Temperature and irradiation time were set through the control panel of the microwave together with the maximum pressure and power reachable during the synthesis (25bar and 900W respectively). All the samples were synthesised at $T = 220^\circ\text{C}$ for 11 minutes (1 minute to reach the desired temperature and 10 minutes of synthesis). The set values were checked through the control panel of the oven during the synthesis (Fig 3.3). All the samples were cooled in the oven to room temperature.

After the synthesis, the sample was transferred in a plastic vial in order to separate the liquid solution from the precipitate by a centrifuge machine (Fig. 3.4). Subsequently, the liquid was removed and the precipitate was washed twice with water and once with ethanol to remove decomposition products soluble in EG/H₂O and residual EG from the precipitate. All these washing steps were made for ten minutes at 5000rpm.

Table 3.1: Sample prepared with different amount of Cu and Zn precursors.

Samples	Cu(Ace) [mg]	Zn(Ace) [mg]
Cu	900	0
Cu ₉ Zn ₁	900	120.6
Cu ₉ Zn ₃	900	361.8
Cu ₉ Zn ₆	900	723.7
Cu ₉ Zn ₉	900	1085.5
ZnO	0	1085.5

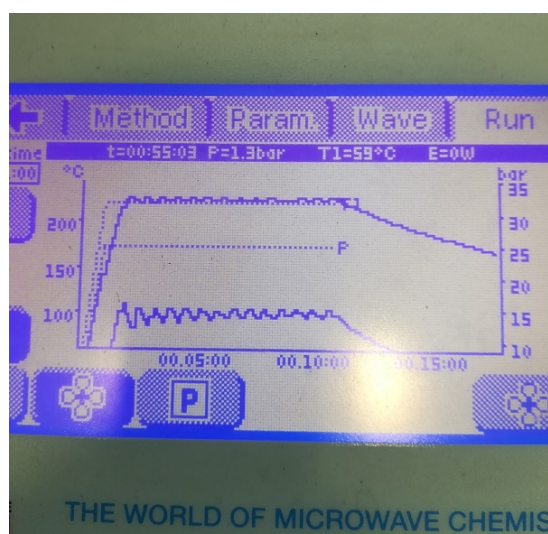


Figure 3.3: The microwave control panel during the synthesis.



Figure 3.4: The centrifuge machine used for collecting and washing step, a UNIVERSAL 320 Hettich, Andreas Hettich GmbH & Co. KG.

Ultimately, the clean powder was placed overnight in a vacuum oven (Fig 3.5) at 60°C, thus obtaining a fine and dry powder.



Figure 3.5: BÜCHI Glass Oven B-585, BÜCHI Labortechnik AG.

3.2 Electrode fabrication

3.2.1 Materials used

The materials used for the preparation of the electrodes are: different synthesised Cu-based powders, acetylene carbon black (CB, Shawinigan Black AB50), Nafion[®] 117 solution (5wt.%), isopropyl alcohol and carbon paper with a gas diffusion layer (GDL) (SIGRACET 28BC, SGL Technologies). The electrolyte is an aqueous solution of 0.1M potassium bicarbonate (KHCO₃, 99.7%).

3.2.2 Electrode preparation

Carbon paper was used as the substrate and it can assure the desired conductive properties of the electrode. The catalyst layer is coated onto the carbon paper. The catalyst layer is composed of a catalyst, CB and Nafion[®]. The CB can enhance the electrical conductivity. The Nafion can increase the ionic conductivity and binder the powder on the substrate. In a typical preparation, 5mg of the chosen catalyst, 0.5mg of carbon black and 45µl of Nafion[®] 117 (for protons exchange and binding properties) were mixed well with 160µl of isopropyl alcohol. The dispersion process was facilitated by sonication for approximately thirty minutes. This ink was then utilized to coat dropwise onto the carbon paper, obtaining an electrode with an active area of $1.5 \times 1\text{cm}^2$. After drying overnight, the electrode was surrounded by copper tape to assure a conductive contact with the current collector during the test (Fig.3.6). The electrode was used for chronoamperometry measurement in a two-compartment three-electrode cell (Sec.3.3.5).

From the abovementioned electrode ($1.5 \times 1\text{cm}^2$), a smaller electrode $0.4 \times 0.5\text{cm}^2$ of active surface was cut out to make the Cyclic Voltammetry measurement in other electrolytic cell type (Fig.3.6). All the electrodes have a mass loading of catalyst material of $3.33\text{mg}/\text{cm}^2$ and all the inactive parts of the electrodes were covered with Teflon tape before the tests.

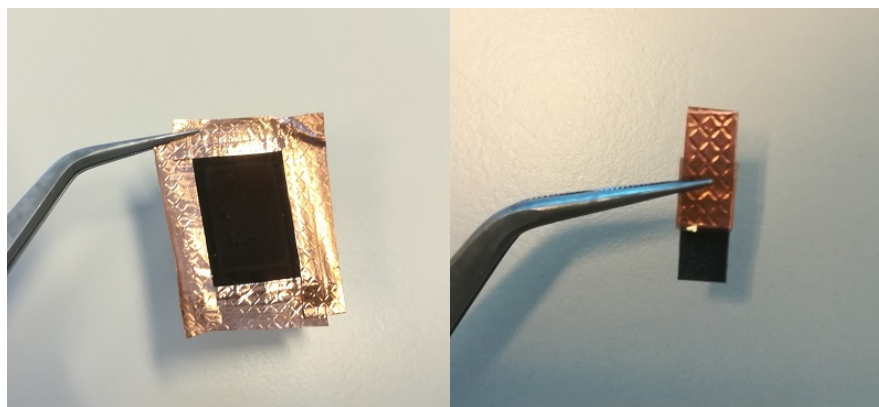


Figure 3.6: The big electrode ($1.5 \times 1\text{cm}^2$) for CA measurement on the left, and the small electrode ($0.4 \times 0.5\text{cm}^2$) for CV measurement on the right.

3.3 Material characterization

As mentioned in Sec.1.3, all the synthesised materials are characterised with several techniques to examine their morphology, composition, electrochemical and catalytic properties. In this section, all the characterization techniques are explained.

3.3.1 Field-Emission Scanning Electron Microscopy

According to Leng [24], the scanning electron microscope (SEM) is the most extensively used type of electron microscope because it is a versatile and non-destructive microscopy technique that reveals information about the morphology and the composition of a specimen. The SEM allows to analyse microscopic structure by scanning the surface of materials with an electron beam at high resolution and great depth of field, resulting in images with a three-dimensional appearance. The specimen's electrons and the electron beam interact in both elastic and inelastic way, giving different types of signals. In elastic interactions, the kinetic energy of the electron is not affected, while inelastic scattering occurs when there is an energy transfer from the electron beam to the atoms in the specimen, resulting in electrons with lower energy and small trajectory deviation. From each of these electron signals, it is possible to get specific information about topography, surface characteristics and composition of the analysed specimen.

A SEM consists of an electron gun (to provide a large and stable current in a restricted beam), a series of electromagnetic lenses and apertures (to focus the beam on the specimen's surface) and a positively charged griddle that attracts the electrons emitted by the specimen to the electron detector (Fig.3.7). In a SEM the electron beam is emitted from a thermionic electron gun; a thermionic emitter uses electrical current to heat up a filament (cathode), generally made of tungsten (W) or lanthanum hexaboride (LaB_6). At elevated heat the work function of the filament material is overcome and the electrons can escape from the material itself, generating an electron beam. Thermionic sources have some operative problems, like the evaporation of cathode material, relative low brightness, thermal drift during operation and specimen's surface charge.

To overcome these complications and to acquire higher resolution images, a Field-Emission Scanning Electron Microscopy (FESEM) can be used. FESEM uses a field emission gun, also called a cold cathode field emitter, that does not heat the filament, but emits electrons by placing the filament in an extremely large electrical potential gradient. The filament is usually a wire of tungsten crafted into a sharp point ($\approx 100\text{nm}$) to lower the work function of the cathode. As

a result, FESEM acquires cleaner images with less electrostatic distortions and with a spatial resolution value as much as six times better than SEM.

Both SEM and FESEM operate under vacuum condition to reduce electrons interference.

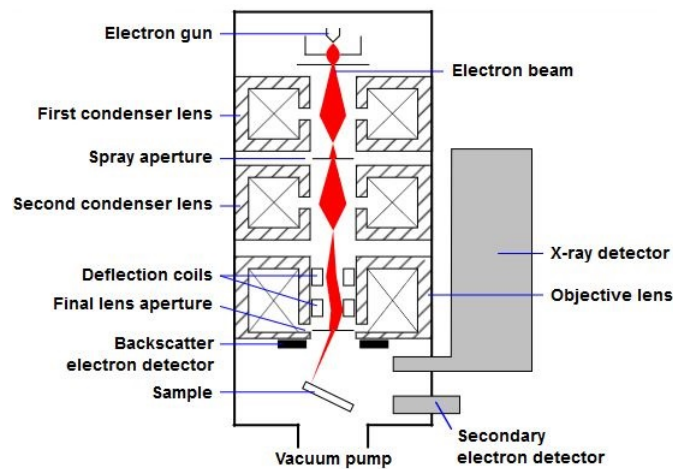


Figure 3.7: A schematic representation of a SEM [©User:Steff, modified by User:ARTE / Wikimedia Commons / CC-BY-SA-3.0].

3.3.2 X-Ray Diffractometry

According to Leng [24], the X-ray diffractometry (XRD) spectroscopic technique is the most widely used diffraction method for materials characterization. X-rays are an electromagnetic radiation of short wavelength ($0.01 < \lambda < 10\text{nm}$) comparable with the size of crystal lattice parameters. X-rays are produced by the collision of high-speed electrons (accelerated by a high-voltage field) with a metal target in a vacuum tube (a device called X-ray tube). The X-ray's wavelength, and therefore its energy, is related to the acceleration voltage of electrons. The X-ray radiation generated by an X-ray tube has a broad range of wavelengths (*Bremsstrahlung*, i.e. "braking radiation") with some intensity maxima at certain wavelengths: the characteristic X-rays (Fig.3.8). X-ray diffraction methods use monochromatic X-rays generated by filtering out unwanted radiations from the spectrum. The three strongest characteristic X-rays are $K\alpha_1$, $K\alpha_2$ and $K\beta$; among these, $K\alpha$ doublet is the most commonly used monochromatic X-ray radiation for XRD.

XRD is based on wave interferences phenomena and, in particular, on Bragg's Law:

$$n\lambda = 2 * d * \sin(\theta) \quad (3.1)$$

where λ is the wavelength of the incident wave, n is an integer, d is the distance between two crystal planes and θ is the incident angle (Fig.3.9).

It is well known that two light waves with the same wavelength that travel in the same direction can interfere either constructively or destructively, depending on their phase difference. According to Eq.3.1, the deflected waves will be in-phase only when the Bragg relationship is satisfied, thus the path difference between them has to be an integer multiple of X-ray wavelengths ($n\lambda$). When constructive interference occurs at a given θ and λ , the information on the spacing between atomic planes of a crystal can be obtained, determining the crystal structure of

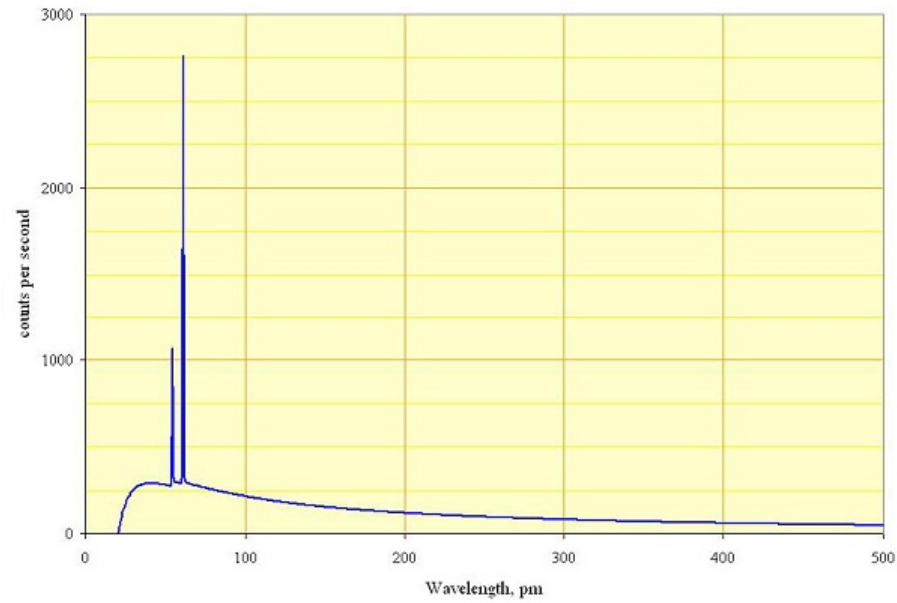


Figure 3.8: X-rays spectrum emitted by a rhodium target at 60 kV [Wikimedia Commons public domain image].

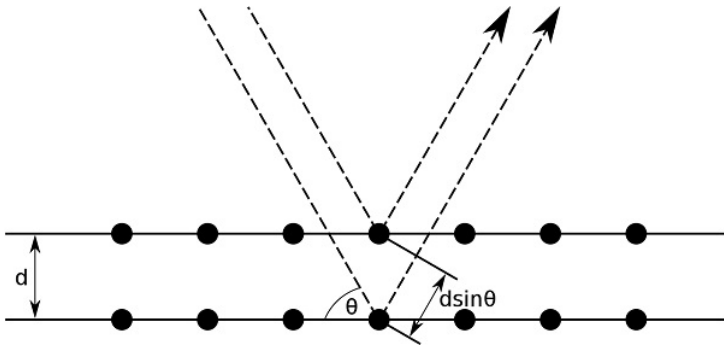


Figure 3.9: Schematic representation of Bragg's Law [Wikimedia Commons public domain image].

the examined material. For example, the plane spacing of a cubic crystal relates to the lattice parameter (a) can be calculated by

$$d_{hkl} = \frac{a}{\sqrt{h^2 + k^2 + l^2}} \quad (3.2)$$

where (h, k, l) represent a series of parallel planes in a crystal with spacing of d_{hkl} . Combining Eqs.3.1 and 3.2, a relationship between diffraction data and crystal parameters for a cubic crystal system can be obtained

$$\sin^2(\theta) = \frac{\lambda^2}{4a^2}(h^2 + k^2 + l^2) \quad (3.3)$$

the relationship between deflection angle and the Miller indices has to be calculated in order to relate ($h^2 + k^2 + l^2$) measured to a plane (hkl) or a set of planes $\{hkl\}$; however, for most crystalline materials, it has already been determined and published by the International Centre for Diffraction Data (ICDD). When the Eq.3.1 is satisfied, a crystallographic plane (hkl) is represented as a light spot of constructive interference. All the different diffraction spots of a crystal form a three-dimensional array called reciprocal lattice. "A reciprocal lattice is in an imaginary reciprocal space that relates to the corresponding crystal lattice in real space" [24].

XRD techniques in materials characterization are used for examining the crystal structure of powder or single crystal samples. In X-Ray powder diffractometry, the machine records a spectrum of diffraction intensity versus the angle between incident and diffraction beam, changing continuously the incident angle of monochromatic X-ray beam. As a result, the machine's software compares the spectrum with its database, thus identifying the crystal structure.

3.3.3 Inductively Coupled Plasma/Optical Emission Spectrometry

According to Meyers [25], inductively Coupled Plasma/Optical Emission Spectrometry (ICP/OES) is a powerful analytical tool for the determination of trace elements in gas, liquid and solid samples. This technique is based upon the spontaneous emission of photons from atoms and ions when excited with a ICP. Liquid and gas samples can be directly injected into the instrument, while analytes of solid samples needs to be extracted or digested in acid in order to get a solution. The sample solution is then nebulized into the plasma chamber. The ICP core reaches temperature of approximately 10000K, vaporizing the aerosol quickly. In the first place, analyte elements turn in their gaseous state. Subsequently, further collisional excitation within the plasma promotes the atoms and ions to their excited states. In order to relax, the excited state species emit a photon of characteristic energies (λ), depending on the quantized energy level structure of the analytes. The measured λ allows to identify the elements present in the solution, while the number of photons is directly proportional to the concentration of these elements.

The ICP/OES is mainly composed of two parts: the ICP and the optical spectrometer. The ICP torch consists of three concentric quartz glass tubes surrounded by a coil of a radio frequency (RF) generator. The gas used to create the plasma is typically Ar and its ionization process is initiate by a brief discharge arc, when a radio frequency signal flows through the coil. The analytical nebulizer directly introduce the aerosol inside the plasma flame, starting the emission of characteristic photons. Transfer lenses are then used to focus the emitted light on a diffraction grating (monochromator) that separates it into its different wavelengths (colours). Subsequently, the particular wavelength is converted to an electrical signal by a photodetector and then amplified and processed by the detector electronics.

The elemental analysis was carried out with an iCAP 7600 DUO (Thermo Fisher Scientific). The RF power of the plasma, the nebulizer gas flow, the coolant gas flow and the auxiliary

gas flow were 1150W, 0.5L/min, 12L/min, 0.5L/min, respectively. Samples were weighted and digested in a flask with 10% of aqua regia overnight, filled up at volume with Milli-Q and filtered using a 0.45 μ m PTFE filter before reading them with the instrument. Ar gas was used as Internal Standard and the R^2 value of the calibration for the Zn and Cu elements (189.99 λ , 324.75 – 224.70 λ , radial mode respectively) was 0.999.

3.3.4 Cyclic Voltammetry

According to Elgrishi et al. [26] and Allen J. Bard [27], Cyclic Voltammetry (CV) is a useful technique employed to examine the oxidation and reduction processes of molecular species and to investigate electron transfer-initiated chemical reactions. From a CV experiment, it is able to obtain a cyclic voltammogram (Fig.3.10) in which the x-axis represents the imposed potential, while the y-axis is the resulting current passed. CV data are commonly reported with two different conventions. In this work, the IUPAC convention is used, where potentials become more positive along the x-axis and oxidation currents are defined as positive. The key parameters of the measure are the potential scan range and the scan rate, the rate of voltage change over time during each applied potential variation.

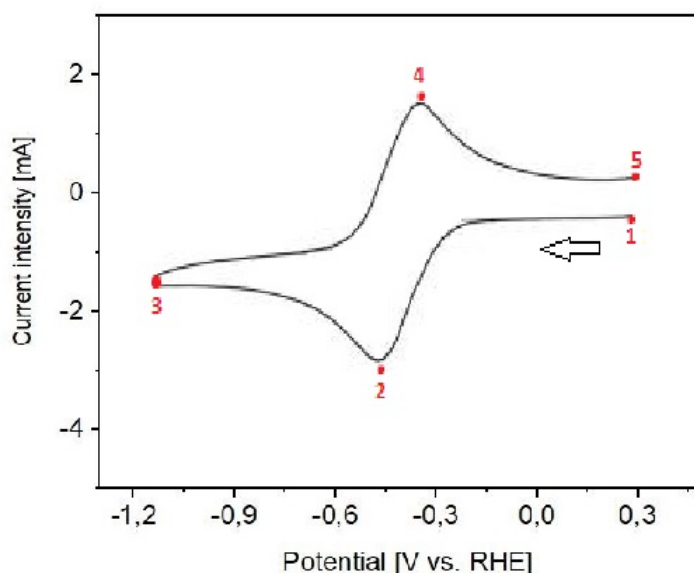


Figure 3.10: A typical CV plot; the arrow defines the convention used.

The whole CV measure is based on the equilibrium between analytes A and A^+ , described by Nernst Equation

$$E = E^0 + \frac{RT}{nF} \ln \frac{(Ox)}{(Red)} \quad (3.4)$$

where E is the potential at the electrode, E^0 is the standard potential of the species, (Ox) and (Red) are the relative activities of the oxidized and reduced analytes in the system at equilibrium, F is Faraday's constant, R is the universal gas constant, n is the number of electrons and T is the temperature. This equation can be simplified for one-electron reduction reaction ($n = 1$) replacing E^0 with the formal potential $E^{0'}$ and the activities with the concentration of analytes

$$E = E^{0'} + \frac{RT}{F} \ln \frac{[A^+]}{[A]} \quad (3.5)$$

During the cathodic scan (points 1 – 3 of Fig.3.10), A^+ is reduced to A locally at the electrode, exhausting all the A^+ at the electrode surface. The current peak at point 2 (Fig.3.10) is generated because the reduced A grows continuously (diffusion layer) and the mass transport of A^+ is limited at the surface of the electrode during the scan (satisfying Eq.3.4), thus decreasing the reaction rate and, therefore, the recorded current. When point 3 is reached, the potential is switched and the scan direction is reversed (anodic scan, points 3 – 5), oxidizing all the A present at the electrode surface back to A^+ as the potential grows positively. The separation between the two peaks is due to the diffusion of the analytes to and from the electrode, as well as the polarization. In Fig.3.10, the reduction process is electrochemically reversible. In fact there is a low barrier to electron transfer and the equilibrium of Eq.3.4 is established immediately after any change in applied potential. In case of irreversible reactions or more complex multiple electron-proton transfer reactions (like CO_2RR), there is a larger barrier to electron transfer and more negative (positive) potentials are required to achieve reduction (oxidation) reactions. The process is generally slower and the peaks are more spaced. For this kind of reactions, CV provides useful kinetic and mechanistic information that allows to better understand the electron transfer reactions underlying the CO_2RR .

CV measurements were performed with Multi Autolab potentiostat/galvanostat at room temperature in 10ml of electrolytic solution ($KHCO_3$ 0.1M) saturated with CO_2 or N_2 . A platinum wire was used as counter electrode due to its conductivity and inert behaviour. A $Ag/AgCl$ ($3M Cl^-$) electrode was used as reference. Each measure was revised by an 85% compensation of the ohmic potential drop (iR-compensation).

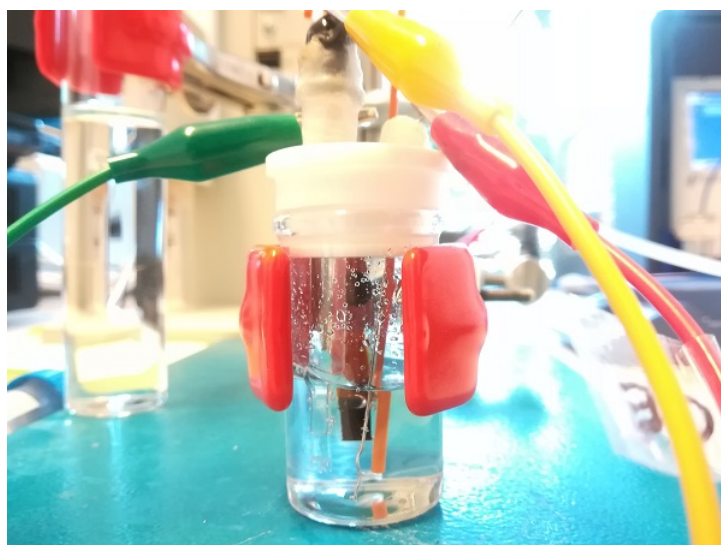


Figure 3.11: Electrolytic cell for CV measurement.

3.3.5 Chronoamperometry

According to Allen J. Bard [27], chronoamperometry (CA) is a commonly used technique in electrochemistry because of its relative ease of implementation and analysis. In an unstirred cell, all the electrochemically active species will diffuse to the electrode's surface as a function of the potential applied to it. Like CV measurements, the analyte concentration decays with distance from the electrode and the arrival of new analyte is diffusion limited. Because of that, when the mass transport limit is reached, the Faradaic current near the electrode also decays and the current is described by Cottrell equation. For a general reaction $O + e \rightleftharpoons R$, Cottrell

equation can be written as

$$i(t) = \frac{nFA\sqrt{D_O}C_O^*}{\sqrt{\pi t}} \quad (3.6)$$

where $i(t)$ is current, t is time, n is the number of electrons transferred in the half reaction, F is Faraday's constant, A is the area of the electrode, D_O is the diffusion coefficient of the O species and C_O^* its initial concentration.

In general, the potential applied to the electrode should be more negative than the formal potential ($E^{0'}$) of the reaction so that the reduction $O \rightarrow R$ can be completed at the electrode's surface, following Eq.3.6.

CA measurements were performed with CH 700E Series Bipotentiostat at room temperature in a two-compartment three-electrode cell (Figs.3.12-3.14). An ion exchange membrane (Nafion, 117) is used to separate the two compartments. Each compartment was filled with 7ml of 0.1M KHCO_3 , leaving 3ml of head space. A Pt foil was used as counter electrode, along with a Ag/AgCl reference electrode (1mm, leak-free LF-1). The electrolyte solution was static for both the anode and cathode chambers. A constant CO_2 flow rate of 15ml/min is maintained in the cathodic chamber to saturate the electrolyte and to carry out gas products to the online micro-gas chromatography, while a flow rate of 3ml/min for the anodic chamber. All the samples were analysed at various potentials and the measures were corrected with an 85% compensation of the ohmic potential drop (iR-compensation).

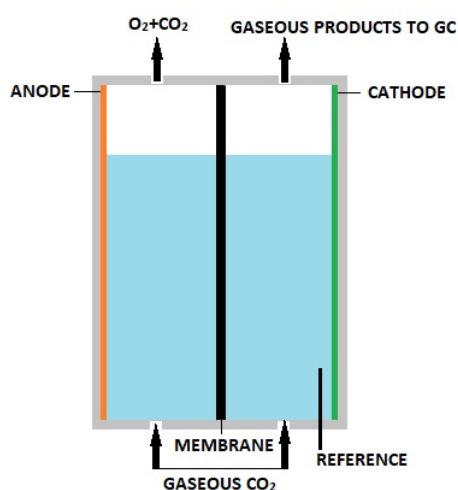


Figure 3.12: Schematic representation of the EC for CA measure.

3.3.6 Gas chromatography

Gas chromatography (GC) is a common technique used in analytical chemistry for separating gaseous compounds and thus analyse them. According to Regmi and Agah [28], GC exploits the physics effect of differential migration of the components of a gaseous mixture caused by their crossing through an immobilized column with a stationary phase. A typical GC configuration is shown in Fig.3.15.

At the exit of the column a detector identifies the amount of separated components as a function of time. The difference between the injection time of the sample in the column and the detection time of a single component (a peak maximum in the chromatogram) is called total

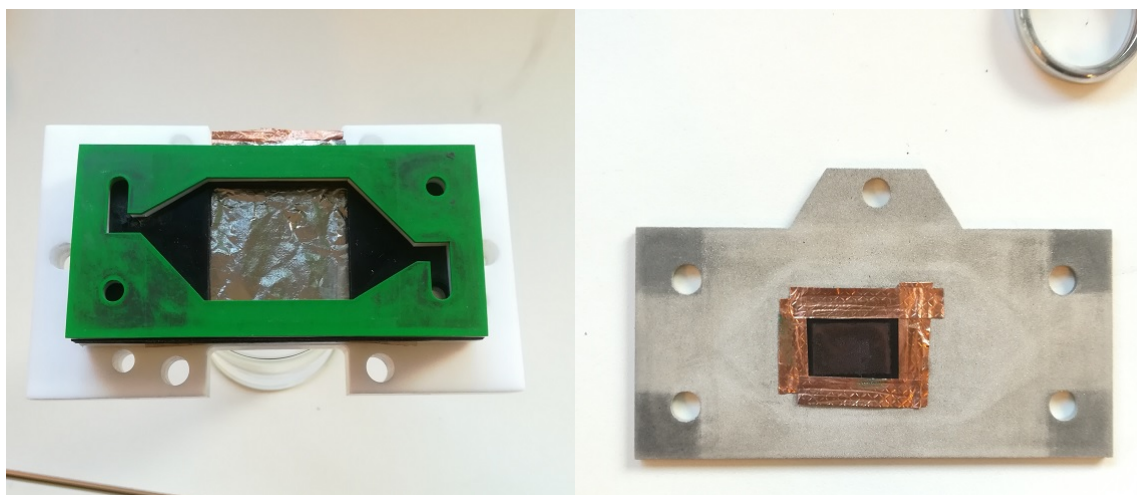


Figure 3.13: Pt foil (anode, left) and working electrode (cathode, right). All the inactive parts of the cathode were then covered with Teflon tape.



Figure 3.14: Completely assembled EC for CA.

retention time (t_R) of that component. Furthermore, the difference between t_R and the hold-up time (the time spent by the component in the mobile phase t_M , same for all components) is called adjusted retention time (t'_R) and corresponds to the actual time spent by the component in the stationary phase.

$$t'_R = t_R - t_M \quad (3.7)$$

To increase and optimise chromatographic separation the retention factor (k) parameter can be used, defined as

$$k = \frac{t'_R}{t_M} \quad (3.8)$$

and it depends on the interaction strength between a component and the stationary phase. A high k value corresponds high retention time. The k value depends also on the temperature of the column. In particular, k decreases at high temperatures.

Another important parameter is the average linear velocity (\bar{u}) of the mobile phase. Because of the non uniform pressure in the column, there is a velocity gradient of the mobile phase through it;

$$\bar{u} = \frac{L}{t_M} \quad (3.9)$$

where L is the column length and t_M is the retention time of a unretained component (CH_4 is commonly used as unretained marker compound). Average linear velocity influences the separation efficiency of a column and, as a result, the resolution of a chromatographic separation.

All the different processes occurring in the column and, additionally, other effects like injection pulse width and dead volumes, contribute to the separation and dispersion of the compounds, allowing to plot the chromatogram of the injected sample.

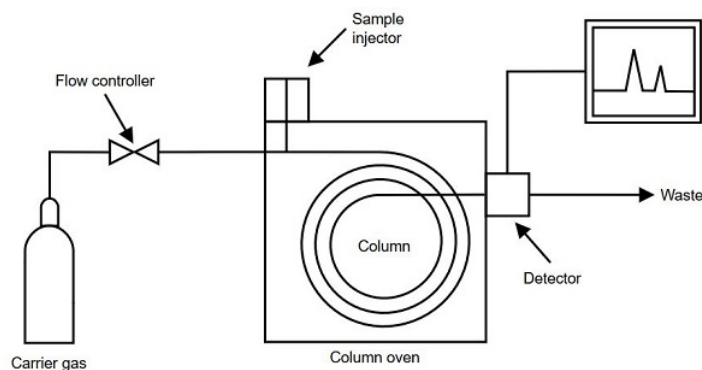


Figure 3.15: Typical GC configuration. The carrier gas is used to control the flow of the injected sample [Wikimedia Commons public domain image].

In this work was used an INFICON micro-GC Fusion (μGC , Fusion[®], INFICON) equipped with two channels with a 10m Rt-Molsieve 5A column and an 8m Rt-Q-Bond column, respectively, and micro thermal conductivity detectors (micro-TCD). All the working principles of a μGC are the same of a GC, but the different components are miniaturized in order to increase the portability of the instrument, to speed up the analysis and to decrease the power consumption. The μGC was connected on-line with the EC during the CA measurement in order to analyse gaseous products generated by the CO_2RR and HER.

4 Results and discussion

In this chapter, all the material characterization results will be presented and discussed for each synthesised material. Naming of the samples follows the nomenclature introduced in table 3.1. In the first section, the morphology and the composition of all the synthesised materials will be analysed separately. In section 4.2, the results of the electrochemical measures will be discussed for each fabricated electrode at various potentials. Ultimately, the results of the material's characterizations will be compared in order to relate the improved efficiency of the fabricated electrodes with the chemical-physical properties of the materials.

4.1 Material's characterization

4.1.1 FESEM

4.1.1.1 Cu

Fig.4.1 shows the Cu powder with a wide size distribution. Most of the agglomerates are sub-micron. The Cu particles have a cube-like shape with irregular surface features (Fig.4.2).

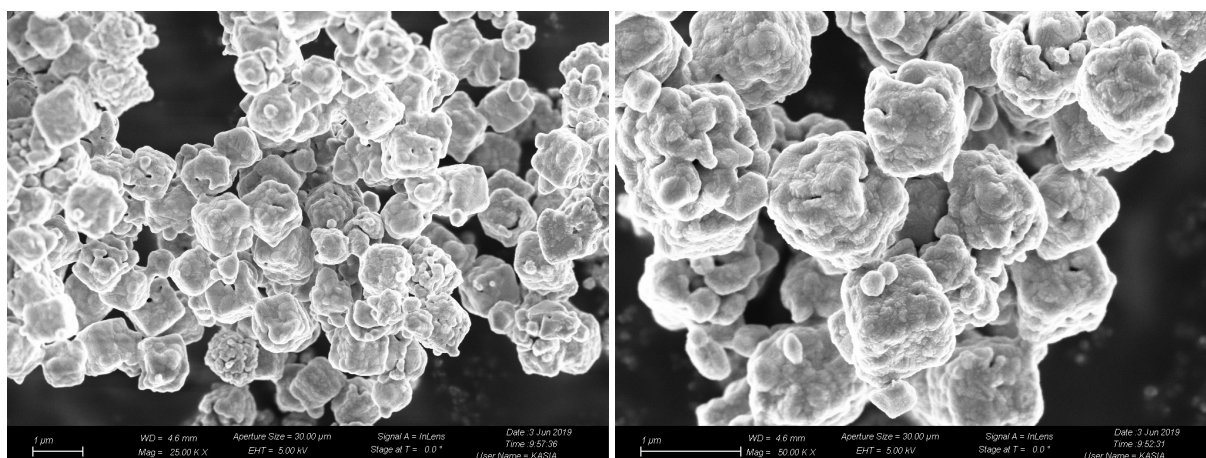


Figure 4.1: FESEM images 2500000 X (left) and 5000000 X (right) of the Cu sample.

4.1.1.2 ZnO

The ZnO sample also exhibits a wide size distribution in the nanometric scale (Fig.4.3). In Fig.4.4, the size of the particles is between 10nm and 30nm. Other bigger particles with irregular shape are also observed ($> 100\text{nm}$).

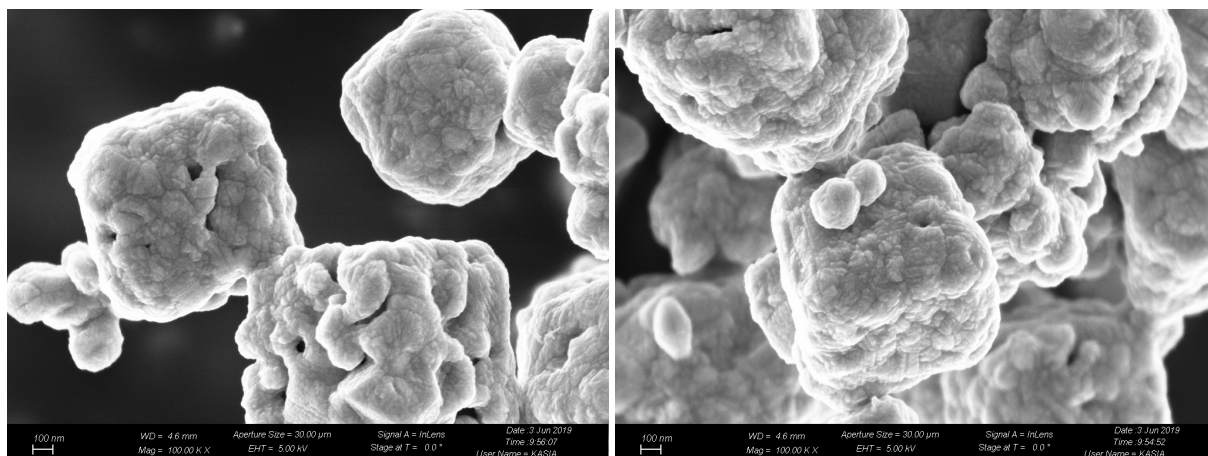


Figure 4.2: FESEM images 10000000 X of the Cu sample.

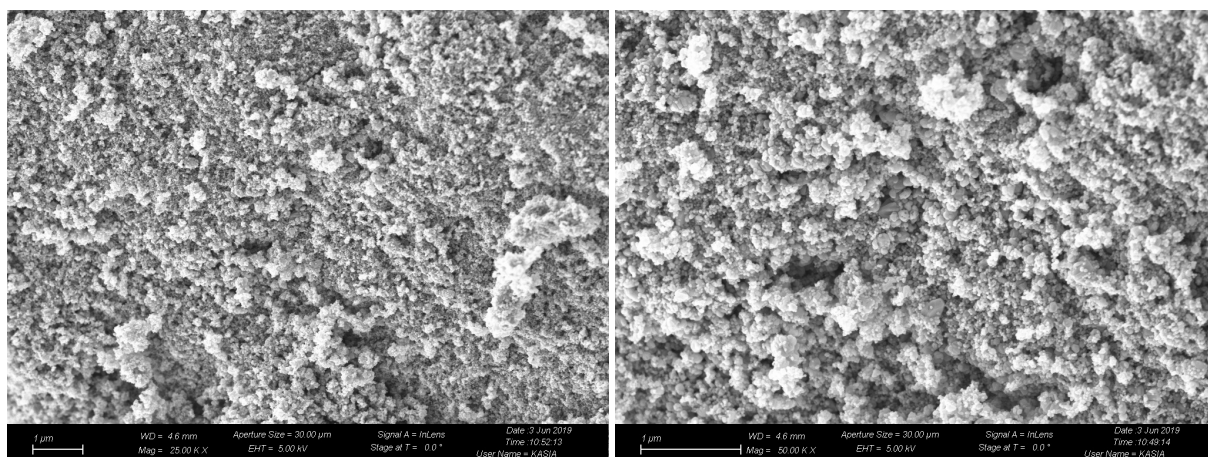


Figure 4.3: FESEM images 2500000 X (left) and 5000000 X (right) of the ZnO sample.

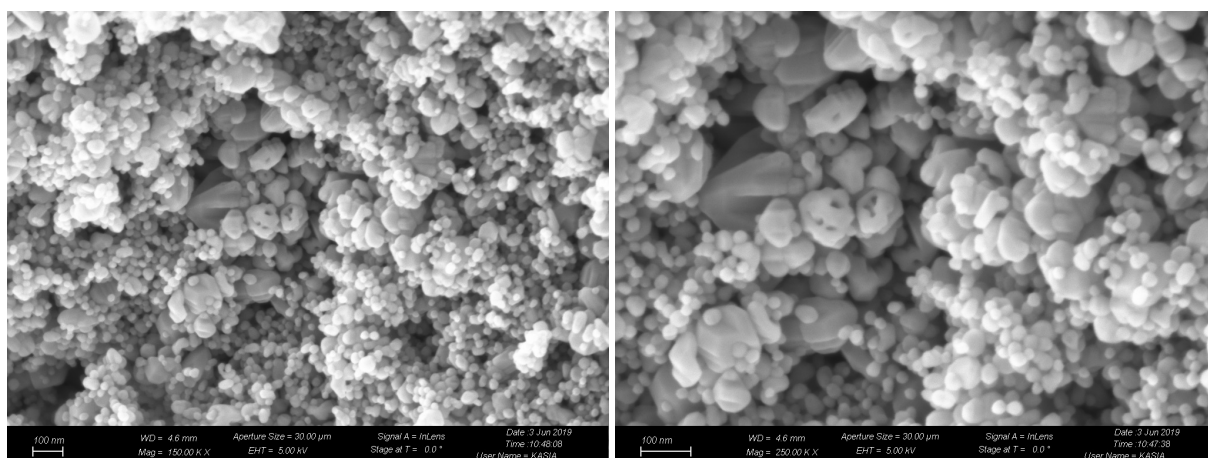


Figure 4.4: FESEM images 15000000 X (left) and 25000000 X (right) of the ZnO sample.

4.1.1.3 Cu_9Zn_1

From Figs.4.5 and 4.6, two different particle types can be distinguished. ZnO particles are smaller and with a nanometric size distribution ($\leq 100\text{nm}$); Cu particles are larger and still with a cube-like shape smaller than $1\mu\text{m}$.

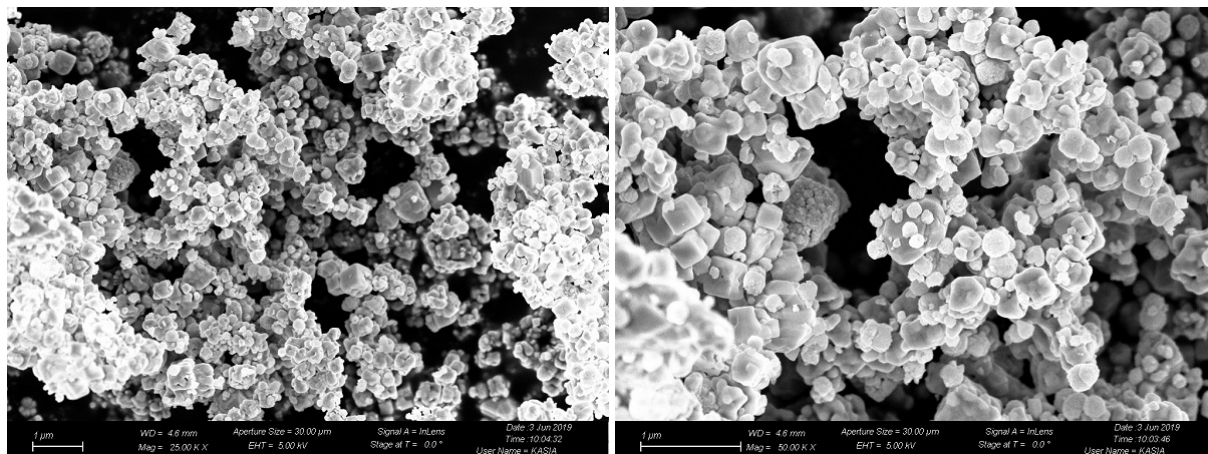


Figure 4.5: FESEM images 2500000 X (left) and 5000000 X (right) of the Cu_9Zn_1 sample.

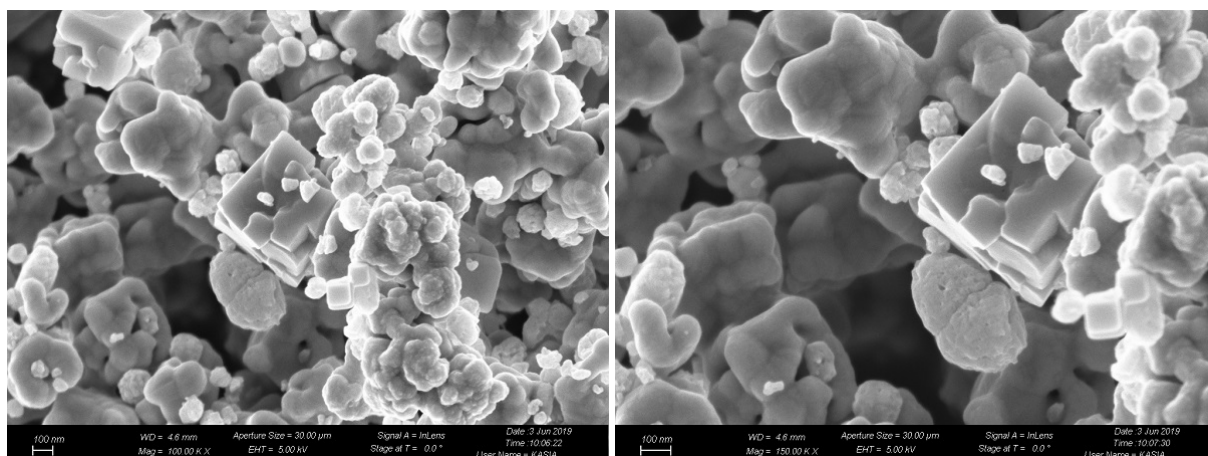


Figure 4.6: FESEM images 10000000 X (left) and 15000000 X (right) of the Cu_9Zn_1 sample.

4.1.1.4 Cu_9Zn_3

Fig.4.7 show the influence of adding more ZnO on the shape of Cu particles. In this sample, nanometric ZnO particles grow on top of irregular and much bigger (in the order of μ) Cu particles, that have lost their cube-like shape (Fig.4.8).

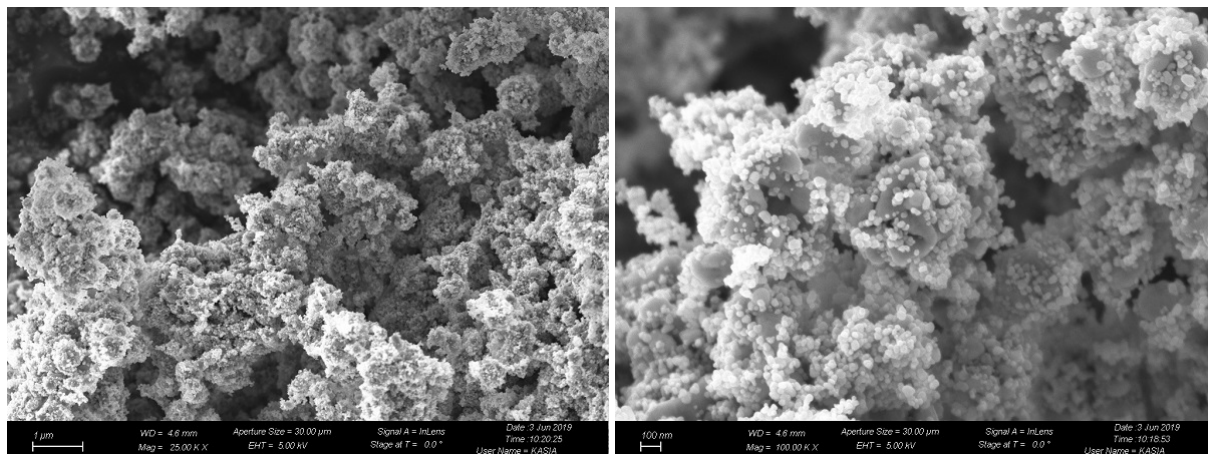


Figure 4.7: FESEM images 2500000 X (left) and 10000000 X (right) of the Cu_9Zn_3 sample.

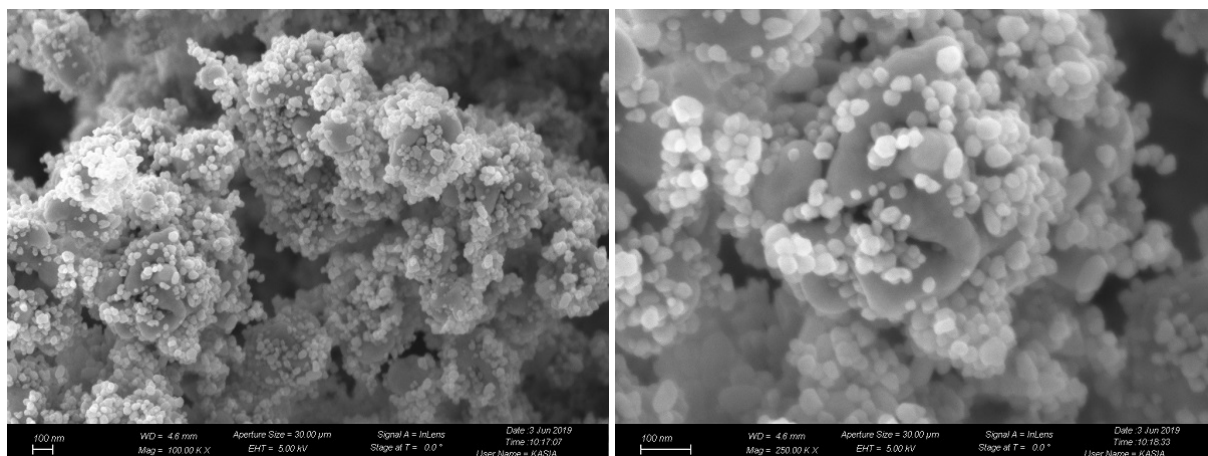


Figure 4.8: FESEM images 10000000 X (left) and 25000000 X (right) of the Cu_9Zn_3 sample.

4.1.1.5 Cu_9Zn_6

Increasing the ZnO atomic ratio enhances the trend already noticed for the Cu_9Zn_3 sample. From Figs.4.9 and 4.10, irregular Cu particles can be barely seen under nanometric Zn particles.

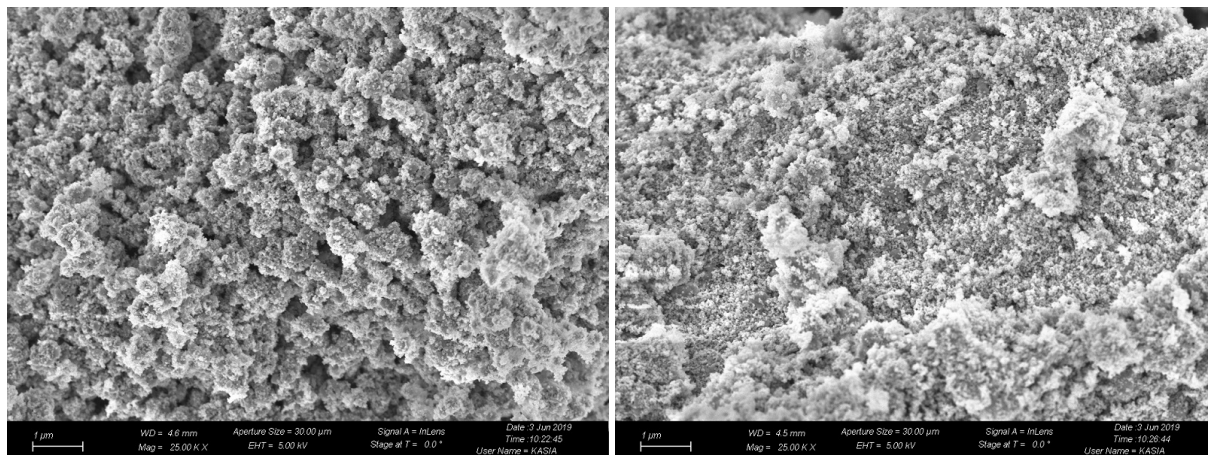


Figure 4.9: FESEM images 2500000 X of the Cu_9Zn_6 sample.

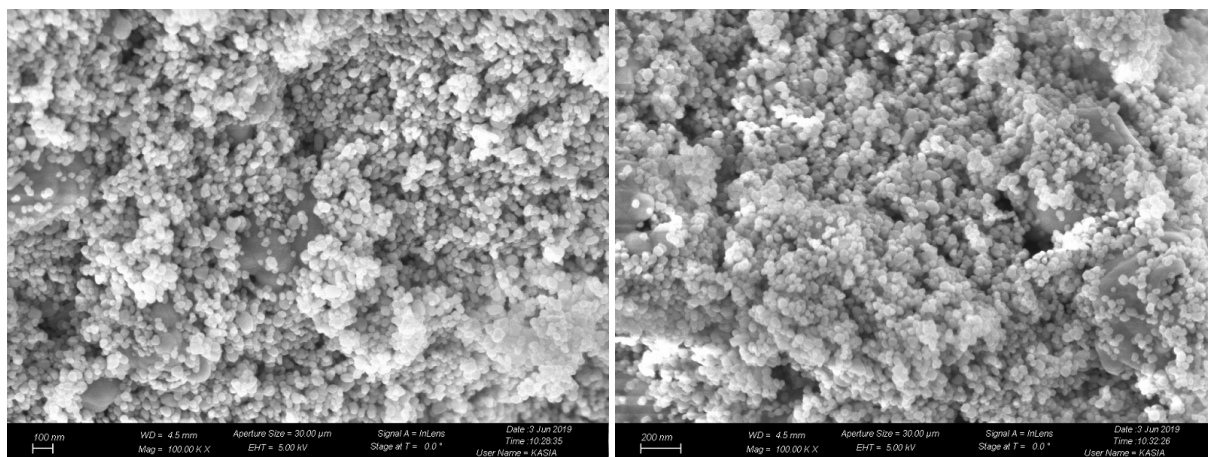


Figure 4.10: FESEM images 10000000 X of the Cu_9Zn_6 sample.

4.1.1.6 Cu_9Zn_9

Like the previous samples, irregular ZnO particles grow on top of Cu particles which are hardly distinguishable (Figs.4.11 and 4.12).

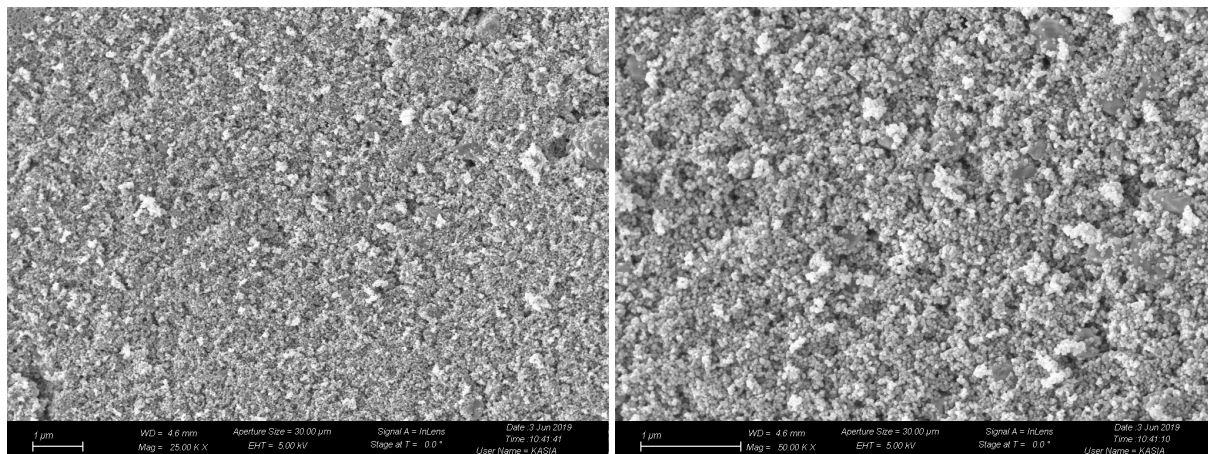


Figure 4.11: FESEM images 2500000 X (left) and 5000000 X (right) of the Cu_0Zn_9 sample.

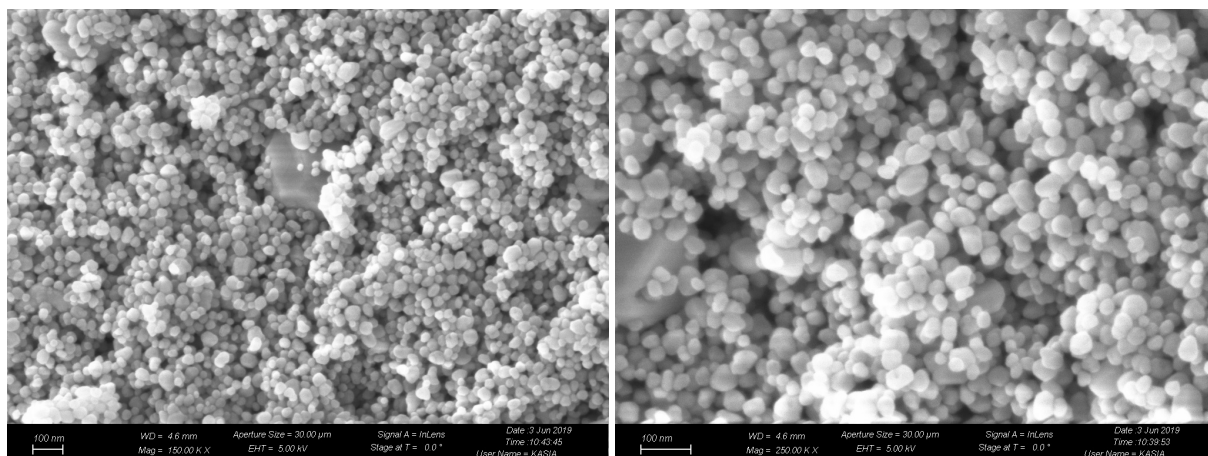


Figure 4.12: FESEM images 15000000 X (left) and 25000000 X (right) of the Cu_0Zn_9 sample.

4.1.2 XRD

In Fig.4.13, the XRD patterns of all the samples are plotted and compared. The reflection planes of Cu and ZnO samples are highlighted in Fig.4.14; these planes correspond to metallic Cu and ZnO, respectively. The synthesis method reduces all the Cu^{2+} of the cupric acetate to metallic Cu, while Zn remains in the Zn^{2+} state thus becoming ZnO. Cu_xZn_y samples show similar XRD patterns (Fig.4.15). They have both the peaks of metallic Cu and ZnO phases, and differ among them only in peaks intensity because of their different atomic ratio. The ZnO-modified samples also have two characteristic peaks of Cu_2O species (Fig.4.15 left). However, the weak intensity of this peaks (hence a negligible Cu_2O quantity) suggests that cuprous oxide forms after the synthesis due to the tendency of small Cu particles to oxidize in air.

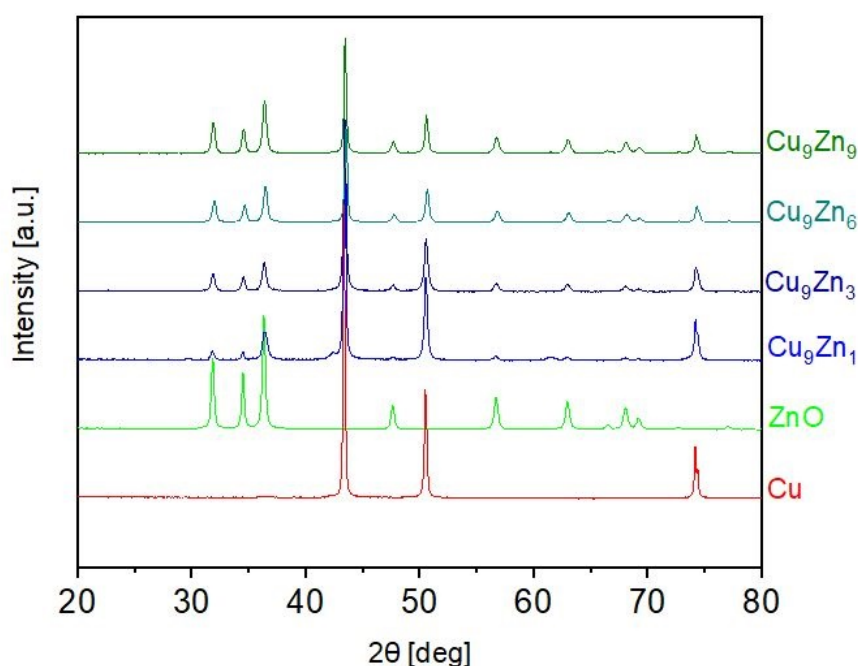


Figure 4.13: XRD results of all the samples.

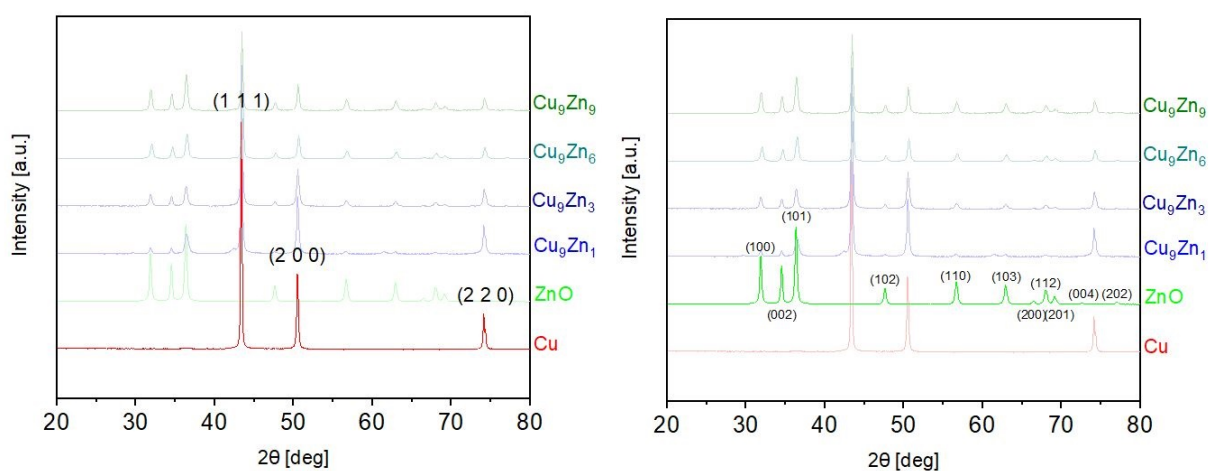


Figure 4.14: XRD plots of Cu sample (left) and Zn sample (right).

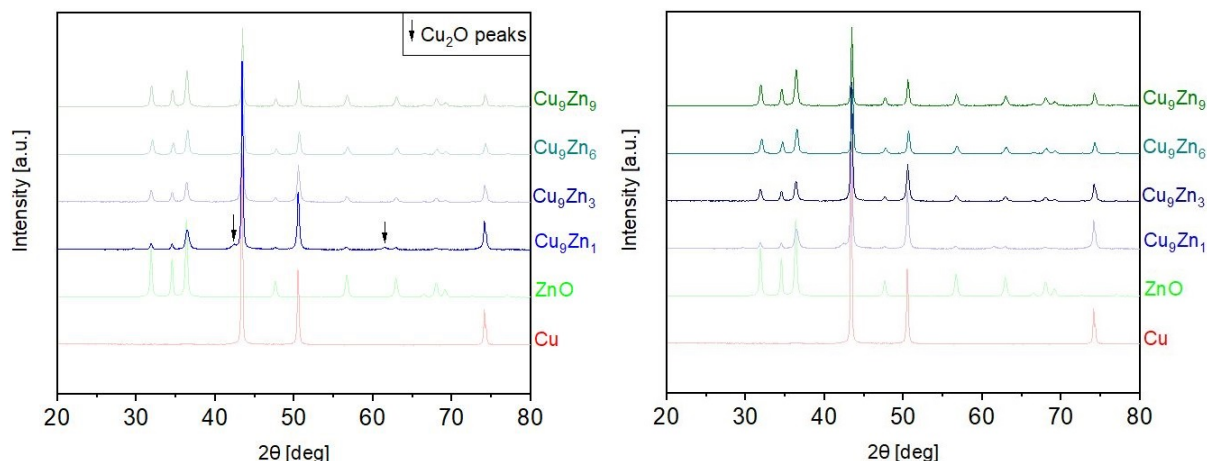


Figure 4.15: XRD results of Cu_9Zn_1 sample (left) and Cu_9Zn_3 , Cu_9Zn_6 and Cu_9Zn_9 samples (right).

4.1.3 ICP/OES

The experimental results of the ICP/OES are reported in table 4.1. ICP/OES confirms XRD data on the species of the samples and validate the feasibility of microwave assisted synthesis. In fact, the Cu/Zn atomic ratio designed for each sample was maintained after the synthesis.

Table 4.1: Results of the ICP/OES

Sample	Cu [wt. %]	Zn [wt. %]	Cu/Zn (atomic ratio)	ZnO [wt. %]
Cu_9Zn_1	92.81	11.70	8.1	14.60
Cu_9Zn_3	75.84	22.70	3.4	28.30
Cu_9Zn_6	52.17	37.26	1.4	46.40
Cu_9Zn_9	44.65	41.06	1.1	51.20

4.2 Electrochemical characterization

4.2.1 Cyclic Voltammetry

Most of the prepared electrodes were analysed via CV in a potential scan range from +0.4V to -1.2V at a scan rate of 10mV/s. Current density values have been calculated dividing the current intensity value by the geometric surface area of the electrode.

Figure 4.16a shows the cyclic voltammograms (CVs) in both CO_2 - and N_2 -saturated electrolytes at the Cu electrode. In the curves there are no peaks related to the redox reactions of Cu. In the negative potential range, Cu electrode in the CO_2 -saturated electrolyte has a lower current density than that in the N_2 -saturated one at the same potential (8.4mA/cm² and 31.4mA/cm² at -1.1V respectively). Moreover, the onset potential for reduction reactions shifts negatively in the CO_2 -saturated electrolyte. These observations are in agreement with the reported results on Cu materials for the CO_2RR [5, 29]. From the CVs on the ZnO electrode (Fig.4.16b), Zn starts to be oxidized at -0.5V and continues to be oxidized at more positive potentials in the anodic

scan, while the ZnO is reduced or partially reduced at more negative potentials ($< -0.5\text{V}$) in the cathodic scan. According to the reported work conducted by in situ/operando X-ray absorption spectroscopy techniques, the nanostructured and bulk metallic Zn catalysts are demonstrated to be structurally stable at potentials more negative than -0.7V versus RHE, whereas chemical oxidation occurs at more positive potentials [30].

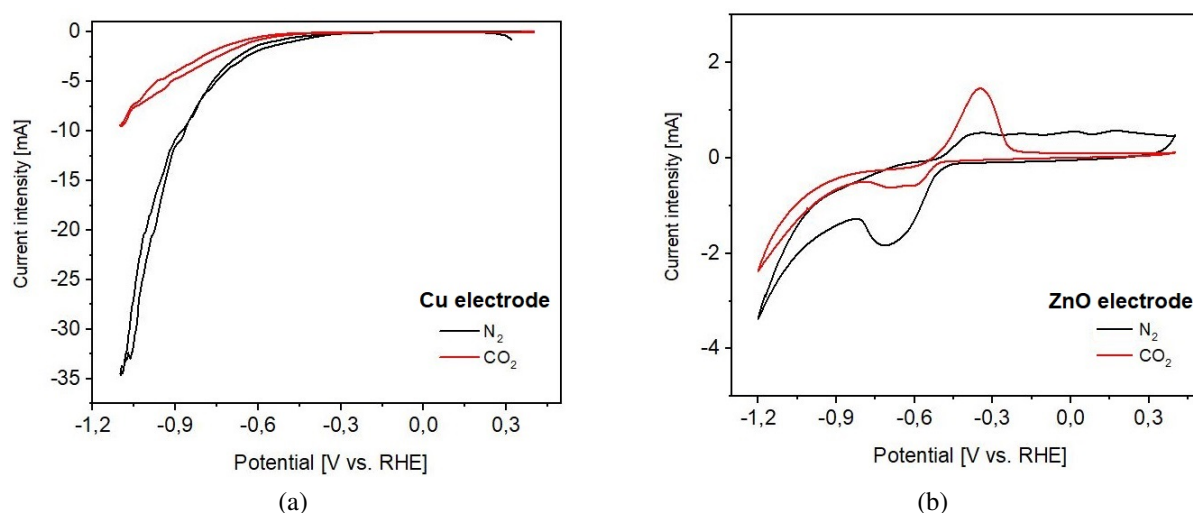


Figure 4.16: CVs of the Cu (a) and ZnO (b) electrodes.

Figures 4.17a, 4.17b and 4.17c display the CVs in both CO_2 - and N_2 -saturated electrolytes on the ZnO-modified Cu electrodes. The redox reactions of Zn are also present in the ZnO-modified Cu electrodes. Similar with the Cu electrode, the ZnO/Cu electrodes in the CO_2 -saturated electrolyte have a lower current density than that in the N_2 -saturated one at the same potential. Interestingly, the difference between the current densities in the two electrolytes is various for the electrodes, indicating the different selectivity for the CO_2RR on these electrodes.

Comparing the CVs in N_2 -saturated electrolyte on all the electrodes (Fig.4.18a), it is found that the addition of ZnO can decrease the current density at negative potentials ($< -0.6\text{V}$). Since only HER occurs in N_2 -saturated electrolyte, this outcome indicates that the addition of ZnO can inhabit the HER.

In CO_2 -saturated electrolyte (Fig.4.18b), the ZnO/Cu electrodes show a broad peak from -0.8V to -1.1V . It is predicted that these electrode could have notable selectivity for the CO_2RR in this potential range. For this reason, the products of all the electrodes have been analysed in this potential range, in particular at four different potentials: -0.8 , -0.9 , -1.0 , -1.1V (V vs. RHE).

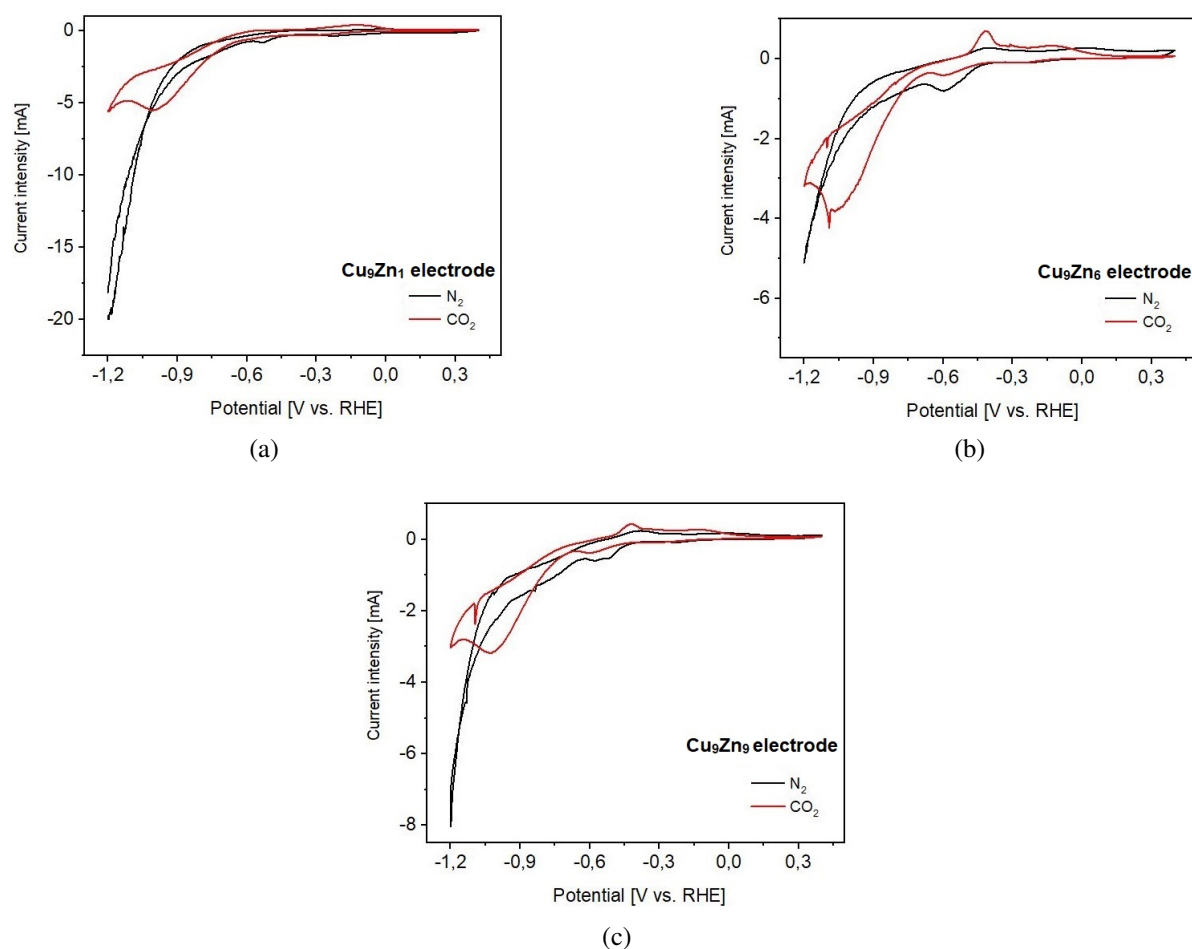


Figure 4.17: CVs of the Cu₉Zn₁ (a), Cu₉Zn₆ (b) and Cu₉Zn₉ (c) electrodes.

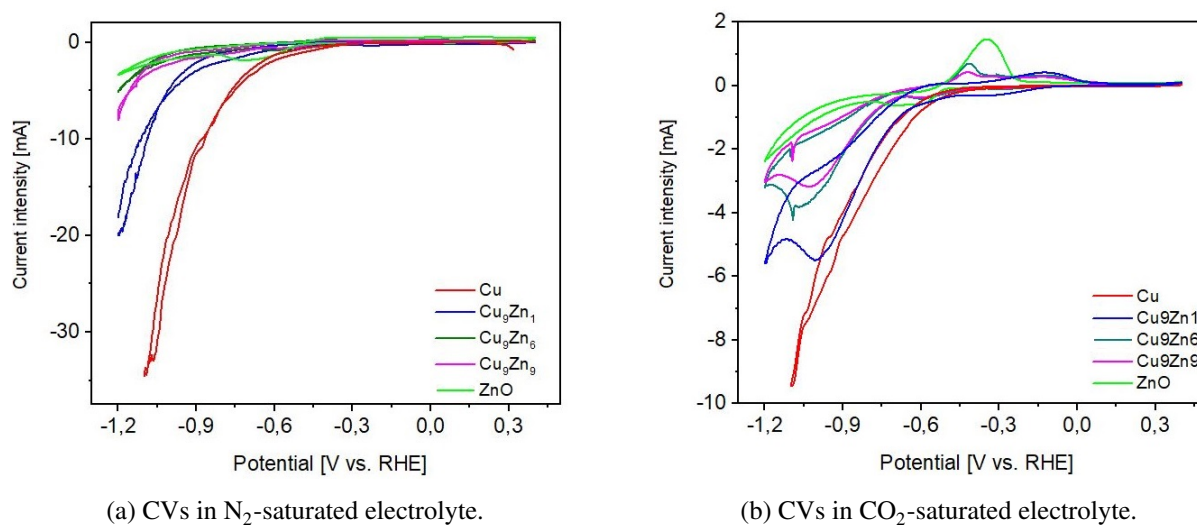


Figure 4.18: Comparison of the CVs of the electrodes.

4.2.2 Chronoamperometry and micro-GC

Since CA measures were carried out on-line with μ GC, results are presented, for each electrode separately, in the same section. In the next section all the results were compared to better understand the electrode's behaviour.

As introduced previously, the electrodes are tested at four different potentials to evaluate their electric properties and reduction products. Furthermore, the measured data are processed in order to better compare the results between different electrodes. In particular, the measured current intensity was divided by the electrode's surface area to obtain current density (j) values, while the FE values were calculated with the equation

$$FE(\%) = \frac{10^{-6} * C_x \dot{V}_x n F}{V_m * i(t)} * 100 \quad (4.1)$$

where C_x is the measured concentration of the formed species in ppm, \dot{V}_x is the flux of the gas through the cell (0.25ml/s), n is the number of electrons involved in the reduction reaction (2 for both CO and H₂), F is the Faraday constant, V_m is the molar volume (22.4ml/mmol) and $i(t)$ is the measured current intensity in mA. FE values of other products, such as HCOOH, are not reported, because these values are low and the total FE value of CO and H₂ is almost 100%, especially on the ZnO/Cu electrodes.

4.2.2.1 Cu

Figure 4.19 shows the CA plots at applied potentials. The current stabilizes in less than 250s, it is stable over time (except at $-1.0V$) and varies from ca. -5.5 to ca. -12.75mA/cm^2 depending on the applied potential. Besides the applied potential, FE values (Figs.4.20 and 4.21) illustrate a considerable production of H₂ ($\approx 80\%$), while CO production remains below 10%.

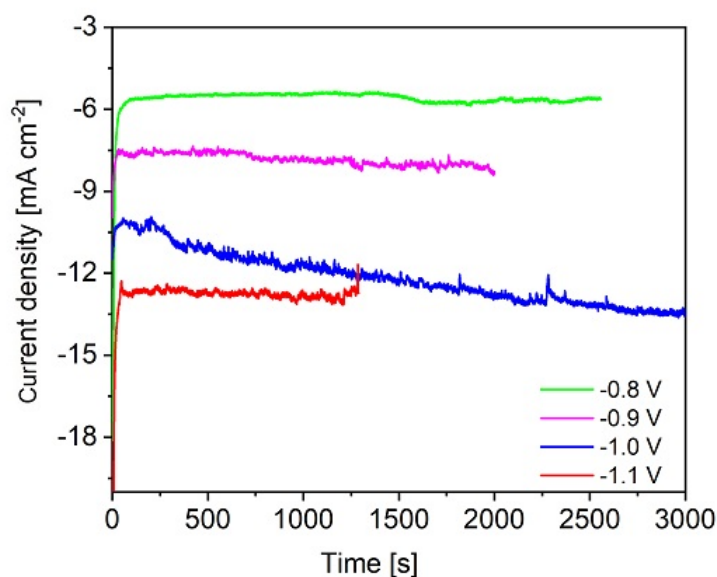


Figure 4.19: CA plots of Cu electrodes.

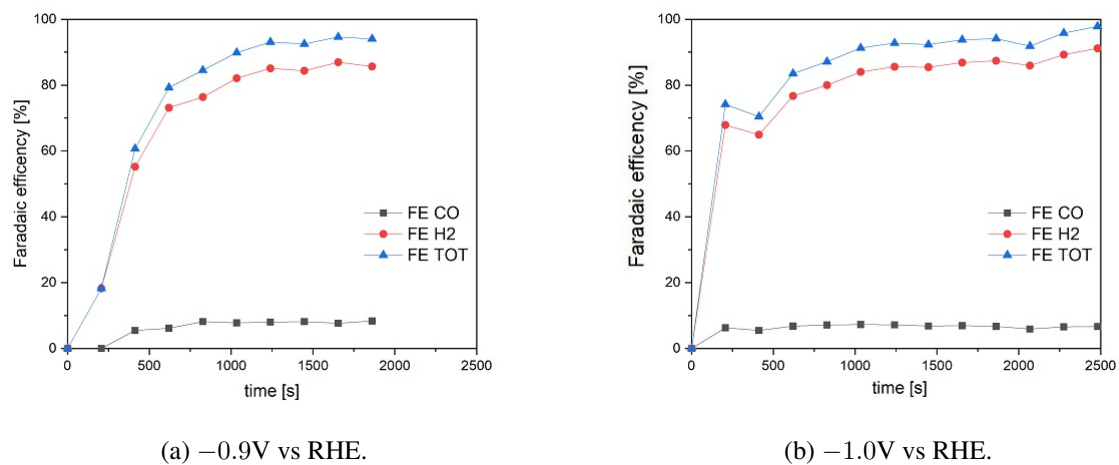


Figure 4.20: FE values over time at two different potentials of the Cu electrodes.

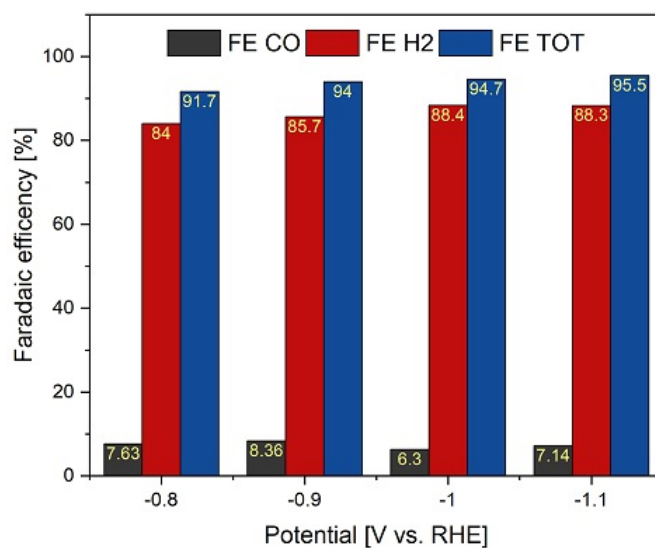


Figure 4.21: Selectivity of Cu electrodes at various potentials.

4.2.2.2 ZnO

The ZnO electrode (Fig.4.22) exhibits a good current stability through time at every potential, but shows a lower current density compared to Cu electrode. Figures 4.23 and 4.24 show the selectivity of the ZnO based electrode; the best performance are achieved at -1.0 and -1.1 V vs. RHE with more than double production of CO (ca. 75%) relative to H_2 production. At all the tested potentials the FE total value is $\approx 100\%$, indicating that ZnO is selective primarily towards CO production.

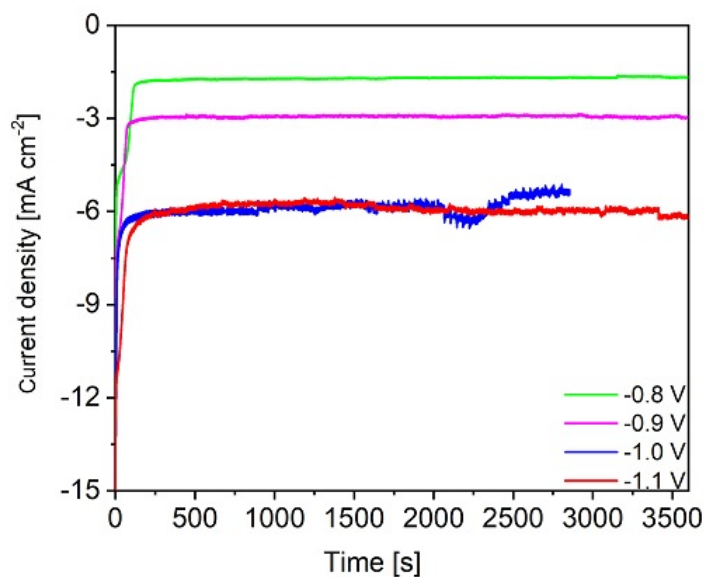


Figure 4.22: CA plots of ZnO electrodes.

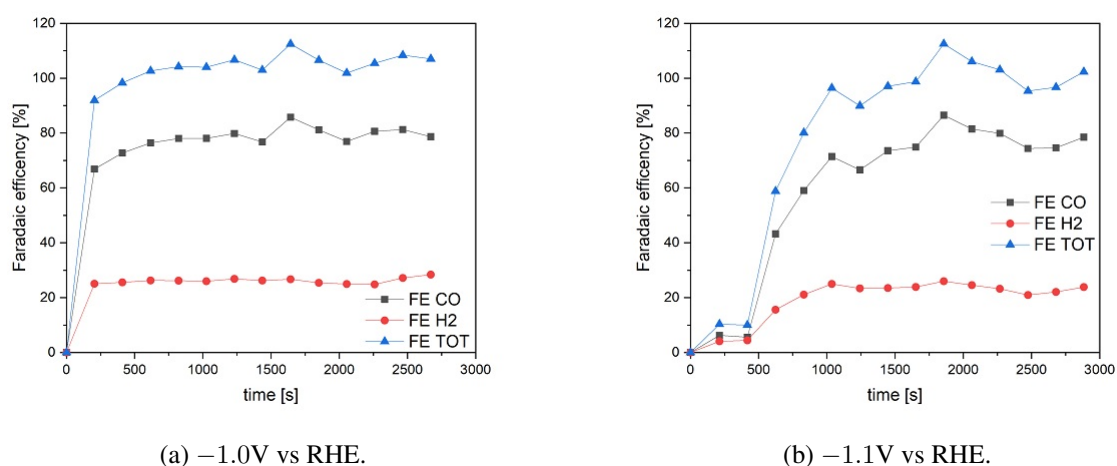


Figure 4.23: FE values over time at two different potentials of the ZnO electrodes.

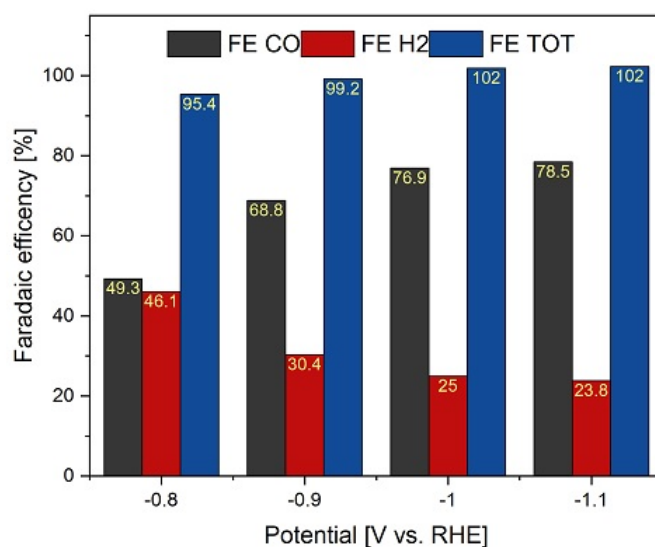


Figure 4.24: Selectivity of Zn electrodes at various potentials.

4.2.2.3 Cu₉Zn₁

The first ZnO-modified Cu electrode shows a higher current density values (Fig.4.25) compared to the ZnO electrode at each potential. The ZnO/Cu electrodes have a good stability over time (measures carried out for more than 3000s). These electrodes produce more H₂ than CO (Figs.4.26 and 4.27). However, at -1.1 V vs. RHE, there is nearly a 60/40 ratio between H₂ and CO production. This increase in CO production proves that adding ZnO to Cu can affect the selectivity of the electrode.

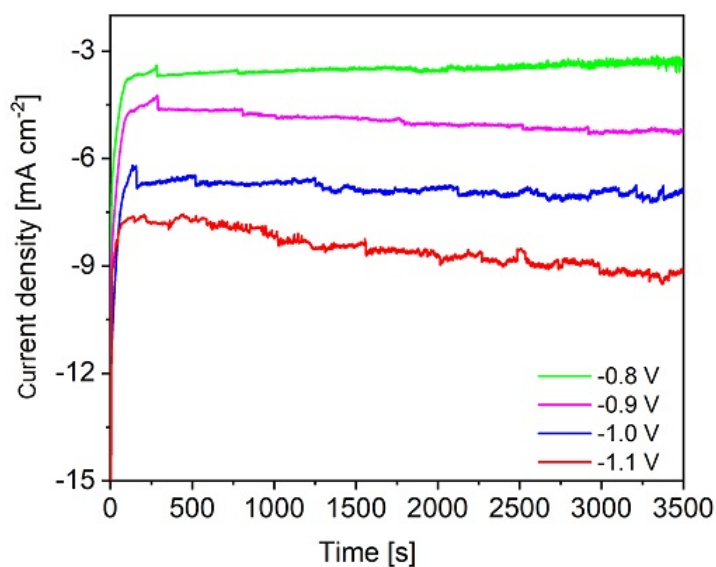


Figure 4.25: CA plots of Cu₉Zn₁ electrodes.

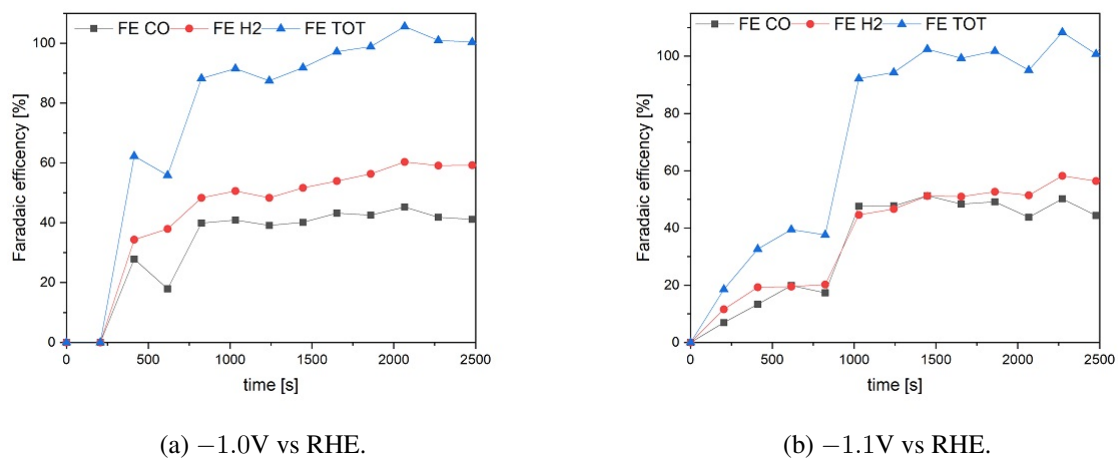


Figure 4.26: FE values over time at two different potentials of the Cu_9Zn_1 electrodes.

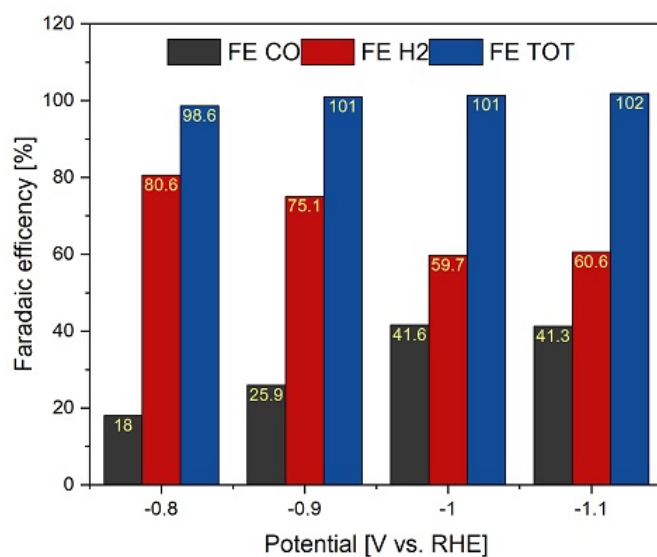


Figure 4.27: Selectivity of Cu_9Zn_1 electrodes at various potentials.

4.2.2.4 Cu_9Zn_3

Increasing the Cu/Zn atomic ratio to 9 : 3 results in a current density decrease compared to the Cu_9Zn_1 electrode, while current stability remains constant (Fig.4.28). Concerning electrode's selectivity, both figures 4.29 and 4.30 show that at -0.8V the H_2/CO ratio is ca. 50/50, while increasing the potential shifts the production towards CO ($> 60\%$ at -1.0 and -1.1V).

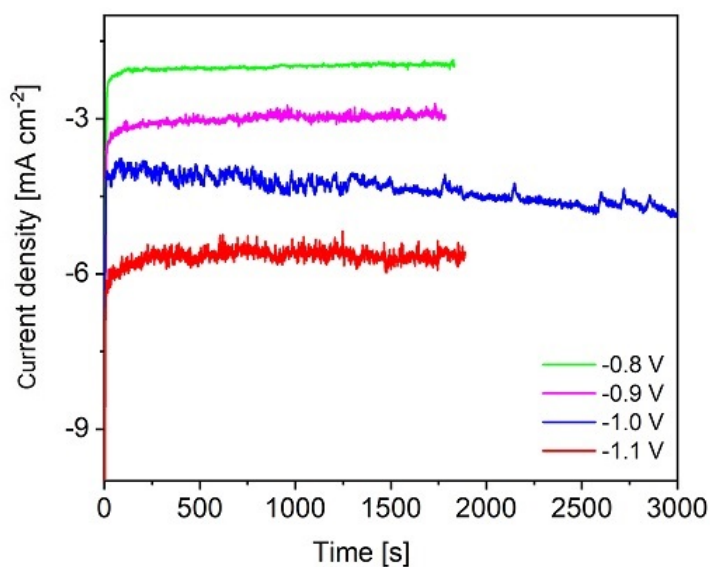
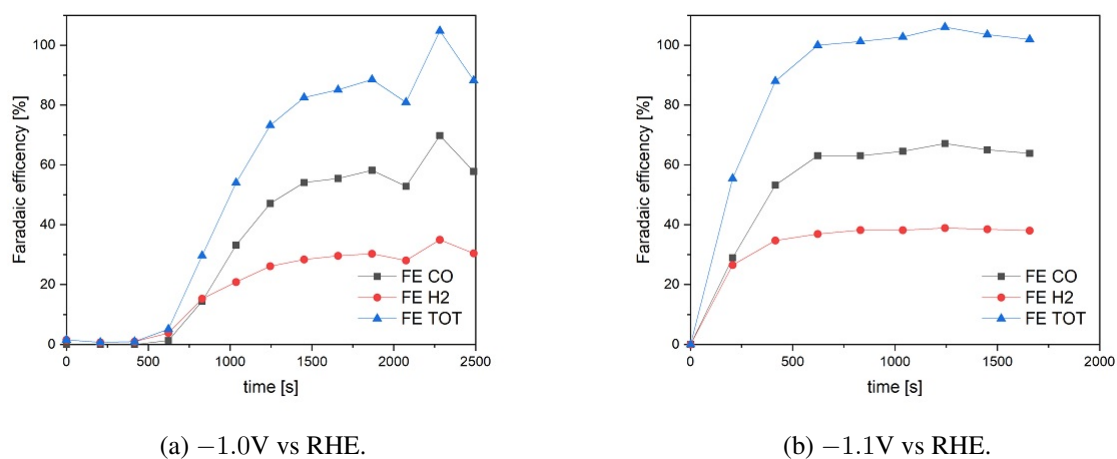


Figure 4.28: CA plots of Cu_9Zn_3 electrodes.



(a) -1.0V vs RHE.

(b) -1.1V vs RHE.

Figure 4.29: FE values over time at two different potentials of the Cu_9Zn_3 electrodes.

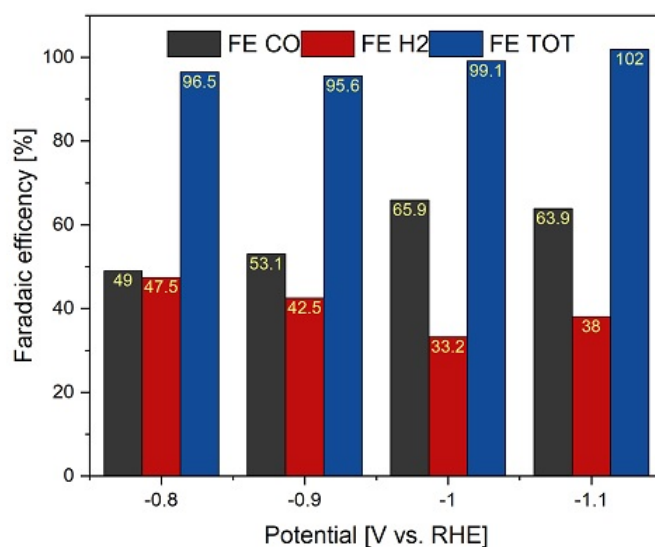


Figure 4.30: Selectivity of Cu₉Zn₃ electrodes at various potentials.

4.2.2.5 Cu₉Zn₆

The Cu₉Zn₆ electrode shows similar current stability at every potential applied; the current density increase after ca. 20 minutes at -0.8V is due to material's reduction. Furthermore, the overall current density remains constant compared to previous ZnO-modified electrodes (Fig.4.31). According to figures 4.32 and 4.33, this electrode reaches a FE_{CO} value of 70.4% at -1.0V , thus the ZnO effect is strengthened even more towards CO production.

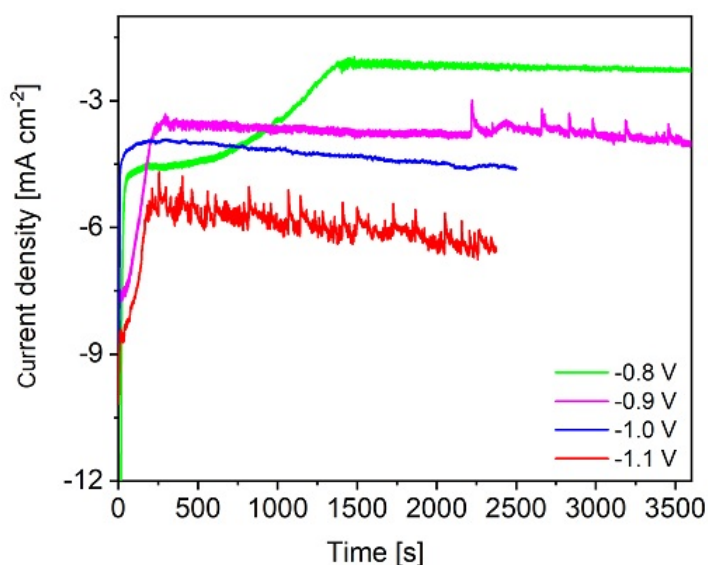


Figure 4.31: CA plots of Cu₉Zn₆ electrodes.

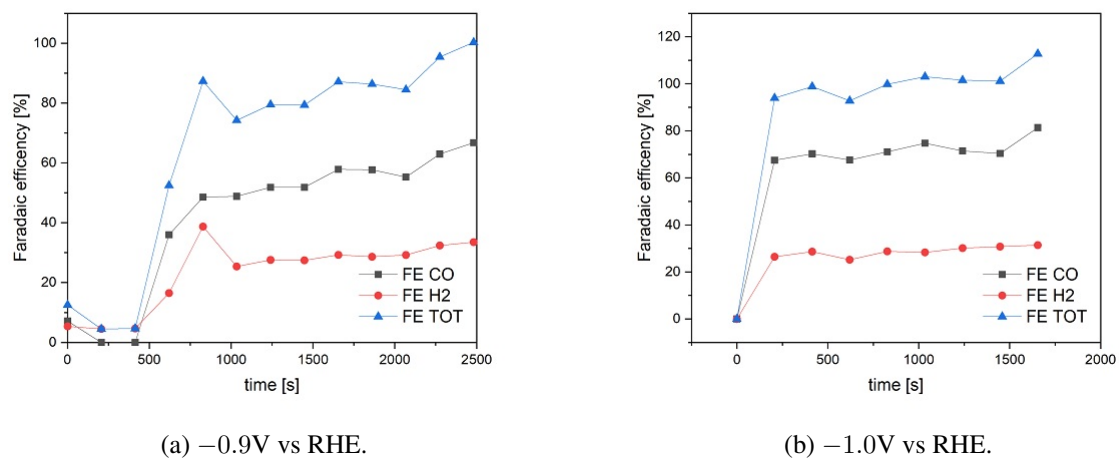


Figure 4.32: FE values over time at two different potentials of the Cu₉Zn₆ electrodes.

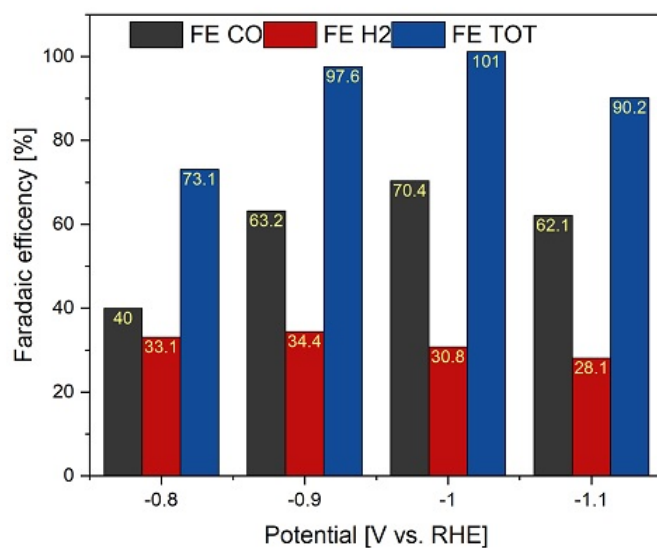


Figure 4.33: Selectivity of Cu₉Zn₆ electrodes at various potentials.

4.2.2.6 Cu₉Zn₉

Figure 4.34 shows that increasing the Cu:Zn atomic ratio to 9 : 9 does not decrease the current density to ZnO current density values ($j^{Cu_9Zn_9, min} \approx -2.5 \text{ mA/cm}^2$ vs. $j^{Zn, min} \approx -1.70 \text{ mA/cm}^2$). In fact $j^{Cu_9Zn_9}$ values are comparable with $j^{Cu_9Zn_1}$ values. However, this electrode exhibits good stability over time. The selectivity towards CO is comparable to that of Cu₉Zn₆ electrodes, with values < 71%. (Figs.4.35 and 4.36).

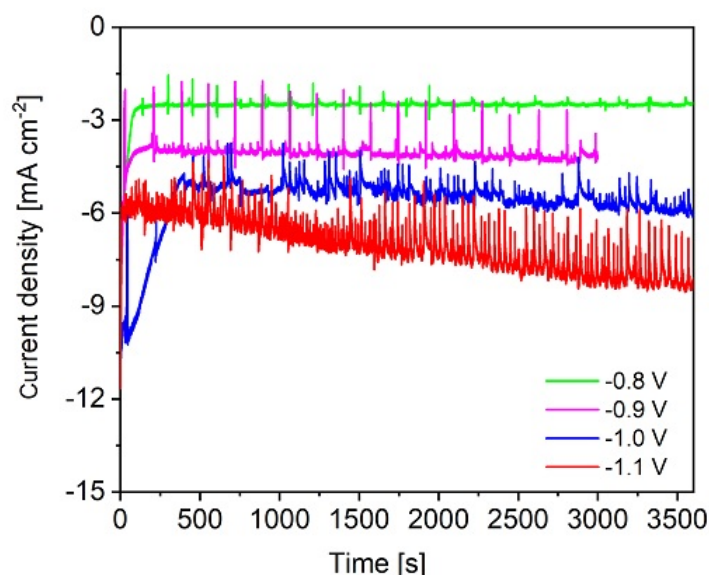
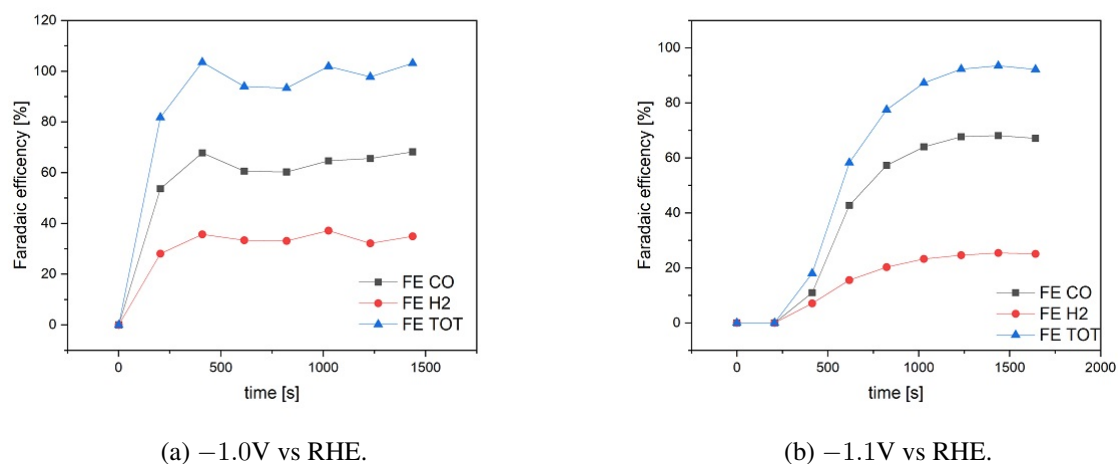


Figure 4.34: CA plots of Cu₉Zn₉ electrodes.



(a) -1.0 V vs RHE.

(b) -1.1 V vs RHE.

Figure 4.35: FE values over time at two different potentials of the Cu₉Zn₉ electrodes.

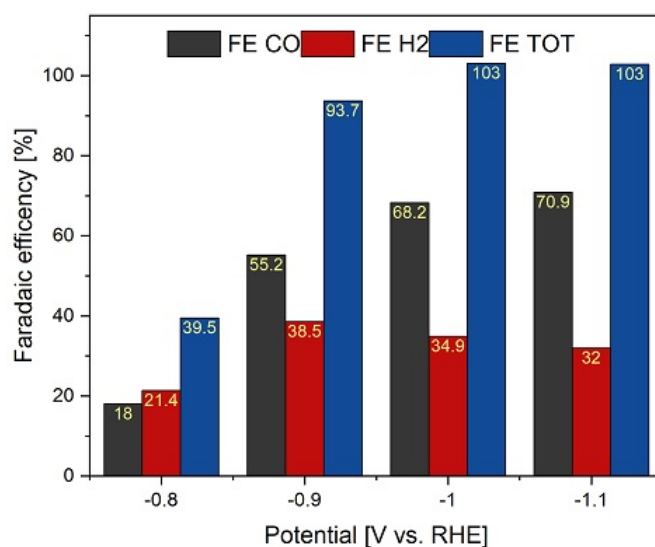


Figure 4.36: Selectivity of Cu_9Zn_9 electrodes at various potentials.

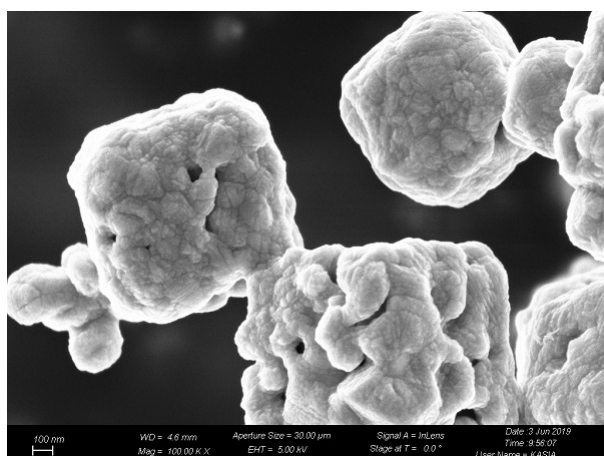
4.3 Comparison of results

Figure 4.37 clearly shows the influence of ZnO on the morphology of the synthesized powders. As explained in sec.3.1.3, all the samples are synthesized in the same conditions, only with different Zn precursor quantities. Single-metal Cu particles have a cube-like shape with a micrometric and wide size distribution (Fig.4.37a). This trend continues for the 9 : 1 atomic ratio of Cu:Zn. From figure 4.37c two different particles are distinguishable: cube-like Cu particles of submicrometric size and smaller ZnO particles. However, both morphology and size distribution of the particles change drastically increasing the atomic ratio to 9 : 3 or more (Figs.4.37d-4.37f). The increment in Zn-precursor quantities led to a decrease in Cu particles size and also to a tendency of ZnO particles to grow on top of Cu particles, with a similar size distribution and particles shape of those of the ZnO sample (4.37b).

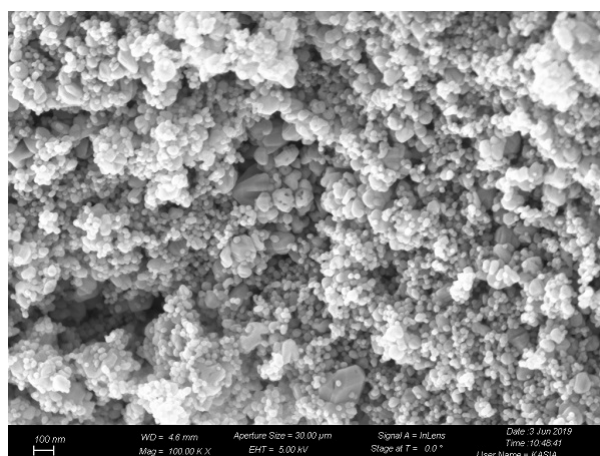
From XRD data analysis (4.38), the addition of Zn(Ace) does not mitigate the reducing effect on Cu^{2+} towards metallic Cu of both EG and NaOH. In fact, only very low quantities of Cu_2O are found in the ZnO-modified samples; these quantities can be attributed to the oxidizing effect of air to small Cu particles. The ZnO-modified samples differ among them only for peaks intensity, especially those relative to metallic Cu phase, which decrease in intensity adding more Zn-precursor.

These first comparisons highlight the effect of the Zn-precursor on particles morphology and their composition. From Cu sample to Cu_9Zn_1 sample, ZnO presence does not modify the shape and size of Cu particles. Moreover, there are two distinct crystal phases (besides low quantity of Cu_2O): metallic Cu and ZnO. The intensity of peaks for the ZnO increases with adding more Zn precursor in the synthesis, indicating more ZnO present in the final material. The crystal phases do not change considerably from sample Cu_9Zn_1 to Cu_9Zn_9 , while the morphology shifts towards a powder of ZnO-decorated Cu particles.

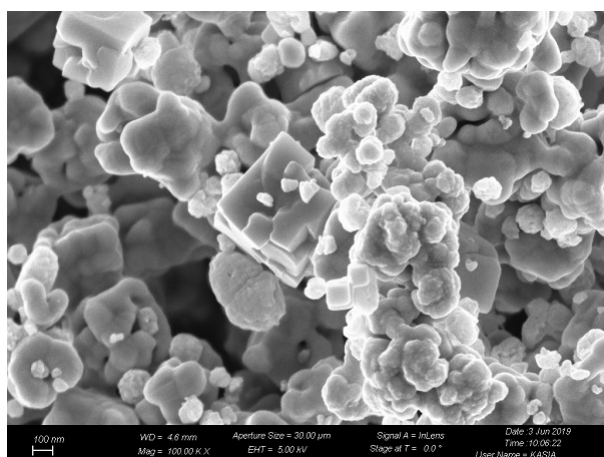
4.3 Comparison of results



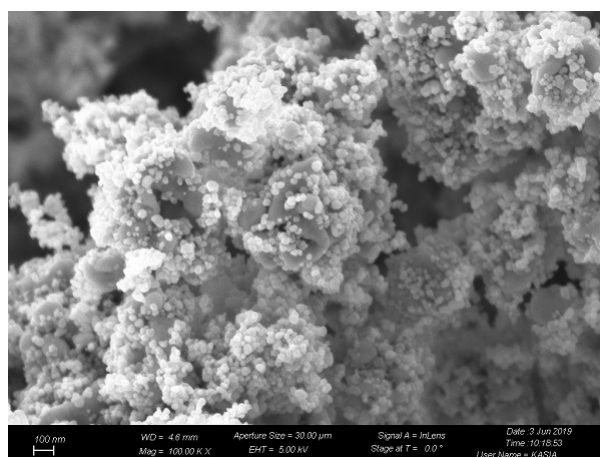
(a) Cu sample.



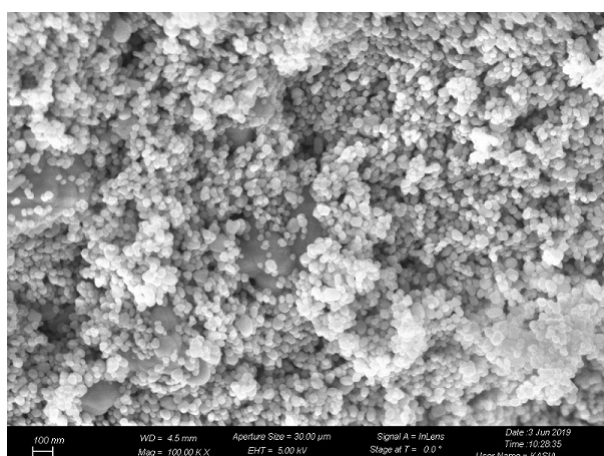
(b) Zn sample.



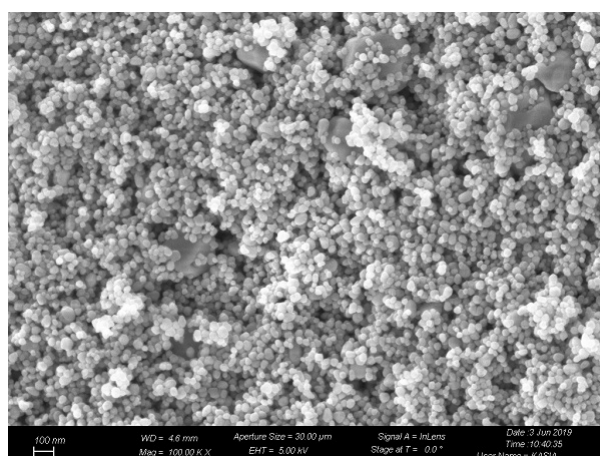
(c) Cu_9Zn_1 sample.



(d) Cu_9Zn_3 sample.



(e) Cu_9Zn_6 sample.



(f) Cu_9Zn_9 sample.

Figure 4.37: FESEM images of the samples at 10000000 X.

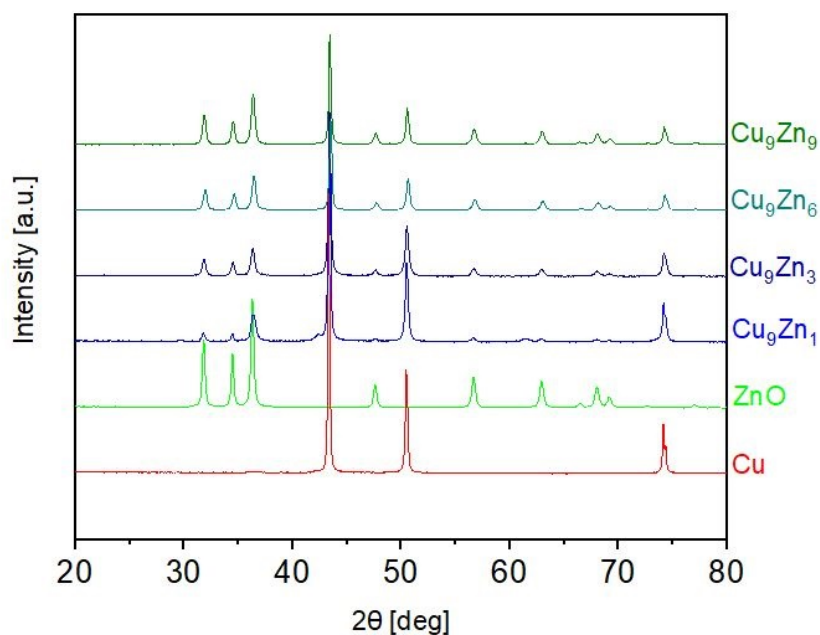
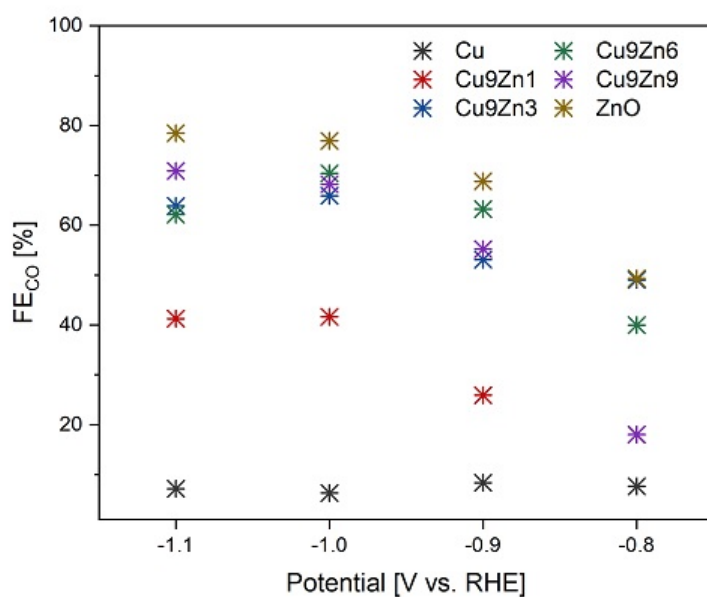


Figure 4.38: XRD spectra of all the samples.

These morphology changes modify the electrochemical properties of single-metal Cu and ZnO electrodes. The selectivity of the Cu electrode is heavily influenced by the ZnO presence (Fig.4.39); different types of active sites for CO₂RR inhabit the HER and shift the production of CO from < 10% (at all the tested potentials) at the Cu electrode to a maximum value < 71% for Cu₉Zn₃, Cu₉Zn₆ and Cu₉Zn₉ at -1.1 and -1.0V (Tab.4.2). The ZnO electrode produces around 75% of CO at both -1.1 and -1.0V.

Figure 4.39: FE_{CO} comparison of all the electrodes.

4.3 Comparison of results

Table 4.2: FE_{CO} values [%].

Potential (V vs RHE)	Cu	Cu_9Zn_1	Cu_9Zn_3	Cu_9Zn_6	Cu_9Zn_9	ZnO
-0.8	7.63	18.01	49.03	39.99	18.04	49.30
-0.9	8.36	25.92	53.08	63.22	55.19	68.82
-1.0	6.30	41.64	65.89	70.39	68.22	76.91
-1.1	7.14	41.27	63.88	62.13	70.88	78.46

Table 4.3 and figure 4.40 show that current density values of the ZnO electrode vary from 5.08 to 5.99mA/cm² at -1.0 and -1.1V respectively ($j^{Cu} = 12.83$ mA/cm² at -1.1V). The reaction rate of a species can be calculated with the equation

$$j_{CO}^{El} = FE_{CO} * j \quad (4.2)$$

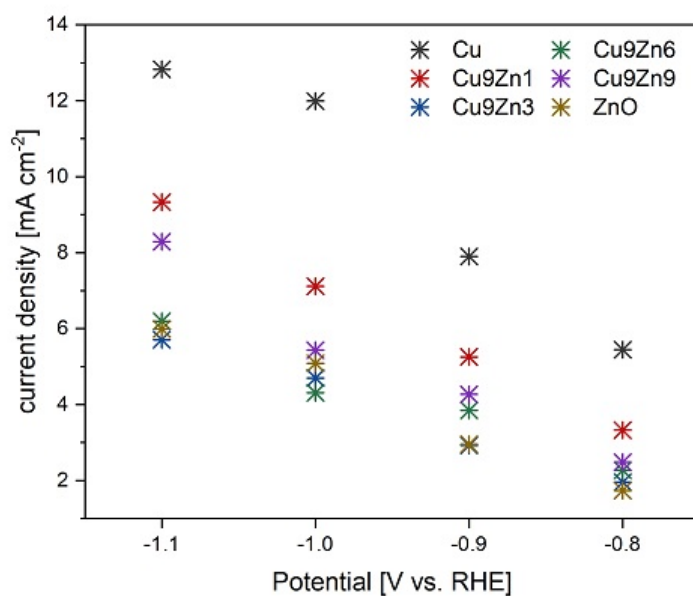
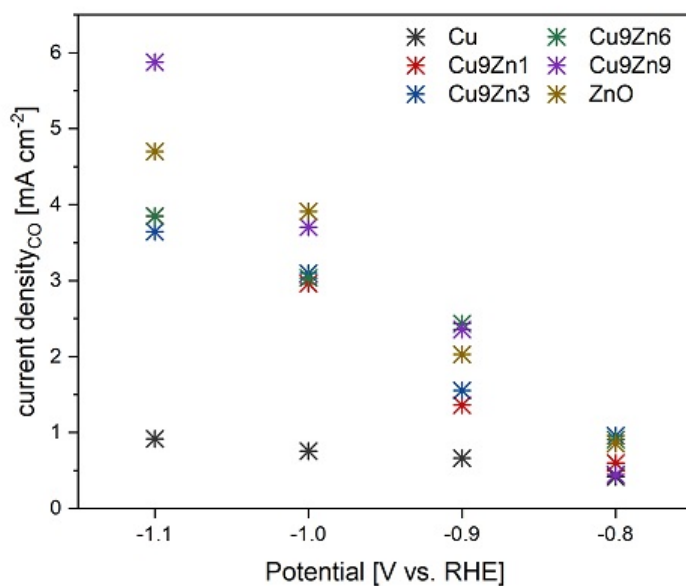
where j_{CO}^{El} is the reaction rate of CO for a specific electrode [mA/cm²] and j is the current density of the electrode. In this case, the conductivity of Cu particles plays a synergistic role with the selectivity of ZnO particles (Fig.4.41), creating a new environment for CO₂RR, thus obtaining a catalyst material for CO production with higher reaction rate ($j_{CO}^{ZnO} = 4.70$ mA/cm² vs. $j_{CO}^{Cu_9Zn_9} = 5.88$ mA/cm² at -1.1V) compared to single material catalyst (Tab.4.4).

Table 4.3: Current density j values [mA/cm²].

Potential (V vs RHE)	Cu	Cu_9Zn_1	Cu_9Zn_3	Cu_9Zn_6	Cu_9Zn_9	ZnO
-0.8	5.44	3.32	1.95	2.27	2.48	1.73
-0.9	7.90	5.25	2.92	3.85	4.27	2.95
-1.0	11.99	7.11	4.70	4.31	5.43	5.08
-1.1	12.83	9.33	5.71	6.19	8.29	5.99

Table 4.4: j_{CO}^X values [mA/cm²].

Potential (V vs RHE)	Cu	Cu_9Zn_1	Cu_9Zn_3	Cu_9Zn_6	Cu_9Zn_9	ZnO
-0.8	0.41	0.60	0.96	0.91	0.45	0.85
-0.9	0.66	1.36	1.55	2.43	2.35	2.03
-1.0	0.75	2.96	3.10	3.03	3.70	3.91
-1.1	0.92	3.85	3.64	3.85	5.88	4.70

Figure 4.40: Current density j comparison of all the electrodes.Figure 4.41: j_{CO}^{El} comparison of all the electrodes.

5 Conclusions and future developments

5.1 Industrial demands and future trends

The purpose of this work is to synthesize and characterize materials for the CO₂RR. The catalyst powders were produced via microwave-assisted solvothermal synthesis from Cu(Ace) and Zn(Ace) with different atomic ratio. This synthesis technique is promising for practical utilization because it is fast and upscalable, with low power consumption and good process parameters control. Although significant advances have been achieved in the research field of the CO₂RR in the past years, this technology is still far from practical utilization and industrial demands. A techno-economic analysis using a gross-margin model [14], shows that the economic feasibility of CO₂RR technology needs long-term durability of the electrodes and high current density values of over approximately 200mA/cm². Despite the electrode material, this high j value is difficult to reach in a liquid-phase reactor (like the electrolytic cell of this study), due to the low solubility of CO₂ in the electrolyte (33mM) that limits the mass transport of reactant to the electrode, thus hindering high productivity. Conversely, gas-phase cell systems have recently shown high performance, particularly for current density values ($> 100\text{mA/cm}^2$), while the best results achieved in liquid-phase cells are far below 100mA/cm² [15].

In order to supply continuously the reactant to the electrode, two different reactor architectures can be used: a Membrane Electrode Assembly (MEA) reactor or a microfluidic reactor (Figs.5.1a and 5.1b). In a typical MEA reactor a polymer electrolyte membrane (PEM) is placed between the cathode and anode. The type of PEMs used (anion or cation exchange membrane or bipolar membrane) is the major component to determine the performance of this type of cells, as well as the membrane deterioration caused by side products such as CO₃²⁻ [15]. The MEA reactor is promising to achieve low cell voltages and thus high energy efficiency, due to the low ohmic drop. In the microfluidic configuration, the PEM separates the cathode and anode to prevent the crossover of products to the anode side. The electrode is made of porous carbon paper coated with the catalyst and with a hydrophobic layer, in order to separate the cathode electrolyte and the CO₂ gas chamber. This configuration can mitigate the membrane deterioration and still achieve high current densities.

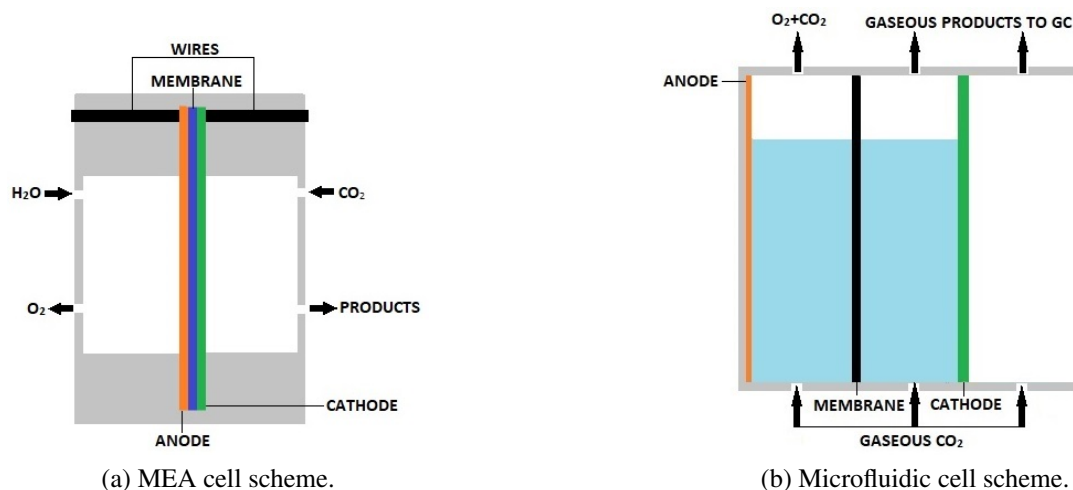


Figure 5.1: Schematic representation of gas-phase cells.

5.2 Further analyses

Further analyses can be accomplished in order to gain detailed insights into the catalysts during their working state, thus understanding the mechanisms behind the enhanced activity and CO selectivity of ZnO/Cu catalysts. These analyses include Electrochemical Impedance Spectroscopy (EIS), scanning transmission electron microscopy (STEM) equipped with energy dispersive X-ray spectroscopy (EDS) and operando X-ray absorption spectroscopy (XAS). An EIS records the current of an electrochemical system generated in response to an applied AC potential, thus obtaining the impedance of the system ($Z(\omega) = \frac{E}{I}$) in a wide frequency range. The frequency dependence of this impedance can reveal further insight into CO₂RR kinetics, in particular the contributions to the impedance value given by three different phenomena which occur during the measure: the transfer of charges at the electrode/electrolyte interface and the transport of charges in both the electrode and the electrolyte [31]. More information on the structure and chemical state of the Zn-modified catalysts can be found using STEM combined with elemental mapping by EDS or electron energy loss spectroscopy (EELS). Using EDS data, before and after CO₂RR, could clarify the role of the specific species to the reduction process through the differences in both the surface structure and the stoichiometric analysis. Moreover, operando XAS data allow to gain insight on the chemical state of the active sites during the CO₂RR.

These information together with a model of the kinetic of the CO₂RR, could lead to better designed catalysts with favourable current density values and the desired CO production ratio. The H₂/CO mixture produced with minor amount of H₂ can be further tuned by adding H₂ in order to get a syngas with a desired H₂/CO ratio. The microwave-assisted technology can be used to synthesize catalyst materials instead of classic solvothermal methods, combining an upscalable and environmental-friendly synthesis method to the main goal of finding new catalyst materials suitable for the electrochemical CO₂RR exploitation.

List of abbreviation and symbols

AC.....	Alternate Current
CA.....	Chronoamperometry
CB.....	Carbon Black
CO ₂ RR.....	CO ₂ Reduction Reaction
Cu(Ace).....	cupric acetate
CV.....	Cyclic Voltammetry
CVs.....	Cyclic Voltammograms
EB.....	Binding Energy
EC.....	Electrolytic Cell
EDS.....	Energy Dispersive X-ray Spectroscopy
EELS.....	Electron Energy Loss Spectroscopy
EG.....	Ethylene Glycol
EIS.....	Electrochemical Impedance Spectroscopy
FE.....	Faradaic Efficiency
FESEM.....	Field-Emission Scanning Electron Microscopy
GC.....	Gas Chromatography
GDL.....	Gas Diffusion Layer
HER.....	Hydrogen Evolution Reaction
ICP/OES.....	Inductively Coupled Plasma/Optical Emission Spectrometry
MEA.....	Membrane Electrode Assembly
NP.....	Nano Particles
RF.....	Radio Frequency
PEM.....	Polymer Electrolyte Membrane
RHE.....	Reference Hydrogen Electrode
SEM.....	Scanning Electron Microscopy
SHE.....	Standard Hydrogen Electrode
STEM.....	Scanning Transmission Electron Microscopy
XAS.....	X-ray absorption spectroscopy
XRD.....	X-ray Diffractometry
Zn(Ace).....	Zinc acetate
ZnO/Cu.....	ZnO-modified Cu
(<i>Ox</i>).....	relative activity of the oxidized analytes
(<i>Red</i>).....	relative activities of the reduced analytes
<i>A</i>	area [cm ²]
<i>a</i>	lattice parameter
<i>C</i> ₀ [*]	initial concentration of the O species
<i>C</i> _{<i>x</i>}	concentration of the formed species during CO ₂ RR
<i>d</i>	distance between two crystal planes
<i>D</i> ₀	diffusion coefficient of the O species
<i>E</i> ⁰	standard reduction potentials [V]
<i>E</i> ^{0'}	formal potential [V]

F	Faraday constant [C/mol]
f	frequency [Hz]
$i(t)$	current intensity [mA]
j	current density [mA/cm ²]
j_{co}	reaction rate of CO [mA/cm ²]
k	retention factor
L	GC column length
λ	wavelength [m]
Q	charge [C]
R	universal gas constant [J/mol K]
t	time [s]
T	temperature [°C, K]
t_M	hold-up time
t_R	retention time
t'_R	adjusted retention time
\bar{u}	average linear velocity
V_m	molar volume [ml/mmol]
\dot{V}_x	gas flux [ml/s]
$Z(\omega)$	impedance [Ω]

References

- [1] M Muntean et al. *Fossil CO₂ Emissions of All World Countries*. 2018.
- [2] Rajendra K Pachauri et al. *Climate change 2014: synthesis report. Contribution of Working Groups I, II and III to the fifth assessment report of the Intergovernmental Panel on Climate Change*. Ipcc, 2014.
- [3] Jinli Qiao et al. “A review of catalysts for the electroreduction of carbon dioxide to produce low-carbon fuels”. In: *Chem. Soc. Rev.* 43.2 (2014), pp. 631–675. DOI: 10.1039/c3cs60323g.
- [4] Bijandra Kumar et al. “New trends in the development of heterogeneous catalysts for electrochemical CO₂ reduction”. In: *Catalysis Today* 270 (July 2016), pp. 19–30. DOI: 10.1016/j.cattod.2016.02.006.
- [5] Juqin Zeng et al. “Advanced Cu-Sn foam for selectively converting CO₂ to CO in aqueous solution”. In: *Applied Catalysis B: Environmental* 236 (Nov. 2018), pp. 475–482. DOI: 10.1016/j.apcatb.2018.05.056.
- [6] Huan Xie et al. “Cu-based nanocatalysts for electrochemical reduction of CO₂”. In: *Nano Today* 21 (Aug. 2018), pp. 41–54. DOI: 10.1016/j.nantod.2018.05.001.
- [7] James W. Vickers, Dominic Alfonso and Douglas R. Kauffman. “Electrochemical Carbon Dioxide Reduction at Nanostructured Gold, Copper, and Alloy Materials”. In: *Energy Technology* 5.6 (Mar. 2017), pp. 775–795. DOI: 10.1002/ente.201600580.
- [8] Simelys Hernández et al. “Syngas production from electrochemical reduction of CO₂: current status and prospective implementation”. In: *Green Chemistry* 19.10 (2017), pp. 2326–2346. DOI: 10.1039/c7gc00398f.
- [9] Yoshio Hori, Katsuhiko Kikuchi and Shin Suzuki. “PRODUCTION OF CO AND CH₄ IN ELECTROCHEMICAL REDUCTION OF CO₂ AT METAL ELECTRODES IN AQUEOUS HYDROGENCARBONATE SOLUTION”. In: *Chemistry Letters* 14.11 (Nov. 1985), pp. 1695–1698. DOI: 10.1246/cl.1985.1695.
- [10] Zhouyang Yin, G. Tayhas R. Palmore and Shouheng Sun. “Electrochemical Reduction of CO₂ Catalyzed by Metal Nanocatalysts”. In: *Trends in Chemistry* (June 2019). DOI: 10.1016/j.trechm.2019.05.004.
- [11] Rita G. Lerner and George L. Trigg. *Encyclopedia of Physics*. Wiley-Interscience, 1990. ISBN: 0-471-18719-4.
- [12] Anthony Vasileff et al. “Surface and Interface Engineering in Copper-Based Bimetallic Materials for Selective CO₂ Electroreduction”. In: *Chem* 4.8 (Aug. 2018), pp. 1809–1831. DOI: 10.1016/j.chempr.2018.05.001.
- [13] Dandan Sun et al. “Microwave-assisted synthesis and optical properties of cuprous oxide micro/nanocrystals”. In: *Materials Research Bulletin* 60 (Dec. 2014), pp. 704–708. DOI: 10.1016/j.materresbull.2014.09.067.

- [14] Sumit Verma et al. “A Gross-Margin Model for Defining Technoeconomic Benchmarks in the Electroreduction of CO₂”. In: *ChemSusChem* 9.15 (June 2016), pp. 1972–1979. DOI: 10.1002/cssc.201600394.
- [15] Jun Song et al. “Towards Higher Rate Electrochemical CO₂ Conversion: From Liquid-Phase to Gas-Phase Systems”. In: *Catalysts* 9.3 (Mar. 2019), p. 224. DOI: 10.3390/catal9030224.
- [16] Rulle Reske et al. “Particle Size Effects in the Catalytic Electroreduction of CO₂ on Cu Nanoparticles”. In: *Journal of the American Chemical Society* 136.19 (May 2014), pp. 6978–6986. DOI: 10.1021/ja500328k.
- [17] Yoshio Hori et al. “Selective Formation of C₂ Compounds from Electrochemical Reduction of CO₂ at a Series of Copper Single Crystal Electrodes”. In: *The Journal of Physical Chemistry B* 106.1 (Jan. 2002), pp. 15–17. DOI: 10.1021/jp013478d.
- [18] Ruud Kortlever et al. “Catalysts and Reaction Pathways for the Electrochemical Reduction of Carbon Dioxide”. In: *The Journal of Physical Chemistry Letters* 6.20 (Sept. 2015), pp. 4073–4082. DOI: 10.1021/acs.jpcllett.5b01559.
- [19] Tiago Pardal et al. “Syngas production by electrochemical CO₂ reduction in an ionic liquid based-electrolyte”. In: *Journal of CO₂ Utilization* 18 (Mar. 2017), pp. 62–72. DOI: 10.1016/j.jcou.2017.01.007.
- [20] Sujat Sen, Dan Liu and G. Tayhas R. Palmore. “Electrochemical Reduction of CO₂ at Copper Nanofoams”. In: *ACS Catalysis* 4.9 (Aug. 2014), pp. 3091–3095. DOI: 10.1021/cs500522g.
- [21] Ki Dong Yang et al. “Morphology-Directed Selective Production of Ethylene or Ethane from CO₂ on a Cu Mesopore Electrode”. In: *Angewandte Chemie International Edition* 56.3 (Dec. 2016), pp. 796–800. DOI: 10.1002/anie.201610432.
- [22] Ruren Xu and Yan Xu. *Modern inorganic synthetic chemistry*. Elsevier, 2010.
- [23] Satoshi Horikoshi and Nick Serpone. *Microwaves in Nanoparticle Synthesis*. Wiley VCH Verlag GmbH, 24th Apr. 2013. ISBN: 3527331972. URL: https://www.ebook.de/de/product/19688382/microwaves_in_nanoparticle_synthesis.html.
- [24] Yang Leng. *Materials Characterization*. Wiley-VCH, 7th Aug. 2013. 392 pp. URL: https://www.ebook.de/de/product/21246083/yang_leng_materials_characterization.html.
- [25] Robert A. Meyers. *Encyclopedia of Analytical Chemistry*. Wiley-Blackwell, 18th Feb. 2011. 2188 pp. ISBN: 0470973331. URL: https://www.ebook.de/de/product/13728875/robert_a_meyers_encyclopedia_of_analytical_chemistry.html.
- [26] Noémie Elgrishi et al. “A Practical Beginner’s Guide to Cyclic Voltammetry”. In: *Journal of Chemical Education* 95.2 (Nov. 2017), pp. 197–206. DOI: 10.1021/acs.jchemed.7b00361.
- [27] Larry R. Faulkner Allen J. Bard. *Electrochemical Methods*. John Wiley & Sons Inc, 4th Dec. 2000. 864 pp. ISBN: 0471043729. URL: https://www.ebook.de/de/product/3254912/allen_j_bard_larry_r_faulkner_electrochemical_methods.html.

- [28] Bishnu P. Regmi and Masoud Agah. “Micro Gas Chromatography: An Overview of Critical Components and Their Integration”. In: *Analytical Chemistry* 90.22 (Oct. 2018), pp. 13133–13150. DOI: 10.1021/acs.analchem.8b01461.
- [29] Hideshi Ooka, Marta C. Figueiredo and Marc T. M. Koper. “Competition between Hydrogen Evolution and Carbon Dioxide Reduction on Copper Electrodes in Mildly Acidic Media”. In: *Langmuir* 33.37 (May 2017), pp. 9307–9313. DOI: 10.1021/acs.langmuir.7b00696.
- [30] Jonathan Rosen et al. “Electrodeposited Zn Dendrites with Enhanced CO Selectivity for Electrocatalytic CO₂ Reduction”. In: *ACS Catalysis* 5.8 (July 2015), pp. 4586–4591. DOI: 10.1021/acscatal.5b00922.
- [31] Vadim F. Lvovich. *Impedance Spectroscopy*. John Wiley & Sons Inc, 31st May 2012. 368 pp. ISBN: 0470627786. URL: https://www.ebook.de/de/product/13459627/vadim_f_lvovich_impedance_spectroscopy.html.

Acknowledgements

Questo lavoro chiude la mia carriera universitaria nel migliore dei modi. Niente di quanto studiato e ricercato in questi ultimi mesi in IIT sarebbe stato possibile senza il prezioso contributo di Juqin a tutte le fasi della tesi, dal lavoro pratico in laboratorio fino alla stesura finale del testo. Per questo: grazie mille Juqin!

Un ringraziamento speciale al professor Giancarlo Cicero per avermi dato la possibilità di lavorare in IIT e, in particolare, di affrontare l'affascinante tema della riduzione elettrochimica della CO₂.

Questo traguardo sarebbe stato impossibile senza il supporto totale della mia famiglia. Anche a distanza, nella lontana Torino.

Grazia anche a Ilaria, gioia di tutti i miei giorni.

Un grazie anche a tutte le persone conosciute in IIT, l'ambiente è piacevole e stimolante grazie a voi.

Amici di una vita, grazie anche a voi, in generale nella vita.